Supplementary Materials for

Digit patterning is controlled by a Bmp-Sox9-Wnt Turing network modulated by morphogen gradients

J. Raspopovic, L. Marcon, L. Russo, J. Sharpe*

*Corresponding author. E-mail: james.sharpe@crg.eu

Published 1 August 2014, *Science* **345**, 566 (2014)
DOI: 10.1126/science.1252960

This PDF file includes:

Other Supplementary Material for this manuscript includes the following:
(available at www.sciencemag.org/345/6196/566/suppl/DC1)

Movies S1 to S14
Microarray data, accessible through GEO Series accession no. GSE58158

List of Supplementary Figures

Contents

List of Figures

List of Tables

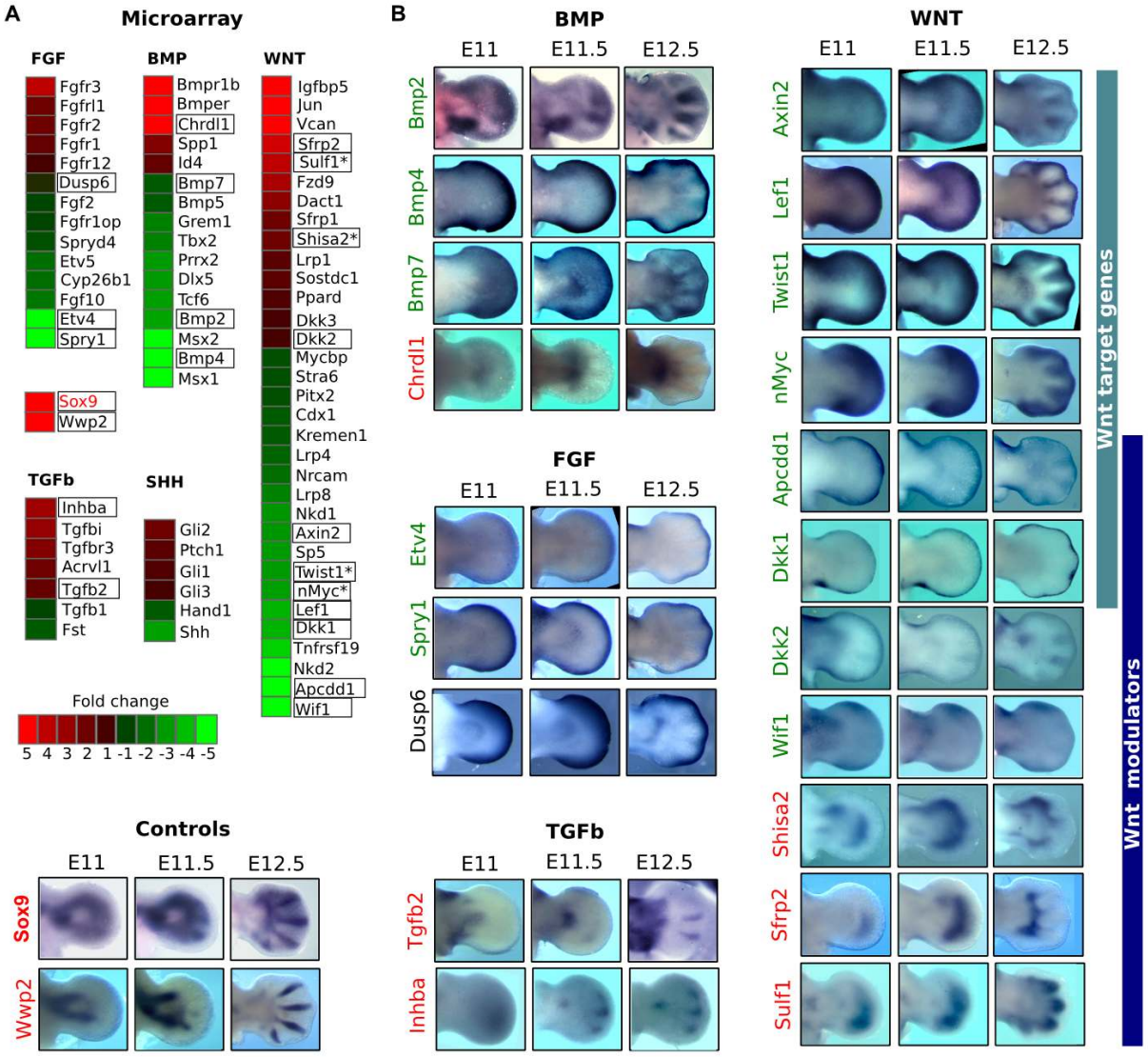

Supplementary Figure S1: A) Microarray analysis shows genes which are differentially expressed in FACS-sorted Sox9+ cells compared to Sox9- cells. Intensity of color indicates the fold-change. Genes with higher expression in Sox9+ cells are red, and those with higher expression in Sox9- cells are green. Genes are grouped by which signaling pathway they are known to play a role in (specifically: ligands, target genes and modulators/inhibitors). Based on both the number of genes and fold-change magnitude, the pathways that were most strongly represented were WNT, BMP, and FGF. Some modulators may play a role in more than one pathway (asterisk). Sox9 and Wwp2 (a direct target of Sox9 [17]) are shown as positive controls. Although the goal of the microarray is to find genes with periodic patterns (digit/interdigit), Shh is included to illustrate why some "false-positives" are inevitable. Its expression domain (posterior mesenchyme) is outside of the digital region (Sox9) and therefore appears high in the Sox9- cells. Genes with differential expression but no obvious role in developmental signaling pathways were excluded from our detailed analysis.

B) A subset of genes were analyzed by whole-mount in situ hybridization (WMISH) to check which patterns were genuinely in-phase or out-of-phase with Sox9, genes highlighted with a black rectangle in

panel A. BMP: The microarray analysis showed that the three Bmps expressed in the limb (Bmp2, Bmp4, Bmp7) are highly expressed in Sox9- cells. Among these Bmp2 has the most strikingly out-of-phase pattern with Sox9 at all stages. Chrdl1 was chosen for analysis because of its expression in Sox9+ cells but analysis by WMISH showed no clear digital pattern. FGF: Three targets of Fgf signaling (Etv4, Spry1, Dusp6) expressed in Sox9- cells do not show an interdigital pattern. TGFb: Genes in this pathway do not give a strong signal in the microarray analysis (neither in number of genes, nor in fold-difference). By WMISH, Tgfb2 and Inhba show rather late digital patterns and seem likely to be downstream of the primary patterning event rather than part of the Turing mechanism. WNT: The WNT pathway shows many differentially-expressed genes with high fold-change between Sox9+ and Sox9- cells. The first 6 expression patterns show Wnt target genes - all suggesting Wnt signaling in the interdigital tissue. The last 7 genes are all modulators of Wnt signaling (mostly extracellular inhibitors). The last 2 of these show a digital pattern (both in the microarray and WMISH), and are therefore candidates for the extracellular Wnt inhibitor which is proposed by the BSW model (see supplementary text 2.5.1).

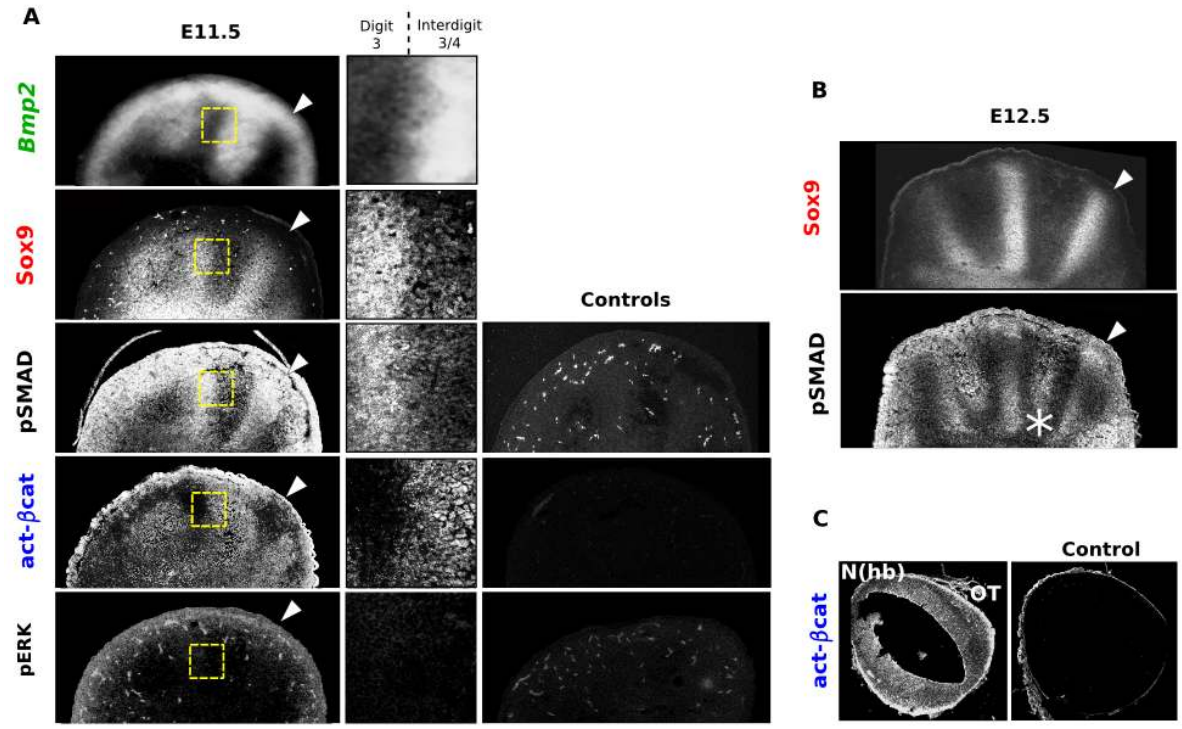

Supplementary Figure S2: A) The first column, from top to bottom shows *Bmp2* expression, endogenous Sox9-EGFP fluorescence, pSMAD, act-βcat and pERK at E11.5. The second column shows a close-up of the highlighted regions (yellow square): pSmad and act-βcat show nuclear staining as expected for active signaling. *Bmp2* and act-βcat are out-of-phase of Sox9, while pSMAD is in-phase. pERK does not show a periodic pattern as expected for the Ffg signaling gradient. The third column shows negative controls for the immunohistochemistry for pSMAD, act-βcat and pERK. B) At E12.5 Bmp signaling (pSMAD) increases in the interdigits (asterisk) and in the distal phalanx forming regions [35] reflecting cell death and chondrogenic differentiation respectively. C) A positive control for the act-βcat shows signal in the optic tract of Neuroepithelium hindbrain [36].

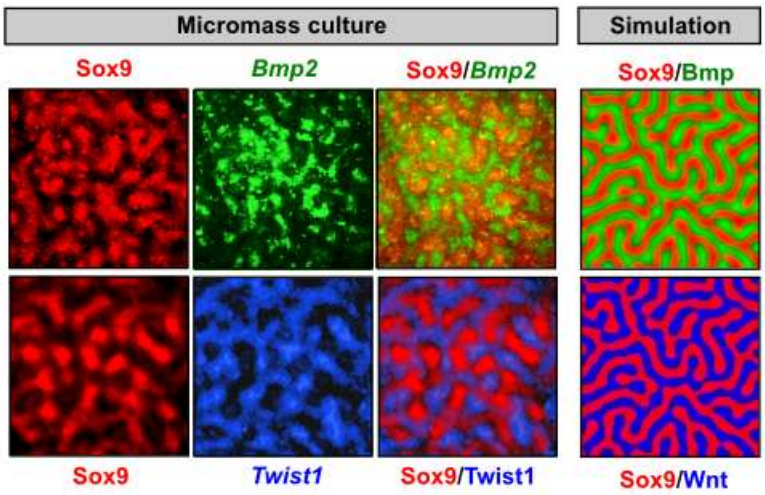

Supplementary Figure S3: Sox9-EGFP (red), Bmp2 expression (green) and the expression of the Wnt target Twist1 (blue) at 24h of micromass culture. Bmp2 and Twist1 expression are out-of-phase with Sox9 in agreement with the 2D simulations of the BSW model (rightmost column).

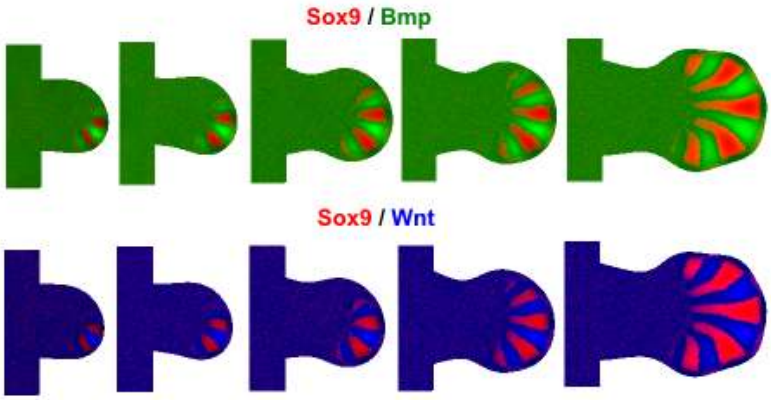

Supplementary Figure S4: The realistic limb development simulation of the BSW model presented in Figure 3E (main text) shows that Bmp (green) and Wnt (blue) form out-of-phase patterns with Sox9 (red), see the section 2.9.4.

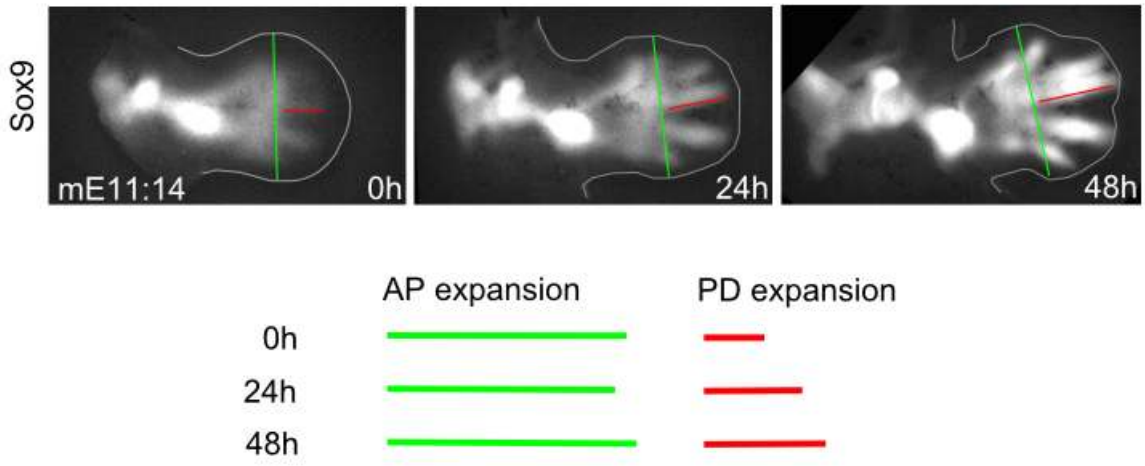

Supplementary Figure S5: Timelapse of Sox9-EGFP limb dissected from a E11.5 embryo. Over 48h, the width of the cultured limb buds does not display the normal amount of growth along the AP axis, however digital expression of Sox9-EGFP is clearly up-regulated as normal, and PD extension of the digits is comparable to the patterning observed in the WT from E11.5 to E12.5.

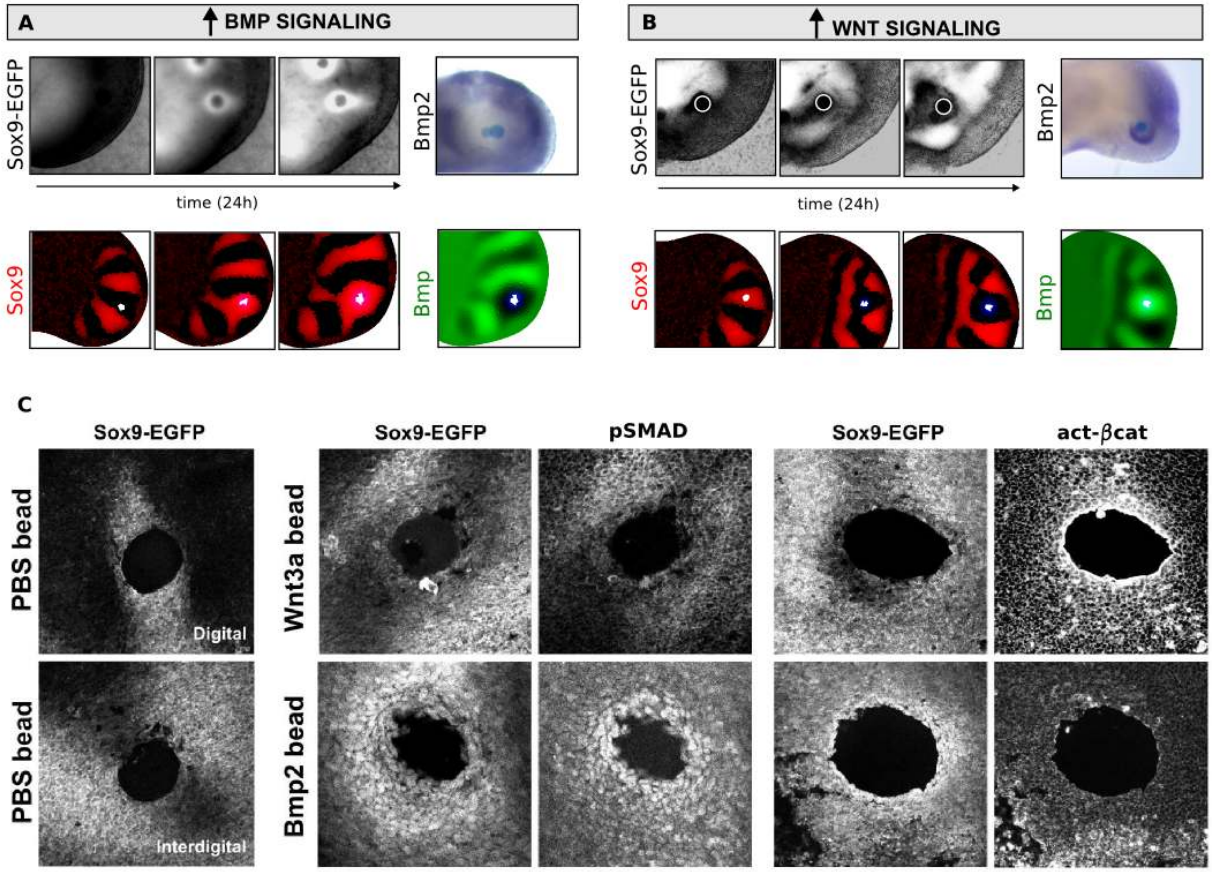

Supplementary Figure S6: A) Both in the simulation and in limb culture experiments, implantation of a Bmp bead results in progressive local up-regulation of Sox9. A clear Sox9 up-regulation is detected at 24h of culture around a Bmp2-soaked bead (top row), the simulated bead is shown in white (bottom row). On the rightmost column, as predicted by the model (bottom) Bmp2 expression is down-regulated around the Bmp2-soaked bead (top). B) Both in the simulation and in limb culture experiments, implantation of a Wnt bead results in progressive local down-regulation of Sox9. A clear Sox9 down-regulation is detected at 24h of culture around a Wnt3a-soaked bead (top row), the simulated bead is shown in white (bottom row). On the rightmost column, as predicted by the model (bottom), Bmp2 expression is up-regulated around the Wnt3a-soaked bead (top). C) Immunohistochemistry for pSMAD and act-βcat on cryosection of limb cultures implanted with Wnt3a- and Bmp2-soaked beads. First row, Wnt3a beads implanted digitally show down-regulation of Sox9 and pSMAD, and up-regulation of act-βcat. Second row, Bmp2 beads implanted interdigitally show up-regulation of Sox9 and pSMAD, and down-regulation of act-βcat. PBS beads are shown as controls.

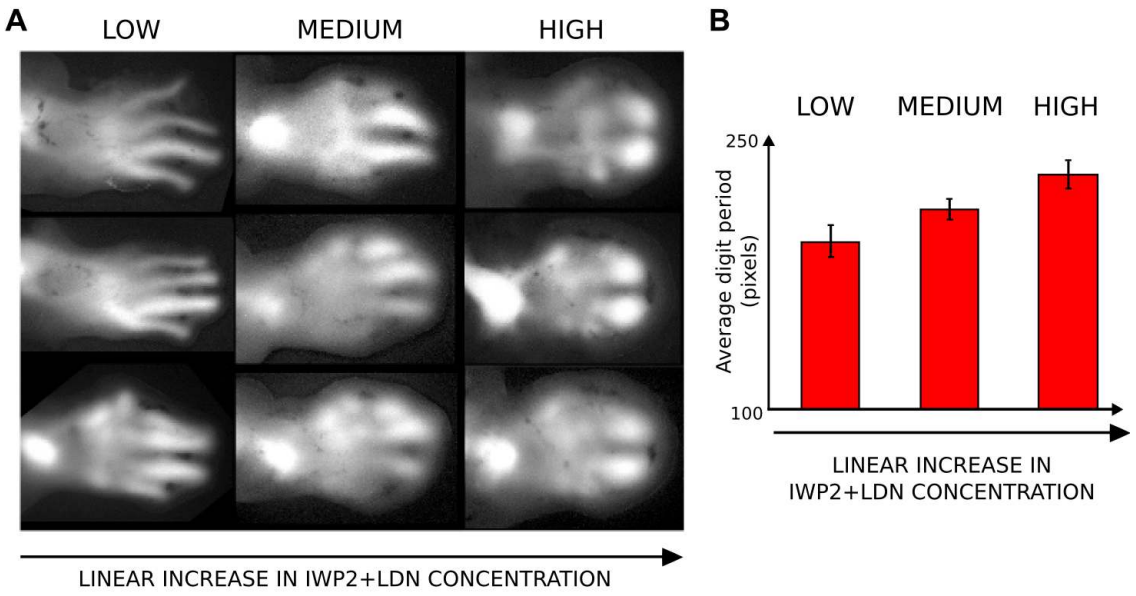

Supplementary Figure S7: A) Different limb cultures with low, medium and high concentrations of LDN and IWP2 at 48h. More severe oligodactyly patterns are observed with increasing concentrations of LDN and IWP2. B) A progressive increase of the digit period (thickness) is observed as the concentrations of LDN and IWP2 increase (low, medium, high).

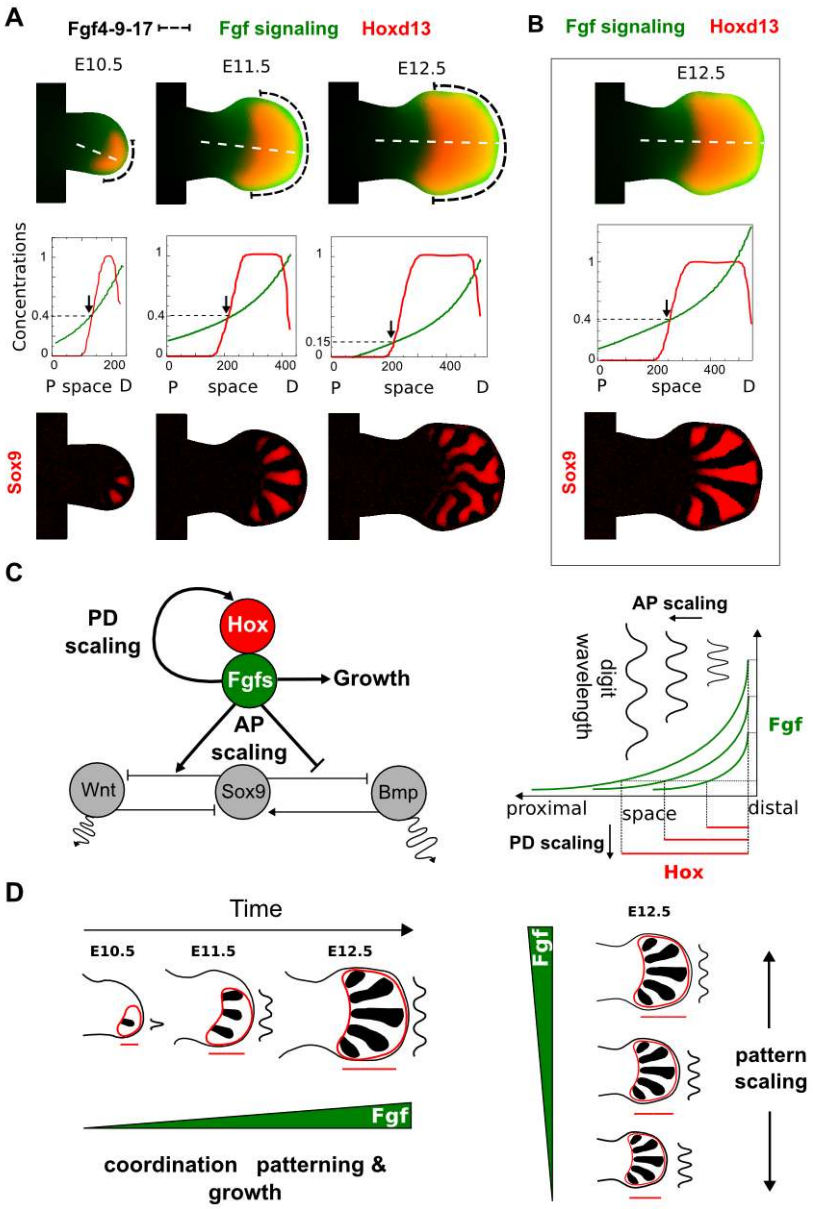

Supplementary Figure S8: A) First row, Hoxd13 expression patterns mapped from experimental data (red), a simulated Fgf signaling gradient (green) and the Fgf4-9-17 position (dashed black line). Second row, graphs show Hoxd13 expression (red) and the Fgf signaling gradient (green) along the white dashed profiles above. The third row shows the resulting simulated Sox9 pattern with the BSW model modulated by the signals above. At E10.5 and E11.5 the progressive proximal expansion of Hoxd13 is accompanied by a proximal extension of the Fgf signaling gradient that results from Fgf4-9-17 anterior expansion (see section 2.9.3).

This coordinated expansion guarantees that the proximal boundary of Hoxd13 coincides with same threshold of Fgf signaling over time (black arrows in graphs) resulting in a simulated Sox9 pattern similar to WT (third row). At E12.5, the fact that Fgf signaling does not extends proximally but Hoxd13 keeps expanding results in a lack of coordination between the two signals: black arrow points

to a lower Fgf signaling threshold. This produces a disorganized simulated Sox9 pattern (third row). B) If the progressive increase in Fgf signaling is prolonged until E12.5 (black arrow in the graph), the simulated Sox9 pattern reproduce the spatio-temporal expression of Sox9, see also section 2.9.4. C) The BSW simulation agrees with previous studies that suggest that Fgf signaling is tightly connected with the proximal expansion of Hoxd13 [34] and with growth [33]. In addition, we previously proposed that Fgf signaling promotes bigger wavelength [9]. Taken together, these three roles suggest that Fgf signaling acts as a central node to coordinate growth with the PD and the AP scaling (network on the left). On the right, the graph highlights that a change in Fgf signaling (green) results in a change in the Hox expression domain (red), which corresponds to PD scaling, and a change in digit wavelength which corresponds to AP scaling. D) This guarantees coordination between patterning and growth (left) and provide a perfect strategy for scale-invariance in limbs of different size (right).

1 Materials and Methods

1.1 Animals

C52BL/6 (Charles River) mouse timed-pregnant females were sacrificed at different days after gestation, namely E10.5, E11,5, E12.5. Embryos were dissected from decidual tissue and fixed with 4%PFA overnight. After washes in dPBT, embryos were dehydrated with increasing concentrations of methanol in dPBT and stored in 100% methanol at $-20°C$, until use for whole mount in situ hybridization (WMISH). Sox9-EGFP knock-in mice have been previously described [17]. Sox9-EGFP embryos were genotyped according to presence or absence of green fluorescent signal and were used in the different protocols described below.

1.2 Micromass cultures and FACS sorting

Limb bud autopods were dissected from E11.5 Sox9-EGFP embryos in cold PBS, digested in 0.5% Trypsin-EDTA (Gibco) for 4 min at RT, allowing the removal of the ectoderm. Remaining mesoderm was washed gently in PBS, dissociated mechanically to single cell suspension and filtered using a standard cell sorting tube with $35\mu m$ Cell-Strainer Cap. Cell sorting was performed on a BD FACSAriaII SORP cell sorter (Becton Dickinson, San Jose, CA). Single-laser analysis was carried out using 488-blue laser for morphological related parameters (FSC and SSC) and EGFP detection. EGFP green fluorescence was measured through a 525/50-nm band pass filter. Negative or positive Sox9-EGFP cells were centrifuged and re-suspended in DMEM/F12 (1X) L-Glu medium(Gibco) (with 10% FCS, 5% Penicillin-Streptomycin) at 2 x 10^7 cells/ml, and cultured as $10\mu l$ drops in 8-well plates (Ibidi) or 35mm plates (Ibidi) coated with Fibronectin. Cells were allowed to attach for 1h at $37°C$ and 5% CO2, when medium was added. After 22h, cultures were fixed in 4%PFA for 15min RT and washed in PBS. Wnt3a, Wnt5a and Wnt7a (all from RD Systems) were added to the micromass medium at $1\mu g/ml$. Fgf4 was added to the medium at $0.5\mu g/ml, 1\mu g/ml, 2\mu g/ml$. PBS was used as vehicle control.

1.3 Microarray hybridization

RNA was harvested from FACS sorted Sox9-EGFP negative and Sox9-EGFP positive cells, using RNAeasy (QIAGEN) according to the manufacturer's instructions. RNA quality was examined on a Bioanalyzer 2100 (Agilent). 100 ng of total RNA was labeled using LowInputQuick Amp Labeling kit (Agilent 5190-2305) following manufacturer instructions. Briefly: mRNA was reverse transcribed in the presence of T7-oligo-dT primer to produce cDNA. cDNA was then in vitro transcribed with T7 RNA polymerase in the presence of Cy3-CTP to produce labeled cRNA. The labeled cRNA was hybridized to the Agilent SurePrint G3 Mouse gene expression 8x60K microarray according to the manufacturer's protocol. The arrays were washed, and scanned on an Agilent G2565CA microarray scanner at 100% PMT and 3 μm resolution. Intensity data was extracted using the Feature Extraction software (Agilent).

1.4 Statistical analysis

Raw data was taken from the Feature Extraction output files and was corrected for background noise [37]. To assure comparability across samples we used quantile normalization [38]. Differential expression analysis was carried out on non control probes with an empirical Bayes approach on linear models [39]. Results were corrected for multiple testing according to the False Discovery Rate (FDR) method [40]. All statistical analyses were performed with the Bioconductor project [41] in the R statistical environment [42].

1.5 Whole mount in situ hybridization

Whole-mount in-situ hybridization (WMISH) was performed according to standard protocols [43]. In situ hybridization on micromass culture was done with the same protocol with the following changes: proteinase K ($7\mu g/\mu l$) digestion was done 2-5 min at RT.

1.6 Immunohistochemistry

Sox9-EGFP limbs at different stages (E10.5, E11. E11.5) were fixed in 4%PFA 2h RT, incubated in 30% sucrose/PBS overnight and embedded in tissue-tek OCT (Sakura). Cryosections were cut coronally and transversally at $14\mu m$. Sections were permeabilized in 10% FBS, 0.3% Tx, 0.5% milk, 0.3M glycine in PBS, for 1-2h at $4°C$ in a wet chamber. Primary antibody incubation was done in a wet chamber in 10% FBS, 5% milk in PBS overnight at $4°C$. Secondary antibodies incubation was done in 10% FBS, 0.1% BSA in PBS 2h, RT in dark in a wet chamber. Slides were mounted in VectaShield. Primary antibodies used, anti pSMAD158-Rb (Cell Signaling) (1:100), pERK (Cell Signaling) (1:50). Secondary antibody used Alexa fluor-568 anti-Rb (1:250).

For the anti-active β-catenin clone 8E7 (Millipore) antibody (1:500), the same protocol was used with following alterations: after the permeabilization step, an extra blocking step was done with 1:10 Donkey anti-Mouse Fab fragments in PBS 2h at RT (Jackson Lab.) and the secondary antibody used was Alexa fluor-568 anti-M (1:500). An alternative protocol was used with signal amplification. Endogenous peroxidase were exhausted by incubation in 3% H2O2 , 30min at RT. After the primary antibody incubation, anti-M-HRP (GE healthcare) (1:100) was diluted in 10%FBS 0.1% BSA in PBS and slides incubated for 2h, $4°C$ in a wet chamber. TSA-biotin was used at (1:50) as amplification step (Perkin-Elmer), and streptavidin-568 (Invitrogen) (1:100) for detection. Controls were done using the identical protocols but without the primary antibody.

Fixed micromass cultures were permeabilized with 0.1% Triton-X in 1%BSA in PBS for 15min at RT and washed in PBS. Primary antibody AntiEGFP-Rb (Clontech) (1:500) in 1%BSA/PBS was applied as a minimal volume to the cultures and incubated overnight at $4°C$. After washing in PBS, secondary antibody, Alexa fluor-488 anti-Rb (1:500), was diluted in 1%BSA/PBS and applied as a minimal volume to the cultures for 2-3h at RT in dark. Cultures were washed with PBS and imaged.

1.7 Bead implantations

Affigel blue beads (Bio Rad), 100-200 mesh, were washed in PBS and incubated for 1h at RT in a $10\mu l$ drop of dissolved growth factor. Recombinant Bmp2 (RD systems) was used at $100\mu g/ml$ and Wnt3a, Wnt5a, Wnt7a (RD systems) were used at $40\mu g/ml$, $100\mu g/ml$, $100\mu g/ml$, respectively. Control beads were incubated in carrier solution. Beads were implanted in dissected Sox9-EGFP limb buds at E11.5, and limbs were cultured as described below.

1.8 Limb bud cultures

Sox9-EGFP embryos were collected at E11.5 and limb buds were dissected in cold PBS. Individual limbs were transferred onto PET membrane inserts (1,0 µm pore size) (Falcon) located in a 6-multiwell plate (Falcon). Each well was filled with 1.5ml DMEM/F12 (1X) L-Glu medium(Gibco) (with 10% FCS, 5% Penicillin-Streptomycin), and limbs were covered with minimal amount of medium to allow air-liquid interface. Limbs were cultured 24h or 48h at $37°C$, 5% CO2. For treatment with drugs, compounds were dissolved in DMSO and added at different concentrations to the medium. IWP2 (Tocris) $10\mu M$, LDN-193189 (Stemgent) $10\mu M$, and for control DMSO was added at appropriate concentration. The concentrations of LDN and IWP2 used double drug treatments are shown in Table ST1.

	LDN193189	IWP2
Low	$0.1\mu M$	$0.2\mu M$
Med	$0.2\text{-}0.25\mu M$	$0.4\text{-}0.5\mu M$
High	$0.3\mu M$	$0.6\mu M$

Table ST1: LDN and IWP2 concentrations in the double-drug experiments

1.9 Microscopy and image acquisition

Images of fixed micromass cultures stained with anti-EGFP, endogenous fluorescent Sox9-EGFP of limb cultures, and WMISH results of gene expression on limbs, were collected using Leica MZ16F Fluorescence Stereo-microscope with magnification 8x. Micromass cell culture with non-FACSed cells and limb culture time-lapses were done in Zeiss Cell Observer HS, with 10x objective NA 0.3, at $37°C$ in a CO2 chamber, and using Hamamatsu ImagEM EM-CCD camera. Timelapse was monitored using AxioVision Rel software.4.8. Sox9-EGFP positive and Sox9-EGFP negative micromass cultures were timelapsed in the confocal microscope Leica TCS SP5 AOBS with an HCX PL APO CS 10x air objective, NA 0.4. Timelapse was monitored by LAS AF software. ImageJ and Photoshop CS5.1 was used for uniform image level normalization. Cell tracking was done in Fiji with MTrackJ plugin. The same confocal microscope was used for imaging immunohistochemistry results on cryosections with 20x air objective NA 0.7. Excitation at 488 and at 568 nm were provided by Argon and DPSS561 laser respectively.

1.10 Optical projection tomography

Optical projection tomography (OPT) imaging [44] was used to acquire 3D images and obtain optical sections. WMISH samples were embedded in 1% low melting point agarose (Sigma), dehydrated in 100% methanol and cleared in BABB. Samples were scanned in transmission mode at intermediate resolution (512x512 pixels) in the Bioptonics OPT scanner using Skyscan software (Bioptonics, MRC Technology). The GFP1 filter (425/40nm, 475nm LP) was used to detect sample anatomy, and the white light channel to image NBT/BCIP. OPT scans were reconstructed using NRecon software (SkyScan) and analyzed using the Bioptonics Viewer.

2 Supplementary Text

2.1 General comments on the modeling approach

The goals of this project are not to build a highly detailed "biochemistry-style" model of the relevant gene regulatory network, but rather to build the simplest dynamical model which is compatible with the data, and can make concrete predictions that can be tested experimentally. On one hand, not every known molecular state of the system (eg. phosphorylation states etc.) will be explicitly represented by a separate variable. On the other hand, the variables used will nevertheless represent measurable states of the system. In this way a model with just 3 state variables can make concrete predictions, even though the real biological system may be composed of tens of distinct molecular species. Our confidence in the model thus derives from the close correspondence between our computational predictions of manipulating the system (with drugs, beads etc.) and the results from real experiments.

Some previous models of the limb skeletal pattern attempted to explain patterning of the long bones in the stylopod and zeugopod, as well as the digits. By contrast we restrict our question to the digits because the evidence for a Turing mechanism is much stronger for this region. In particular, polydactyly is a very common phenomenon which can arise from mutations in nature or manipulations, while by contrast generating 3 long bones in the zeugopod is rare.

2.2 Linear Stability Analysis

We apply the linear-stability analysis presented in [45] to a Turing system that represents the interactions between Bmp, Sox9 and Wnt. Let us consider the following general reaction-diffusion equations for Bmp, Sox9 and Wnt:

$$\begin{aligned} \frac{\partial sox9}{\partial t} &= f(sox9, bmp, wnt) + D_{sox9}\nabla^2 sox9 \\ \frac{\partial bmp}{\partial t} &= g(sox9, bmp, wnt) + D_{bmp}\nabla^2 bmp \\ \frac{\partial wnt}{\partial t} &= h(sox9, bmp, wnt) + D_{wnt}\nabla^2 wnt \end{aligned} \tag{1}$$

we can linearize the system around the steady state
$f(sox9^*, bmp^*, wnt^*) = g(sox9^*, bmp^*, wnt^*) = h(sox9^*, bmp^*, wnt^*) = 0$
by setting the one-dimensional case with zero-flux boundary condition to:

$$\begin{aligned} sox9(x,t) &= sox9^* + \varepsilon_{sox9}(x,t) \\ bmp(x,t) &= bmp^* + \varepsilon_{bmp}(x,t) \\ wnt(x,t) &= wnt^* + \varepsilon_{wnt}(x,t) \end{aligned}$$

where $\varepsilon_{sox9}(x,t), \varepsilon_{bmp}(x,t), \varepsilon_{wnt}(x,t)$ define small partial perturbations written as:

$$\begin{aligned} \varepsilon_{sox9}(x,t) &= sox9_0 e^{\sigma t + ikx} \\ \varepsilon_{bmp}(x,t) &= bmp_0 e^{\sigma t + ikx} \\ \varepsilon_{wnt}(x,t) &= wnt_0 e^{\sigma t + ikx} \end{aligned}$$

the linearized system can be rewritten in matrix form (without considering terms that are of order higher than linear) as:

$$\begin{pmatrix} \sigma - f_{sox9} + D_{sox9}k^2 & -f_{bmp} & -f_{wnt} \\ -g_{sox9} & \sigma - g_{bmp} + D_{bmp}k^2 & -g_{wnt} \\ -h_{sox9} & -h_{bmp} & \sigma - h_{wnt} + D_{wnt}k^2 \end{pmatrix} \begin{pmatrix} sox9_0 \\ bmp_0 \\ wnt_0 \end{pmatrix} = 0,$$

where the terms in the form f_{sox9} denote the partial derivatives $\frac{\partial f}{\partial sox9}$ of f, g and h evaluated at steady state and the matrix on the left is the stability matrix A.

This system has solutions if $det(A) = 0$ which is written as:

$$\sigma^3 + a_1(k^2)\sigma^2 + a_2(k^2)\sigma + a_3(k^2) = 0, \tag{2}$$

where the terms $a_1(k^2), a_2(k^2), a_3(k^2)$ are:

$$\begin{aligned}
a_1(k^2) &= -f_{sox9} - h_{wnt} - g_{bmp} + (D_{sox9} + D_{bmp} + D_{wnt})k^2 \\
a_2(k^2) &= f_{sox9}h_{wnt} + f_{sox9}g_{bmp} + g_{bmp}h_{wnt} - h_{bmp}g_{wnt} - f_{bmp}g_{sox9} \\
&\quad - f_{wnt}h_{sox9} - k^2(D_{wnt}g_{bmp} + D_{bmp}h_{wnt} + D_{sox9}h_{wnt} \\
&\quad + D_{sox9}g_{bmp} + D_{bmp}f_{sox9} + D_{wnt}f_{sox9}) \\
&\quad + k^4(D_{bmp}D_{wnt} + D_{bmp}D_{sox9} + D_{sox9}D_{wnt})
\end{aligned}$$

$$\begin{aligned}
a_3(k^2) &= -f_{sox9}g_{bmp}h_{wnt} + f_{sox9}h_{bmp}g_{wnt} + f_{bmp}g_{sox9}h_{wnt} - f_{bmp}h_{sox9}g_{wnt} \\
&\quad - f_{wnt}g_{sox9}h_{bmp} + h_{sox9}g_{bmp}f_{wnt} + k^2(D_{wnt}f_{bmp}g_{sox9} \\
&\quad - D_{bmp}h_{sox9}f_{wnt} - D_{sox9}h_{bmp}g_{wnt} + D_{sox9}g_{bmp}h_{wnt} + D_{bmp}h_{wnt}f_{sox9} \\
&\quad + D_{wnt}g_{bmp}f_{sox9}) - k^4(D_{bmp}D_{sox9}h_{wnt} + D_{sox9}D_{wnt}g_{bmp} \\
&\quad + D_{bmp}D_{wnt}f_{sox9}) + k^6 D_{sox9}D_{bmp}D_{wnt},
\end{aligned}$$

Similarly to a two-reactant system [46] a diffusion-driven instability is formed when two conditions are satisfied:

- The system is stable without diffusion
- The system is unstable with diffusion

These two conditions correspond respectively to the existence of a negative and a positive real part in the solution σ of (2), that write:

$$Re(\sigma(k^2 = 0))) < 0 \tag{3}$$

$$Re(\sigma(k^2 > 0))) > 0 \tag{4}$$

By using the Routh-Hurwitz criteria [46] we can show that the condition (3) is satisfied when:

$$a_1(0) > 0 \wedge a_3(0) > 0 \wedge a_1(0)a_2(0) - a_3(0) > 0 \tag{5}$$

and the condition (4) is satisfied when at least one of the Routh-Hurwitz terms becomes negative for some $k^2 > 0$:

$$a_1(k^2) < 0 \vee a_3(k^2) < 0 \vee a_1(k^2)a_2(k^2) - a_3(k^2) < 0 \tag{6}$$

The second condition (6) cannot be solved analytically but can be simplified if one of the species is not diffusible [45]. If for example $D_{sox9} = 0$, the complex term $a_3(k^2)$ can be simplified to:

$$\begin{aligned}
a_3(k^2) &= -D_{bmp}D_{wnt}f_{sox9}k^4 + k^2(D_{bmp}[h_{wnt}f_{sox9} - h_{sox9}f_{wnt}] \\
&\quad + D_{wnt}[g_{bmp}f_{sox9} - f_{bmp}g_{sox9}]) + a_3(0)
\end{aligned}$$

In this case, sufficient conditions that satisfy (6) by making $a_3(k^2) < 0$ can be derived according to the sign of f_{sox9} :

$$\text{if} \quad f_{sox9} > 0, \text{ then} \quad a_3(k^2) \to -\infty \quad \text{(no diffusion-driven instability)} \tag{7}$$

$$\text{if} \quad f_{sox9} = 0, \text{ then} \quad a_3(k^2) < 0 \quad \text{if} \quad D_{bmp} h_{sox9} f_{wnt} + D_{wnt} f_{bmp} g_{sox9} > 0 \tag{8}$$

$$\text{if} \quad f_{sox9} < 0, \text{ then} \quad a_3(k^2) < 0 \quad \text{if} \quad F_1 < 0 \quad \text{and} \quad F_2 > 0 \tag{9}$$

where

$$F_1 = D_{bmp}[h_{wnt} f_{sox9} - h_{sox9} f_{wnt}] + D_{wnt}[g_{bmp} f_{sox9} - f_{bmp} g_{sox9}],$$

and

$$\begin{aligned} F_2 = {} & D_{bmp}[h_{wnt} f_{sox9} - h_{sox9} f_{wnt}] + D_{wnt}[g_{bmp} f_{sox9} - f_{bmp} g_{sox9}] \\ & + 4 D_{bmp} D_{wnt} f_{sox9} a_3(0) > 0, \end{aligned}$$

To summarize, in a three-component reaction-diffusion system with one non diffusible molecule ($D_{sox9} = 0$) the conditions (5), (8) or (9) are necessary and sufficient to form a diffusion-driven instability.

2.3 Possible Turing topologies

Now that we have derived the necessary and sufficient conditions for a diffusion-driven instability in a three-component Turing system with one non-diffusible molecule, we build a simple linear model which considers all the possible interactions between $sox9, bmp$ and wnt. We set $D_{sox9} = 0$ and define the reaction part f, g, h in (1) in the following way:

$$\begin{aligned} f(sox9, bmp, wnt) &= k_1 sox9 + k_2 bmp + k_3 wnt \\ g(sox9, bmp, wnt) &= k_4 sox9 + k_5 bmp + k_6 wnt \\ h(sox9, bmp, wnt) &= k_7 sox9 + k_8 bmp + k_9 wnt \end{aligned} \tag{10}$$

A graphical representation of the system is shown in Figure 1A. Let's now define a minimal Turing network, as a system in the form (10) that respects the condition (5), (8) (9) and has the least number of interactions (edges) between $sox9, bmp$ and wnt. Equivalently, a minimal Turing model can be formulated as a model that has the most of rates $k_i = 0 \in \{1, \dots, 9\}$ and is still capable of a diffusion-driven instability. We found that according to (5)(8)(9) minimal Turing networks can be obtained by setting at most three rates $k_i = 0$ (six interactions between $sox9, bmp$ and wnt). Our goal is to identify the possible minimal Turing topologies (defined by the signs of the six rates $k_i \neq 0 \in \{1, \dots, 9\}$) that are capable of Turing instability.

To reduce the spectrum of possible topologies we take into account previous studies that showed that BMP signaling promotes *Sox9* [24-27] and that canonical Wnt signaling mediated by β-catenin inhibits *Sox*9 [21-23], see also the paragraph in the main text. These two pieces of evidence can be represented in our model with the conditions:

$$k_2 > 0, \quad k_3 < 0 \tag{11}$$

see also Figure 1A. To analyze every minimal topology with six regulatory links, we systematically explore the possible different cases by considering all the possible triplets of $(k_{i_1} = 0, k_{i_2} = 0, k_{i_3} = 0)$ with $i_1, i_2, i_3 \in \{1, \dots, 9\}$. The total number of triplets is defined by a 3-combination of a set of 9 elements:

$$\binom{9}{3} = \frac{9!}{9!(9-3)!} = 84$$

By analyzing every minimal topology with the software Mathematica [47], we find that only 19 topologies are minimal Turing topologies that satisfy the conditions (5), (8) (9), (11), see Figure 1B.

Our next objective is to identify the type of Turing patterns that are formed by each topology and more specifically the in-phase/out-of-phase relation between the periodic patterns of $sox9, bmp$ and wnt. In the one-dimensional system, in-phase and out-of-phase patterns can be described by the sign of the eigenvector components of the maximum positive eigenvalue that satisfy the system (2).

For each topology we calculate the sign of the eigenvectors in the following way. First, we choose a set of representative parameters that satisfy the conditions (5),(8) (9), (11). Then we use the program Mathematica to solve the system (2) and find the analytical solutions of the eigenvalues $(\sigma_1^-(k), \sigma_2^-(k), \sigma_3^+(k))$ as a function of k. Because the parameters that we choose satisfy the condition (8) or the condition (9), one eigenvalue $(\sigma_3^+(k))$ will be real and positive for for certain $k > 0$, while the other two eigenvalues $(\sigma_1^-(k), \sigma_2^-(k))$ will be negative and will have a complex part. To find the wavenumber k that has the maximum eigenvalue σ we have to find the maximum of $\sigma_3^+(k)$. This could be done by solving the equation $D(\sigma_3^+(k)) = 0$, however this system cannot be solved analytically. For this reason we use the software Mathematica to find the maximum (k_{max}, σ_{max}) with a numerical method. Finally, we use Mathematica to calculate the eigenvector $\nu_3^+ = (\nu_{sox9}(k), \nu_{bmp}(k), \nu_{wnt}(k))$ of the eigenvalue $\sigma_3^+(k)$ and substitute $k = k_{max}$ to find the sign of the eigenvectors $(\nu_{sox9}(k_{max}), \nu_{bmp}(k_{max}), \nu_{wnt}(k_{max}))$.

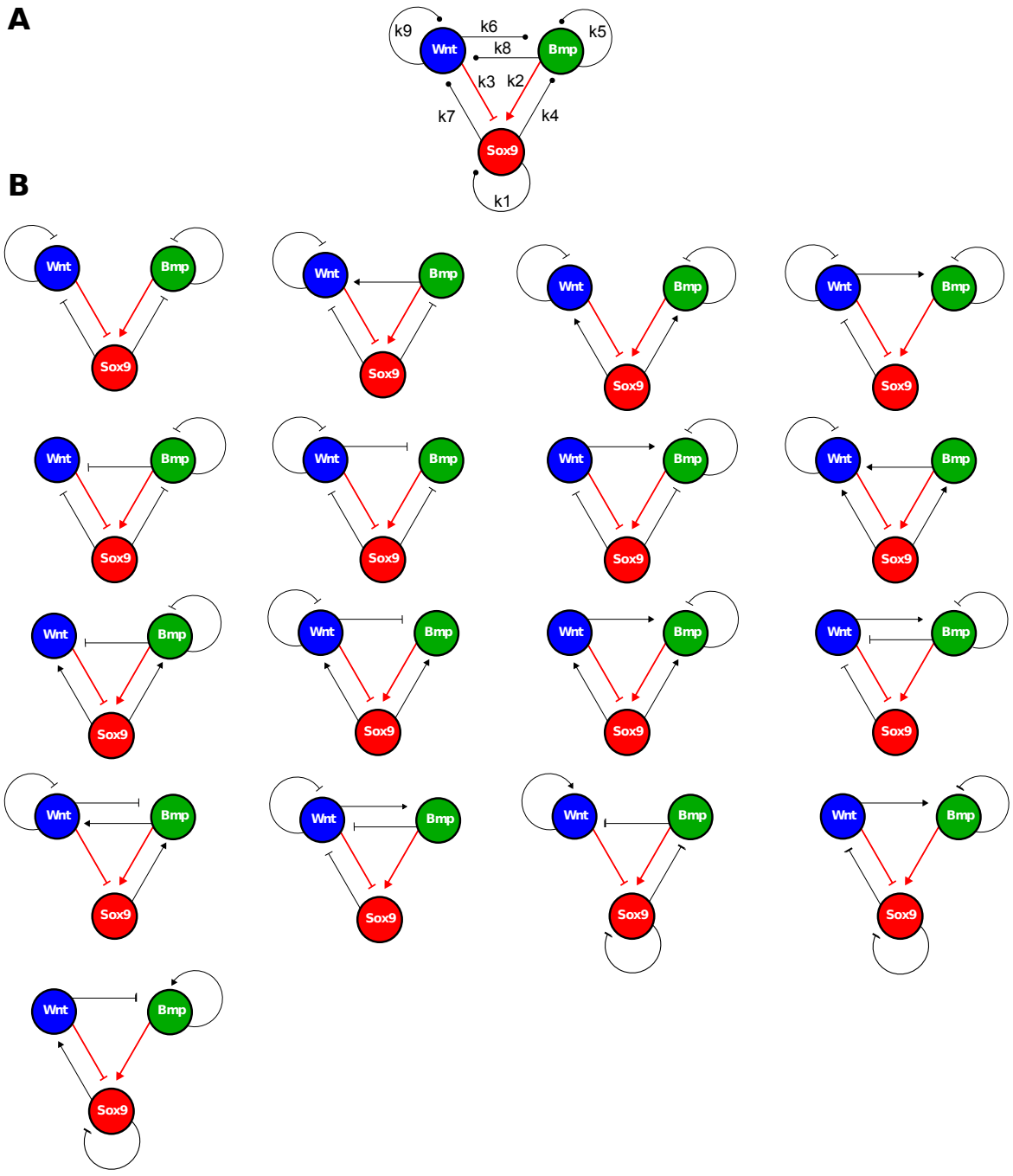

Figure 1: Possible minimal Turing topologies. A) The topology reflecting the system (10), the interaction corresponding to conditions $k_2 > 0$ and $k_3 < 0$ are highlighted in red. B) The 19 minimal Turing topologies that satisfy the conditions (5), (8) (9), (11).

2.3.1 Example of eigenvector calculation

In the following, we provide a representative example for the analysis of the eigenvectors of the network shown in Figure 2A. Let's consider the minimal Turing topology obtained by setting $k_1 = k_6 = k_8 = 0$:

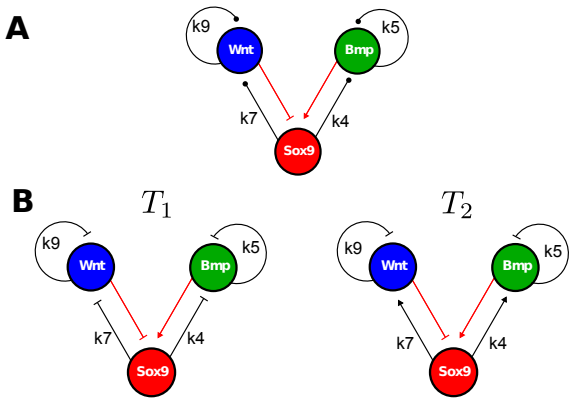

Figure 2: A) Networks capable of diffusion driven instability when $k_1 = k_6 = k_8 = 0$. B) The two possible minimal Turing topologies: T_1 with $k_5 < 0, k_4 < 0, k_7 < 0, k_9 < 0$ and T_2 with $k_5 < 0, k_4 < 0, k_7 > 0, k_9 > 0$.

Using the software Mathematica we find that the network satisfies the conditions (5)(8)(11) when:

$$k_5<0 \;\;\&\;\; k_9<0$$

$$\&$$

$$k_5 < k_9 \;\begin{cases} k_7<0 \;\&\; k_3<0 \;\&\; k_4<0 \;\&\; k_2>-\frac{k_3k_5k_7}{k_4k_9} \;\&\; D_{bmp}>-\frac{D_{wnt}k_2k_4}{k_3k_7} \longrightarrow T_1 \\ k_7>0 \;\begin{cases} 0>k_3>-\frac{k_5k_9^2}{k_5k_7-k_7k_9} \;\&\; k_4>0 \;\&\; 0<k_2<-\frac{k_3k_5k_7}{k_4k_9} \;\&\; D_{bmp}<-\frac{D_{wnt}k_2k_4}{k_3k_7} \\ k_3\le-\frac{k_5k_9^2}{k_5k_7-k_7k_9} \;\&\; k_4>0 \;\&\; 0<k_2<\frac{k_5^2k_9-k_3k_7k_9+k_5k_9^2}{k_4k_5} \;\&\; D_{bmp}<-\frac{D_{wnt}k_2k_4}{k_3k_7} \end{cases} \Big\} \longrightarrow T_2 \end{cases}$$

$$k_5 = k_9 \;\begin{cases} k_7<0 \;\&\; k_3<0 \;\&\; k_4<0 \;\&\; k_2>-\frac{k_3k_7}{k_4} \;\&\; D_{bmp}>-\frac{D_{wnt}k_2k_4}{k_3k_7} \longrightarrow T_1 \\ k_7>0 \;\&\; k_3<0 \;\&\; k_4>0 \;\&\; 0<k_2<-\frac{k_3k_7}{k_4} \;\&\; D_{bmp}<-\frac{D_{wnt}k_2k_4}{k_3k_7} \longrightarrow T_2 \end{cases}$$

$$k_5 > k_9 \;\begin{cases} k_7<0 \;\begin{cases} k_3\le-\frac{k_5k_9^2}{k_5k_7-k_7k_9} \;\&\; k_4<0 \;\&\; k_2>\frac{k_5^2k_9-k_3k_7k_9+k_5k_9^2}{k_4k_5} \;\&\; D_{bmp}>-\frac{D_{wnt}k_2k_4}{k_3k_7} \\ 0>k_3>-\frac{k_5k_9^2}{k_5k_7-k_7k_9} \;\&\; k_4<0 \;\&\; k_2>-\frac{k_3k_5k_7}{k_4k_9} \;\&\; D_{bmp}>-\frac{D_{wnt}k_2k_4}{k_3k_7} \end{cases} \Big\} \longrightarrow T_1 \\ k_7>0 \;\&\; k_3<0 \;\&\; k_4>0 \;\&\; 0<k_2<-\frac{k_3k_5k_7}{k_4k_9} \;\&\; D_{bmp}<-\frac{D_{wnt}k_2k_4}{k_3k_7} \longrightarrow T_2 \end{cases}$$

Figure 3: Conditions required to form diffusion-driven instability with the network shown in Figure 2A.

The conditions for the stability of the homogeneous steady state (5) require $k_5 < 0, k_9 < 0$ and depending on the relation between these two rates define three different cases. Nevertheless, in each case there are only two possible sets of signs for the six rates k_i (two possible topologies), see Figure 2B. We

consider the case with $k_5 = k_9$ as a representative example, see the conditions outlined in red in Figure 3, and define two sets of parameters that implement the two possible topologies, see Table ST2 and Table ST3.

k_2	k_3	k_4	k_5	k_7	k_9	D_{bmp}	D_{wnt}
1	-1	-1.59	-0.1	-1.27	-0.1	2.5	1

Table ST2: Parameter set for topology T_1

k_2	k_3	k_4	k_5	k_7	k_9	D_{bmp}	D_{wnt}
1	-1	1.27	-0.1	1.59	-0.1	1	2.5

Table ST3: Parameter set for topology T_2

2.3.2 Eigenvectors of topology T_1

First we analyze the topology T_1. We derive the stability Matrix A and substitute the parameter set in Table ST2:

$$A = \begin{pmatrix} 0 & k_2 & k_3 \\ k_4 & -D_{bmp}\mathbf{k}^2 + k_5 & 0 \\ k_7 & 0 & -D_{wnt}\mathbf{k}^2 + k_9 \end{pmatrix} = \begin{pmatrix} 0 & 1 & -1 \\ -1.59 & -2.5\mathbf{k}^2 - 0.1 & 0 \\ -1.27 & 0 & -\mathbf{k}^2 - 0.1 \end{pmatrix}$$

We use the software Mathematica to calculate the eigenvalues of the matrix A and obtain:

$$\begin{aligned}\sigma_1^-(k) = &-(0.132283 + 0.229122i) \\ &\sqrt[3]{-7k^6 + 0.825k^4 + 52.98k^2 + \sqrt{-379.687k^{12} - 106.313k^{10}...}} - 0.286 \\ &+ \frac{(0.209987 - 0.363708i)\left(-4.75k^4 - 0.35k^2 + 0.95\right)}{\sqrt[3]{-7k^6 + 0.825k^4 + 52.98k^2 + \sqrt{-379.687k^{12} - 106.313k^{10}...}} - 0.286} \\ &- 0.333333\left(3.5k^2 + 0.2\right)\end{aligned}$$

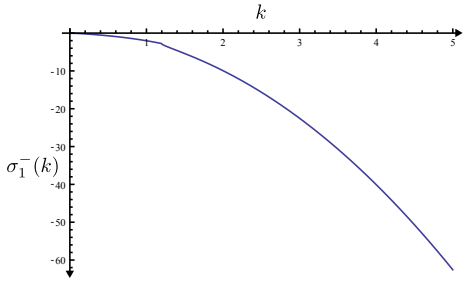

$$\begin{aligned}\sigma_2^-(k) = &-(0.132283 - 0.229122i) \\ &\sqrt[3]{-7.k^6 + 0.825k^4 + 52.98k^2 + \sqrt{-379.687k^{12} - 106.313k^{10}...}} - 0.286 \\ &+ \frac{(0.209987 + 0.363708i)\left(-4.75k^4 - 0.35k^2 + 0.95\right)}{\sqrt[3]{-7.k^6 + 0.825k^4 + 52.98k^2 + \sqrt{-379.687k^{12} - 106.313k^{10}...}} - 0.286} \\ &- 0.333333\left(3.5k^2 + 0.2\right)\end{aligned}$$

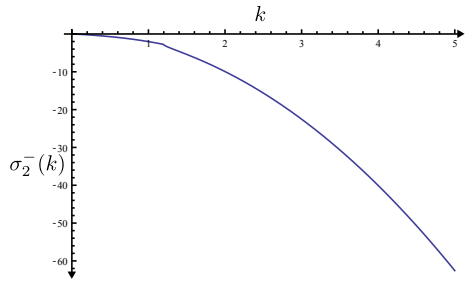

$$\sigma_3^+(k) = -0.333333\left(3.5k^2 + 0.2\right) + 0.264567\sqrt[3]{-7.k^6 + 0.825k^4 + 52.98k^2 + \sqrt{-379.687k^{12} - 106.313k^{10}...}} - 0.286 - \frac{0.419974\left(-4.75k^4 - 0.35k^2 + 0.95\right)}{\sqrt[3]{-7.k^6 + 0.825k^4 + 52.98k^2 + \sqrt{-379.687k^{12} - 106.313k^{10}...}} - 0.286}$$

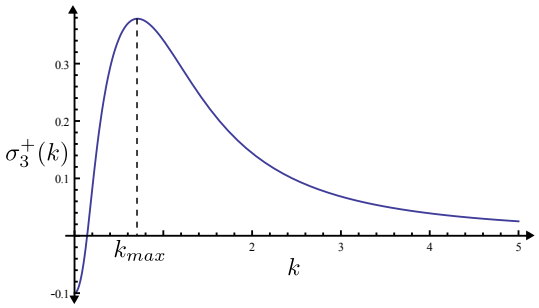

Figure 4: Dispersion relation for the topology T_1, the wavenumber k is plotted against the corresponding eigenvalue σ_3^+. k_{max} is the wavenumber with the maximum σ and corresponds to the mode that will be selected in the one-dimensional case.

The two eigenvalues $\sigma_1^-(k), \sigma_2^-(k)$ are negative and have a complex part, while $\sigma_3^+(k)$ is real and assumes positive values for certain $k > 0$. We use the software Mathematica to calculate with a gradient ascend method the wavenumber k_{max} with the maximum eigenvalue σ_3^+ and obtain $k_{max} = 0.709445$. Finally we substitute k with k_{max} in the stability matrix A and calculate the eigenvector $\nu_3^+(k)$ of the eigenvalue $\sigma_3^+(k)$, we obtain:

$$\nu_3^+(k) = (\nu_{sox9}(k), \nu_{bmp}(k), \nu_{wnt}(k)) = (-0.533574, 0.488553, 0.690373)$$

$$\frac{\nu_{sox9}(k)}{\nu_{bmp}(k)} = - \quad \frac{\nu_{bmp}(k)}{\nu_{wnt}(k)} = +$$

Our analysis reveals that the *sox*9 component has the opposite sign of the *bmp* and *wnt* components. This implies that *bmp* and *wnt* will both form periodic patterns that are out-of-phase of *sox*9. To ensure that the relation between the three eigenvector components of $\sigma_3^+(k)$ is maintained when the kinetic parameters k_i are changed, we allow one parameter k_i to change at a time and calculate the

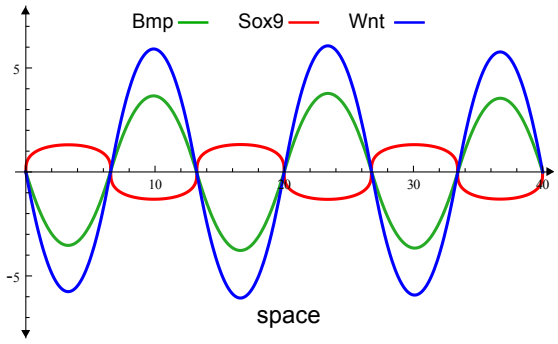

Figure 5: Numerical simulation of T_1 at time $t = 1000$. The periodic pattern of $sox9$ (red) is out-of-phase of bmp and wnt (green and blue).

ratio $\frac{\nu_{sox9}(k)}{\nu_{bmp}(k)}$ and the ratio $\frac{\nu_{bmp}(k)}{\nu_{wnt}(k)}$. For each parameter, we perform the analysis by starting from the parameter set in Table ST2 and by changing the rate k_i within the range that satisfy the diffusion-driven instability conditions (5)(8), see the Figure 6. Our analysis confirms that the ratio $\frac{\nu_{sox9}(k)}{\nu_{bmp}(k)}$ is always negative and the ratio $\frac{\nu_{bmp}(k)}{\nu_{wnt}(k)}$ is positive.

Finally, to confirm the results of the eigenvector analysis we perform a one-dimensional simulation with the parameters shown in Table ST2. As initial conditions we use a slight random perturbation (± 0.1) of the homogeneous steady state $(sox9_0, bmp_0, wnt_0) = (0, 0, 0)$ and we consider a one-dimensional spatial domain of 40 space units. If we just set these parameters in the equations system (10) we would obtain a diffusion-driven instability that grows infinitely. To avoid the infinite growth we add a cubic saturation term to the function $f(sox9, bmp, wnt)$ as follows:

$$f(sox9, bmp, wnt) = k_1 sox9 + k_2 bmp + k_3 wnt - sox9^3$$

The cubic term "$-sox9^3$" guarantees a symmetrical saturation of $sox9$ around the steady sate $sox9_0 = 0$ and prevents the infinite growth of the system by limiting the auto-catalysis of $sox9$. In biological terms the saturation represents the maximum transcriptional rate of Sox9. Although the form of saturation introduced in the model may differ from the real system, the qualitative aspect of the analytical and numerical results presented in this study do not depend on the saturation type. Moreover, the linear stability analysis presented at the beginning of this section neglects all the terms higher than linear. In conclusion, numerical simulations of the system are in agreement with the prediction of the eigenvector analysis and show a periodic pattern of $sox9$ that is out-of-phase of bmp and wnt, see Figure 5.

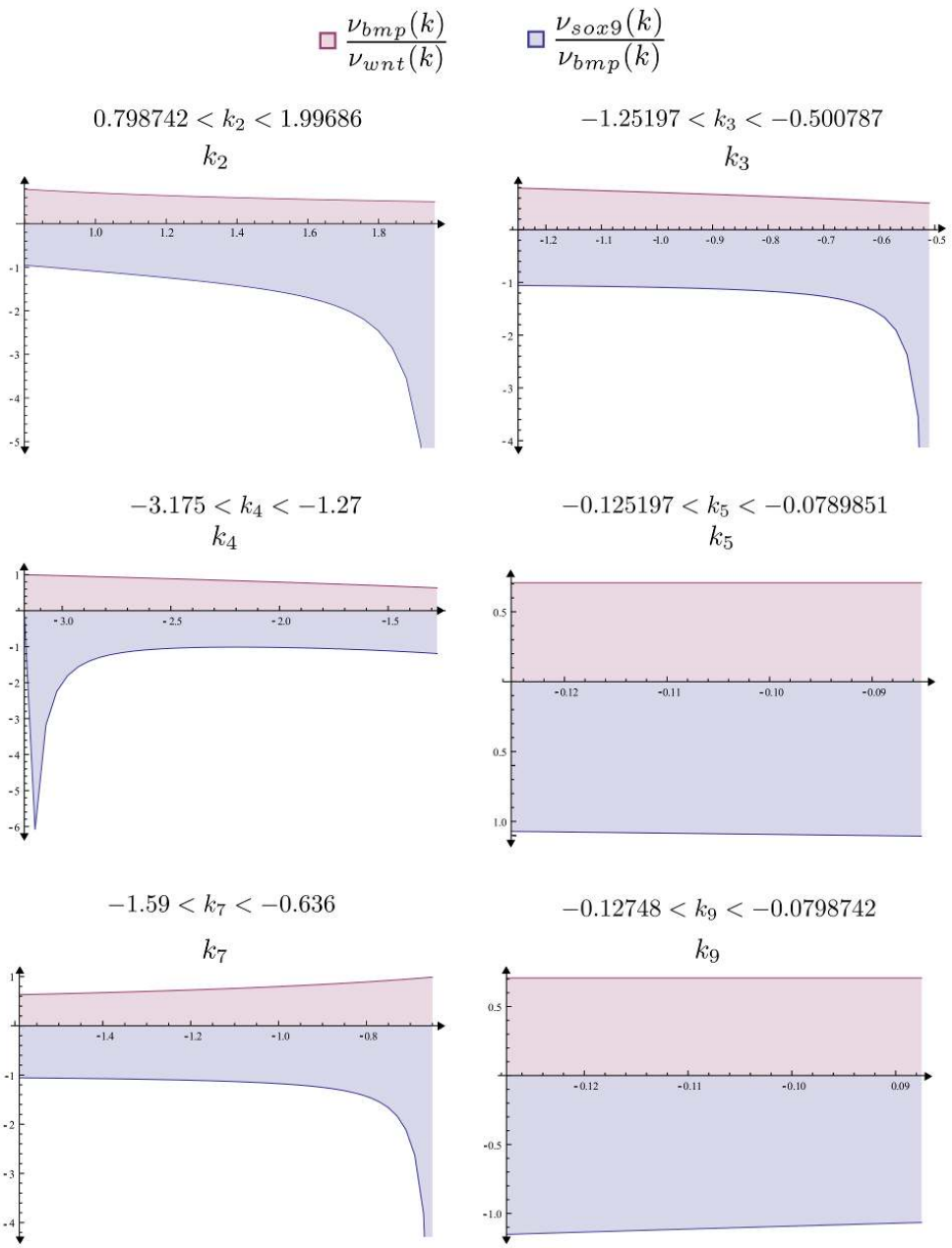

Figure 6: Analysis of the sign of the eigenvector components $(\nu_{sox9}(k), \nu_{bmp}(k), \nu_{wnt}(k))$ when the reaction rates k_i are changed for the topology T_1. The parameters k_i are varied within the range that gives rise to a diffusion-driven instability (inequalities above the graphs).

2.3.3 Eigenvectors of topology T_2

We derive the stability Matrix A and substitute the parameter set in Table ST3:

$$A = \begin{pmatrix} 0 & k_2 & k_3 \\ k_4 & -D_{bmp}\mathbf{k}^2 + k_5 & 0 \\ k_7 & 0 & -D_{wnt}\mathbf{k}^2 + k_9 \end{pmatrix} = \begin{pmatrix} 0 & 1 & -1 \\ 1.27 & -0.1 - \mathbf{k}^2 & 0 \\ 1.59 & 0 & -0.1 - 2.5\mathbf{k}^2 \end{pmatrix}$$

We use the software Mathematica to calculate the eigenvalues $(\sigma_1^-(k), \sigma_2^-(k), \sigma_3^+(k))$ of the matrix A and we find numerically the wavenumber $k = k_{max}$ for which $\sigma_3^+(k)$ is maximum. Finally, we substitute k with k_{max} in the stability matrix A and calculate the eigenvector $\nu_3^+(k)$ of the eigenvalue $\sigma_3^+(k)$, we obtain:

$$\nu_3^+(k) = (\nu_{sox9}(k), \nu_{bmp}(k), \nu_{wnt}(k)) = -0.533574, -0.690373, -0.488553$$

$$\frac{\nu_{sox9}(k)}{\nu_{bmp}(k)} = + \quad \frac{\nu_{bmp}(k)}{\nu_{wnt}(k)} = +$$

Our analysis reveals that the *sox*9 component is of the same sign of the component *bmp* and *wnt*. This implies that *bmp*, *wnt* and *sox*9 will form periodic patterns that are in-phase. To ensure that the relation between the three eigenvector components of $\sigma_3^+(k)$ is maintained when the kinetic parameters k_i are changed, we allow one parameter k_i to change at a time and calculate the ratio $\frac{\nu_{sox9}(k)}{\nu_{bmp}(k)}$ and the ratio $\frac{\nu_{bmp}(k)}{\nu_{wnt}(k)}$. For each parameter, we perform the analysis by starting from the parameter set in Table ST3 and by changing the rate k_i within the range that satisfy the diffusion-driven instability conditions (5)(8), see the Figure 8. Our analysis confirms that the ratio $\frac{\nu_{sox9}(k)}{\nu_{bmp}(k)}$ and the ratio $\frac{\nu_{bmp}(k)}{\nu_{wnt}(k)}$ are always positive.

Finally, to confirm the results of the eigenvector analysis we perform a one-dimensional simulation with the parameters shown in Table ST3. As initial conditions we use a slight random perturbation (± 0.1) of the homogeneous steady state $(sox9_0, bmp_0, wnt_0) = (0, 0, 0)$ and we consider a one-dimensional spatial domain of 40 space units. Similarly to the case of T_1, we add a negative cubic term "$-sox9^3$" to the function $f(sox9, bmp, wnt)$ in order to saturate the auto-catalysis. In agreement with the prediction of the eigenvector analysis we obtain a periodic pattern of *sox*9 that is in-phase of *bmp* and *wnt*, see Figure 7.

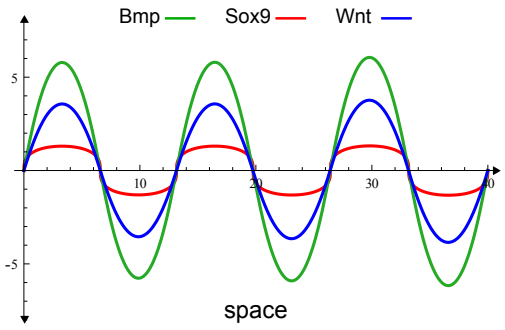

Figure 7: Numerical simulation of T_2 at time $t = 1000$. The periodic pattern of *sox*9 (red) *bmp* (green) and *wnt* (blue) are in-phase.

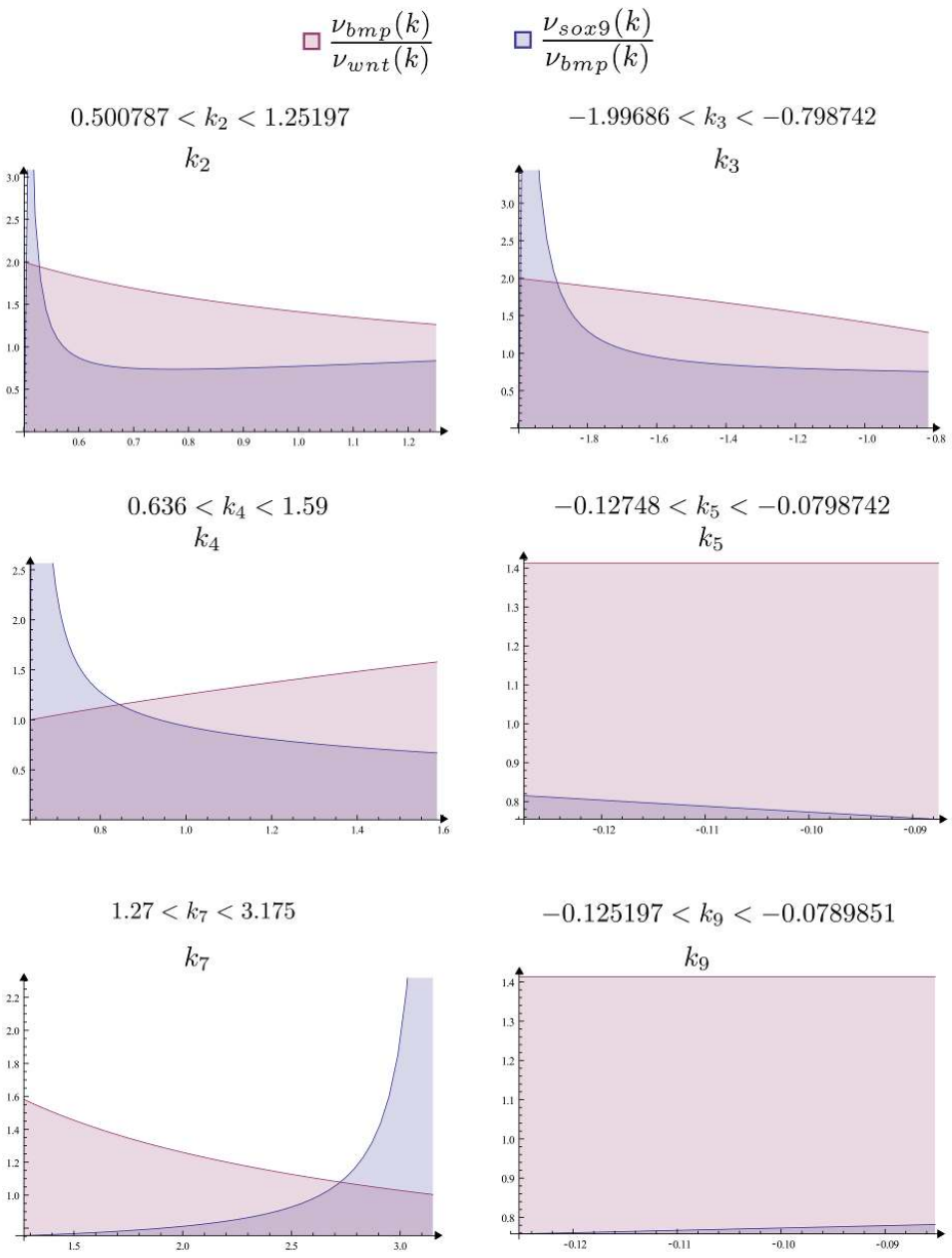

Figure 8: Analysis of the sign of the eigenvector components $(\nu_{sox9}(k), \nu_{bmp}(k), \nu_{wnt}(k))$ when the reaction rates k_i are changed for topology T_2. The parameters k_i are varied within the range that gives rise to a diffusion-driven instability (inequalities above the graphs).

2.3.4 Identification of the minimal Turing topology

Similarly to the example for topology T_1 and T_2 (see Figure 2B), we analyze the eigenvectors of all the 19 minimal Turing topologies shown in Figure 1B. We find that each minimal topology has either $(\frac{\nu_{sox9}(k)}{\nu_{bmp}(k)}, \frac{\nu_{bmp}(k)}{\nu_{wnt}(k)}) = (-,+)$ or $(\frac{\nu_{sox9}(k)}{\nu_{bmp}(k)}, \frac{\nu_{bmp}(k)}{\nu_{wnt}(k)}) = (+,+)$. The first group (A) corresponds to a *sox*9 pattern that is out-of-phase of *bmp* and *wnt* (see Figure 9A), while the second group (B) corresponds to periodic patterns of $sox9, bmp$ and *wnt* that are in-phase (see Figure 9B). No solutions where found in which *bmp* and *wnt* were out-of-phase due to the two constrains $k_2 > 0$ and $k_3 < 0$.

The microarray analysis shown in Figure S1 and the analysis of expression patterns and signaling activities shown in Figure 2 (main text) revealed that as soon as the digital pattern appears the expression of Sox9 becomes out-of-phase of Bmp2 expression and Wnt signaling activity. This allows us to restrict the analysis of the possible networks that control digit patterning to the 10 topologies presented in Figure 9A that show a periodic pattern of *sox*9 that is out-of-phase of *bmp* and *wnt*.

A detailed analysis of the conditions (5), (8) (9) in these 10 topologies highlights two observation:

1. All the topologies in Figure 9A require the diffusion of *bmp* to be higher than the diffusion of *wnt* ($D_{bmp} \gg D_{wnt}$) while the topologies in Figure 9B require the opposite ($D_{bmp} \ll D_{wnt}$)

2. Some of the models are equivalent because they satisfy the conditions (8) or (9) in the same way. The only difference between these topologies is the way in which they satisfy the conditions (5) needed for the stability of the homogeneous steady state.

The second observation can be easily seen by considering the 5 topologies shown in panel I of Figure 9A. We can observe that in these five topologies the diffusion-driven instability conditions (8) are satisfied merely by the rates k_2, k_3, k_4 and k_7, while the conditions for the homogeneous steady state stability (5) are satisfied by 2 different rates $k_i, i \in \{5, 6, 8, 9\}$ in each case, shown by the dashed arrows in Figure 9A. This can be better appreciated if we set the parameters k_2, k_3, k_4 and k_7 to the values shown in Table ST2 and we allow the other parameters to change. In this case, we obtain that the conditions (5), (8) are satisfied when:

Conditions (8) for diffusion-driven instability (case I)

True with the paramteres in Table ST1

$$k_2 = 1, \quad k_3 = -1, \quad k_4 = -1.59, \quad k_7 = -1.27, \quad D_{wnt} = 1, \; D_{bmp} = 2.5$$

Conditions (5) for homogenous steady state stability (case I)

True when

T_1 $\quad k_6 = 0, \quad k_8 = 0, \quad k_9 < 0,$

$$125197 k_9 < k_5 < \frac{0.005(-100\ k_9^2 - 159.)}{k_9} - 0.005\sqrt{\frac{10000\ k_9^4 + 82600\ k_9^2 + 25281}{k_9^2}}$$

T_3 $\quad k_6 = 0, \quad k_5 = 0, \; k_8 > 0, \; -1.25197\ k_8 < k_9 < -k_8$

T_4 $\quad k_6 = 0, \quad k_9 = 0, \; k_8 < 0, \; 1.25197\ k_8 < k_5 < k_8$

T_5 $\quad k_8 = 0, \quad k_5 = 0, \; k_6 < 0, \; k_6 < k_9 < 0.798742\ k_6$

T_6 $\quad k_8 = 0, \quad k_9 = 0, \; k_6 < 0, \; -k_6 < k_5 < -0.798742\ k_6$

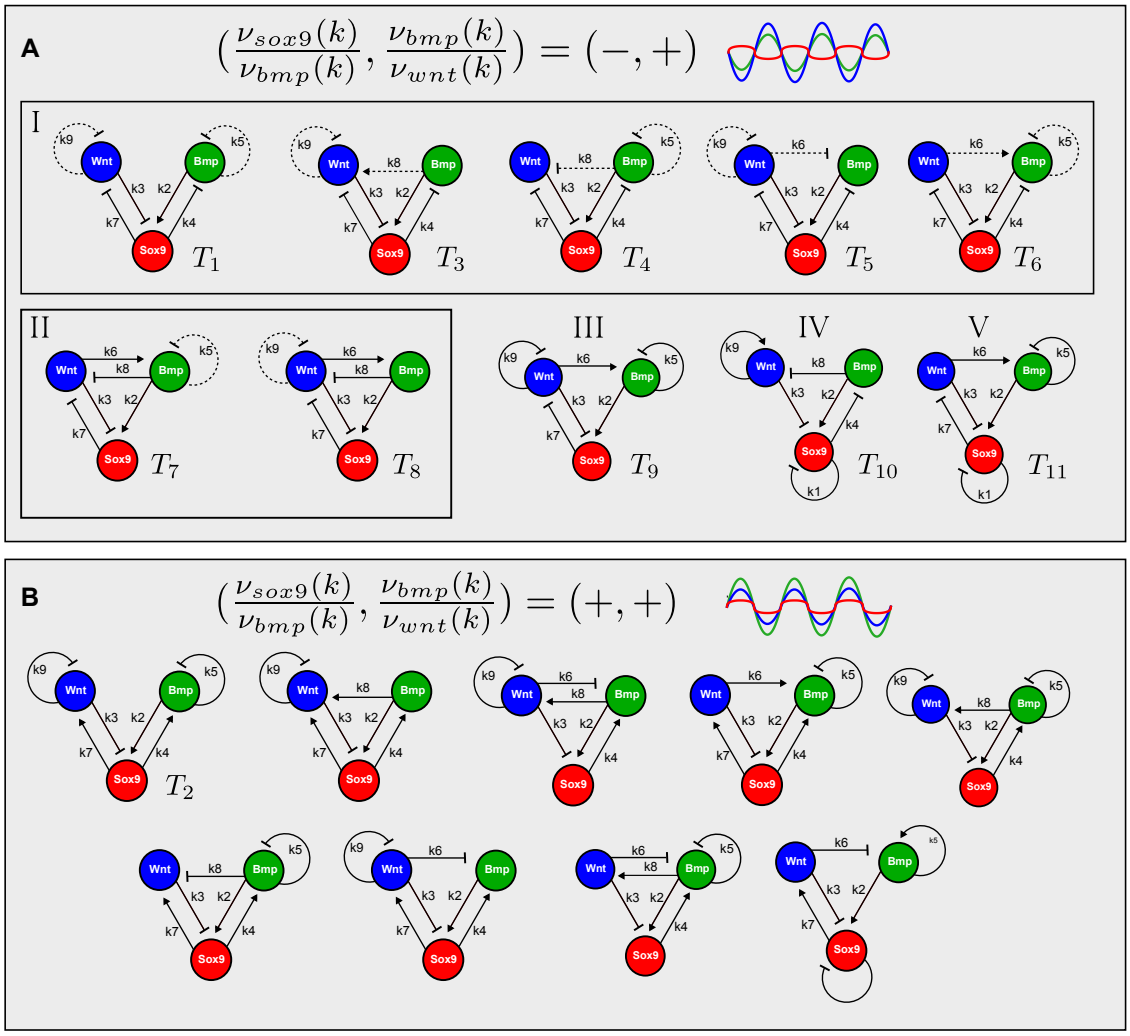

Figure 9: Result of the eigenvector analysis on the 19 minimal Turing topologies shown in Figure 1B. A) The Turing topologies that have $(\frac{\nu_{sox9}(k)}{\nu_{bmp}(k)}, \frac{\nu_{bmp}(k)}{\nu_{wnt}(k)}) = (-,+)$ and produce a *sox*9 pattern that is out-of-phase of *bmp* and *wnt*. The interaction that satisfy the homogeneous steady state stability (5) are shown with dashed lines. B) The Turing topologies that have $(\frac{\nu_{sox9}(k)}{\nu_{bmp}(k)}, \frac{\nu_{bmp}(k)}{\nu_{wnt}(k)}) = (+,+)$ and produce in-phase patterns of $sox9, bmp$ and *wnt*.

The five alternative conditions that satisfy (5) correspond respectively to the five topologies in panel I of Figure 9A (T_1 and $T_3 - T_6$) where the different interactions that satisfy (5) have been highlighted with dashed lines. In summary, our analysis reveals that the five topologies shown in panel I of Figure 9A are closely related and share the feedbacks that implement the diffusion-driven instability.

A similar analysis can be performed for the two topologies in panel II of Figure 9A. In this case it is easy to show that the diffusion-driven instability conditions (8) are satisfied just by the rates k_2, k_3, k_6, k_7 and k_8, and that the homogeneous steady state state stability (5) can be obtained either by having $k_5 < 0$ or $k_9 < 0$, see the dashed interactions in panel II of Figure 9A.

We can thus restrict our analysis to five dynamically different cases (I to V), see Figure 9A and Figure 10A. In order to compare the robustness of these five different models, we choose two representative topologies for the case I and the case II and calculate for each case the volume of the Turing space as the kinetic rates k_i are changed. We calculate the volume of the Turing space as follows:

- We choose $D_{bmp} = 2.5$ and $D_{wnt} = 1$ as representative values that satisfy $D_{bmp} \gg D_{wnt}$ (the effect of diffusion coefficients is discussed in the next section).
- We obtain non-dimensional models for each topology by dividing each rate k_i by k_2 obtaining the non-dimensional rates $k'_i = \frac{k_i}{k_2}$, see the topologies in Figure 10A.
- In each case we set two rates k'_i to 1 or -1 choosing the rates that appear only in the homogeneous steady state stability conditions (5) or the rates that have the simplest relations with other rates k'_i in (8) or (9).
- We allow the remaining three rates k'_i to vary in the range $[0, 5]$ and plot the parameter space where the conditions (5), (8) or (9) are satisfied. This range represents a plausible relative difference of five fold between the kinetic rates k_i,
- We calculate the volume of the Turing space using a numerical method to compute multiple integrals provided by the software Mathematica. The smaller the Turing space the less robust is the model because small changes in the rates k'_i can break the system and disrupt the diffusion-driven instability.

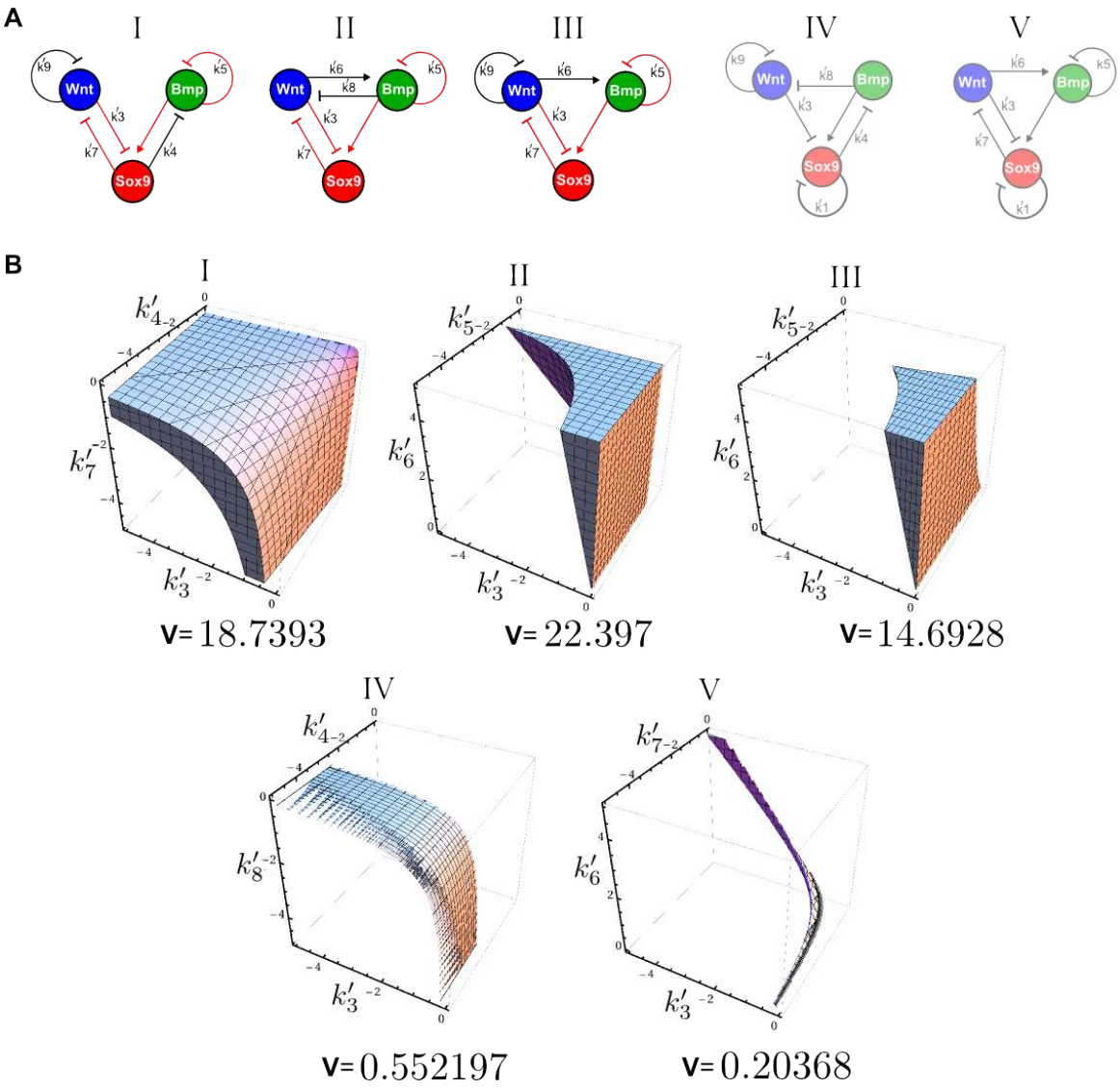

Figure 10: A) The 5 different dynamical Turing models that form a pattern with sox_9 out-of-phase of bmp and wnt. The interactions that are present in all three cases I, II, III are highlighted in red. B) The Turing space of each dynamical model with its corresponding volume **v**.

We analyze each case by considering the non-dimentionalized system:

$$\begin{aligned} f(sox9, bmp, wnt) &= k_1' sox9 + bmp + k_3' wnt \\ g(sox9, bmp, wnt) &= k_4' sox9 + k_5' bmp + k_6' wnt \\ h(sox9, bmp, wnt) &= k_7' sox9 + k_8' wnt + k_9' wnt \end{aligned} \tag{12}$$

the parameter sets used in each case are:

- I

k_1'	k_5'	k_6'	k_8'	k_9'
0	-1	0	0	-1

This model satisfy (5), (8) when: $-\frac{k_4'}{k_3'} < k_7' < -\frac{0.4k_4'}{k_3'}$

- II

k_1'	k_4'	k_7'	k_8'	k_9'
0	0	-1	-1	0

This model satisfy (5), (8) when: $k_5' < -1 \quad \& \quad k_3' > \frac{k_6'}{k_5'}$

- III

k_1'	k_4'	k_7'	k_8'	k_9'
0	0	-1	0	-1

This model satisfy (5), (8) when:

$$(k_6' \leq k_5'^2 \quad \& \quad k_3' > \frac{k_6'}{k_5'}) \parallel$$
$$(k_5'^2 < k_6' < k_5'^2 - k_5' \quad \& \quad k_3' > k_5' - k_5'^2 + k_6')$$

- IV

k_1'	k_5'	k_6'	k_7'	k_9'
-2.5	0	0	0	1

We set $k_1' = 2.5$ to better visualize the small Turing space in the interval $[0, 5]$. This model satisfy (5), (9) when:

$$(-6.25 < k_4' \leq -2.8147 \quad \& \quad \frac{0.0025(-625 + 200k_4' - 16k_4'^2)}{k_4'k_8'} < k_3' < \frac{1}{k_8'}) \parallel$$
$$(-2.8147 < k_4' < -2.5 \quad \& \quad \frac{0.25(15 + 10k_4')}{k_4'k_8'} < k_3' < \frac{1}{k_8'})$$

- V

k_1'	k_4'	k_5'	k_8'	k_9'
-1	0	-1	0	0

This model satisfy (5), (9) when:

$$-k_6' < k_3' < -0.734931\sqrt{k_6'^2} - 0.111111k_6' \quad \&$$
$$\frac{2}{k_3' - k_6'} < k_7' < -0.8\sqrt{\frac{k_3'k_6' + k_6'^2}{k_3'^4}} - \frac{0.4(k_3' + 2k_6')}{k_3'^2}$$

Our analysis reveals that the first three models I, II, III are much more robust than the models IV and V, see the volumes **V** in Figure 10B. This is consistent with the linear stability analysis presented in Section 2.2, which shows that when $f_{sox9} < 0$ (that is $k_1' < 0$) the diffusion-driven instability become more stringent, see the conditions (9).

The three models I, II, III have comparable parameter space volumes $\mathbf{v}$, see the Figure 10B, and share four of the six interactions between $sox9, bmp$ and wnt, see the interactions highlighted in red in Figure 10A. Both the model I and the model III predict the presence of a negative feedback loop in Wnt signaling, see the interactions k_9' in Figure 10A. Model II in contrast is highly based on the cross talk between the Bmp and Wnt pathway.

Our analysis reveals all 3 models to be plausible, but our goal is to uncover the simplest model compatible with the observed experimental data. We thus choose model T_1 as the minimal model on the basis of not requiring direct cross-regulation between the two signaling pathways (Figure 10A). We call this topology the Bmp-Sox9-Wnt model (BSW) and we use it as a starting point for all the analysis and simulations showed in the following sections.

2.4 Diffusion coefficients of Bmp and Wnt

By analyzing the possible Turing topologies that can produce a periodic pattern with Sox9 out-of-phase of Bmp and Wnt, we were able to identify a minimal Turing network that is compatible with our experimental data on digit patterning, see Figure 2B-C (main text). According to the diffusion-driven instability conditions (8) and (9), this network forms a Turing pattern only when the diffusion of Bmp is greater than the diffusion of Wnt. To the best of our knowledge the diffusion constants of these two signaling molecules have never been measured in mouse. Indeed, the techniques required to perform such measurements (E.g creating functional GFP-fused protein and imaging after photo-bleaching) are very challenging in mouse. However, in other systems like the Drosophila wing disc, the diffusion coefficients of Wg (a homologue of Wnt) and Dpp (a homologue of Bmp) have been measured with high precision [48]. This study revealed that Wg has a diffusion coefficient of $0.05\mu m^2/s$ and that Dpp diffuses two or three fold faster with a coefficient of $0.15\mu m^2/s$. These measurements are currently controversial and a recent study has estimated a much higher diffusion of Dpp $10\mu m^2/s$ [49]. Another study in Xenopus [50] has confirmed the fast diffusivity of Bmps and has proposed that its diffusion coefficient can be as fast as $15\mu m^2/s$. Finally, a recent study in Zebrafish [51] has shown that Nodal and Lefty (two molecules of the same family of Bmps, the TGF-β family) have diffusion coefficients with 14-fold difference and a maximum diffusivity of $18\mu m^2/s$ in the case of Lefty2. These results are in agreement with the requirement for a fast diffusing Bmp ($D_{bmp} \gg D_{wnt}$) that was identified by our analysis.

To test weather our minimal BSW network (T_1 in Figure 10) can form a Turing pattern with realistic Bmp and Wnt diffusion coefficients, we analyze how the Turing space changes when the ratio between the diffusions of Bmp and Wnt ($\frac{D_{bmp}}{D_{wnt}}$) is changed. The system of PDEs of the BSW model with explicit signs for the rates k_i writes:

$$\begin{aligned}
\frac{\partial sox9}{\partial t} &= k_2 bmp - k_3 wnt \\
\frac{\partial bmp}{\partial t} &= -k_4 sox9 - k_5 bmp + D_{bmp}\nabla^2 bmp \\
\frac{\partial wnt}{\partial t} &= -k_7 sox9 - k_9 wnt + D_{wnt}\nabla^2 wnt
\end{aligned} \tag{13}$$

we normalize this system with respect to the diffusion of wnt by dividing the diffusion coefficients of bmp and wnt by D_{wnt}, we obtain:

$$\begin{aligned}
\frac{\partial sox9}{\partial t} &= k_2 bmp - k_3 wnt \\
\frac{\partial bmp}{\partial t} &= -k_4 sox9 - k_5 bmp + \gamma d\nabla^2 bmp \\
\frac{\partial wnt}{\partial t} &= -k_7 sox9 - k_9 wnt + \gamma\nabla^2 wnt
\end{aligned} \tag{14}$$

where $d = \frac{D_{bmp}}{D_{wnt}}$ is the ratio between the two diffusion constants and γ is a new term that we introduced to scale both diffusions. If we set the parameters k_i as in Table ST4 and set $\gamma = 1$, the diffusion-driven instability conditions (5), (8) are satisfied when $d > 1.25197$.

k_2	k_3	k_4	k_5	k_7	k_9
1	1	1.59	0.1	1.27	0.1

Table ST4: Reaction parameters of the BSW model

Therefore the minimum limit for d agrees with the diffusion difference of two and three fold ($d = 2, d = 3$) that was measured in the Drosophila wing. However, it is well known that as d decreases the parameter space that gives rise to a Turing instability also decreases. This could question the robustness

of the system when it is closed to low values of d. To investigate how the Turing parameter space changes when d is changed, we use a non-dimensionalized version of system (14) obtained by dividing all the rates k_i by k_2:

$$\begin{aligned}\frac{\partial sox9}{\partial t} &= bmp - k_3' wnt \\ \frac{\partial bmp}{\partial t} &= -k_4' sox9 - k_5' bmp + \gamma d \nabla^2 bmp \\ \frac{\partial wnt}{\partial t} &= -k_7' sox9 - k_9' wnt + \gamma \nabla^2 wnt\end{aligned} \tag{15}$$

where $k_3' = \frac{k_3}{k_2}, k_4' = \frac{k_4}{k_2}, k_5' = \frac{k_5}{k_2}, k_7' = \frac{k_7}{k_2}$ and $k_9' = \frac{k_9}{k_2}$. Assuming $k_i' > 0, i \in \{3,4,5,7,9\}$, the system (15) satisfy the conditions (5), (8) in three different cases depending on k_4', k_5' and k_9' :

1. $\mathbf{k_5' < k_9'} \quad \& \quad k_4' \leq -\frac{{k_5'}^2 k_9'}{k_5' - k_9'} \quad \& \quad k_3' < \frac{k_4' k_9'}{k_5' k_7'} \quad \& \quad d > \frac{k_4'}{k_3' k_7'}$
2. $\mathbf{k_5' < k_9'} \quad \& \quad k_4' > -\frac{{k_5'}^2 k_9'}{k_5' - k_9'} \quad \& \quad k_3' < \frac{k_4' k_5' + {k_5'}^2 k_9' + k_5' {k_9'}^2}{k_7' k_9'} \quad \& \quad d > \frac{k_4'}{k_3' k_7'}$
3. $\mathbf{k_5' \geq k_9'} \quad \& \quad k_3' < \frac{k_4' k_9'}{k_5' k_7'} \quad \& \quad d > \frac{k_4'}{k_3' k_7'}$

If we consider the third case (3.) and we impose the simple condition $k_5 = k_9$, we can simplify the diffusion-driven instability conditions to:

$$k_3' < \frac{k_4'}{k_7'} \quad \& \quad d > \frac{k_4'}{k_3' k_7'} \tag{16}$$

We can now study how the Turing space (16) changes when the ratio between the diffusion constants d is changed. To perform this analysis, we consider three cases with $d = 1.5$, $d = 2.5$, $d = 4$ and calculate the volume of the Turing space (16) when k_3', k_4', k_7' are varied in the range $[0, 5]$. As in the previous analysis this range represents a biologically plausible five fold difference between the kinetic rates k_i'. The volume is calculated using a numerical method to calculate multiple integrals provided by Mathematica. The results, shown in Figure 11A, confirm that that the Turing space increases when the difference d is increased.

In particular, we observe that when $d = 1.5$ the parameter space is small (volume $\mathbf{v} \approx 9.58$) and the rates k_3', k_4', k_7' can change less than one fold within the Turing space. The situation improves when $d = 2.5$ and the parameter space doubles (volume $\mathbf{v} \approx 18.74$). In this case the rates k_3', k_4', k_7' can change of two fold within the Turing space. Similarly, when $d = 4$ the parameter space increases (volume $\mathbf{v} \approx 24.82$) and the rates k_3', k_4', k_7' can change of almost three fold within the Turing space. Finally we perform for each case a numerical simulation using the parameters in Table ST4 on a domain of of 40 space units, see Figure 11B. We can observe that as d increases the amplitude of the Turing pattern become larger. This is also shown by the larger maximum eigenvalues σ_{max} shown in the dispersion relations in Figure 11B that imply a faster appearance of the Turing patterns. The wavenumber k_{max} becomes slightly smaller when d increases, however we do not observed dramatic changes in the wavelength of the patterns in the one-dimensional simulations. A much stronger change in wavelength can be induced by changing both diffusion constants with the parameter γ.

To summarize, our analysis reveals that the BSW model can form a relatively robust Turing pattern with a difference in diffusivity of two and a half ($d = 2.5$) between Bmp and Wnt. This agrees with the best estimation for diffusion coefficients of Wg (homologous of Wnt) and Dpp (homologous of Bmp) that has been performed in the developing Drosophila wing [48].

Finally, we calculate a realistic value for the parameter γ that represents the absolute magnitude of both diffusion coefficients. Our model uses minutes (min) as time units and micrometers (μm) as spatial

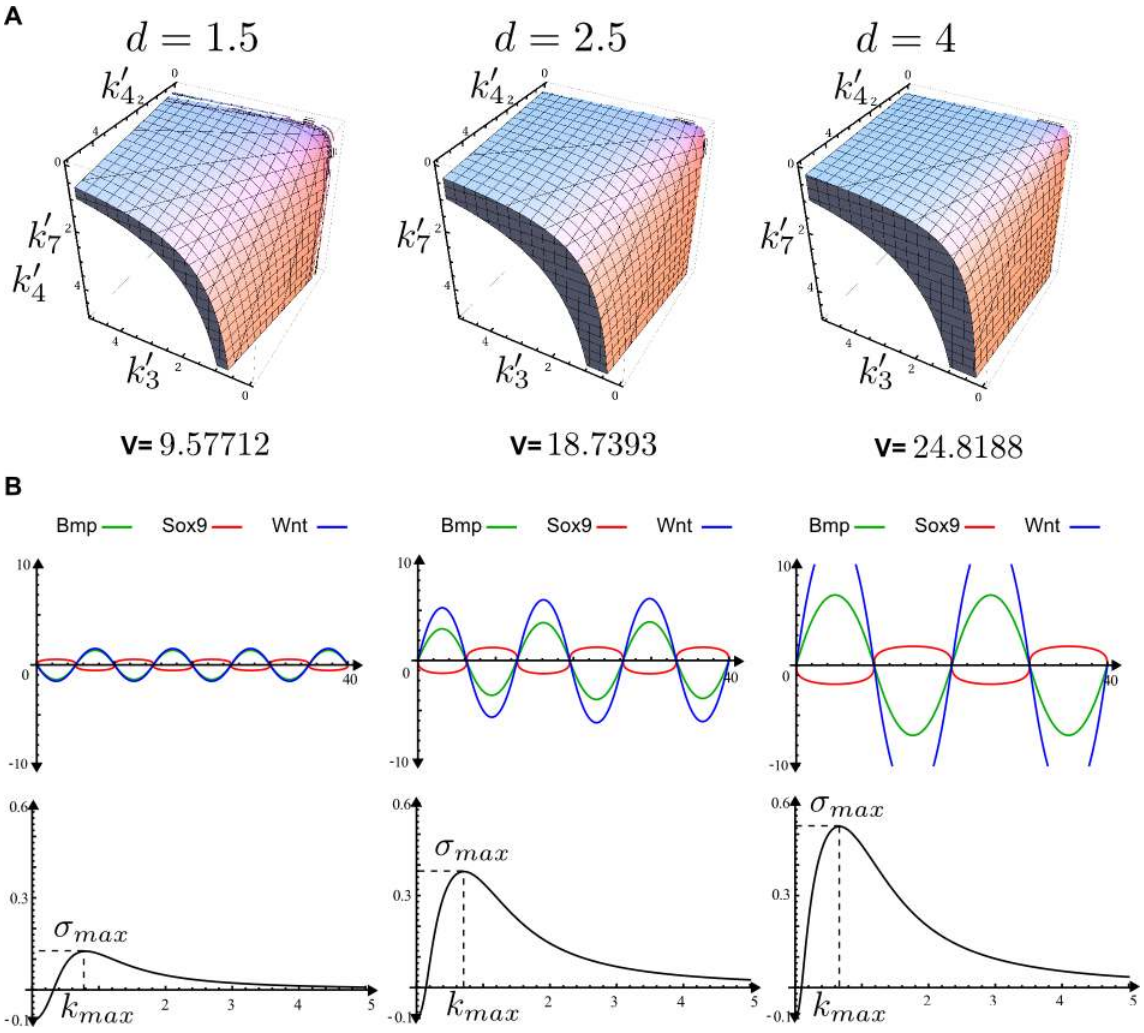

Figure 11: A) From left to right, Turing space (16) with $d = 1.5$ $d = 2.5$ $d = 4$ respectively, the volume $\mathbf{v}$ of the parameter space in the interval $k'_3, k'_4, k'_7 = ([0,5],[0,5],[0,5])$ is shown below the graphs. B) From left to right, on the first row numerical simulations on a 40 space unit one-dimensional domain with parameters in Table ST4 $d = 1.5$ $d = 2.5$ $d = 4$ respectively. On the second row the dispersion relations highlight an increasing maximum eigenvalue σ_{max} when d is increased.

units. If we convert to our units the two most recent estimations of the Dpp diffusion in Drosophila [49] and Bmp in Xenopus [50] we obtain respectively: $600\mu m^2/min$ and $900\mu m^2/min$. According to this values, we set our parameter $\gamma = 250$ so that with the plausible ratio $d = 2.5$ between the diffusion of Bmp and Wnt determines a Bmp diffusion of $D_{bmp} = \gamma \cdot d = 250 \cdot 2.5 = 625\mu m^2/min$.

2.5 Interpretation of the main feedbacks of the model

In the BSW model, the mutual inhibition between Sox9 and Wnt is required to form a periodic pattern of Sox9 that is out-of-phase of Wnt, see Figure 12A. Similarly, the negative feedback from Sox9 to Bmp is required to form a periodic pattern of Sox9 that is out phase of Bmp, see Figure 12B. Nevertheless, when we compare the periodic pattern formed by this model with the patterns presented Figure 2 (main text) the interpretation of the two negative feedbacks is profoundly different. The *bmp*-node represents the expression of the Bmp2 mRNA (see Figure 12B) and its diffusible gene product (the BMP2 ligand). The negative feedback from Sox9 (k_4) thus represents transcriptional repression of the Bmp2 gene. By contrast, our microarray data show that the Wnt genes are not differentially expressed. Instead it is the signalling pathway, as represented by active β-catenin, which is regulated spatially. The *wnt*-node thus represents the active WNT ligand (as shown by act-βcat, see Figure 12A), and the negative feedback from Sox9 (k_7) reflects an inhibition of the ligand activity.

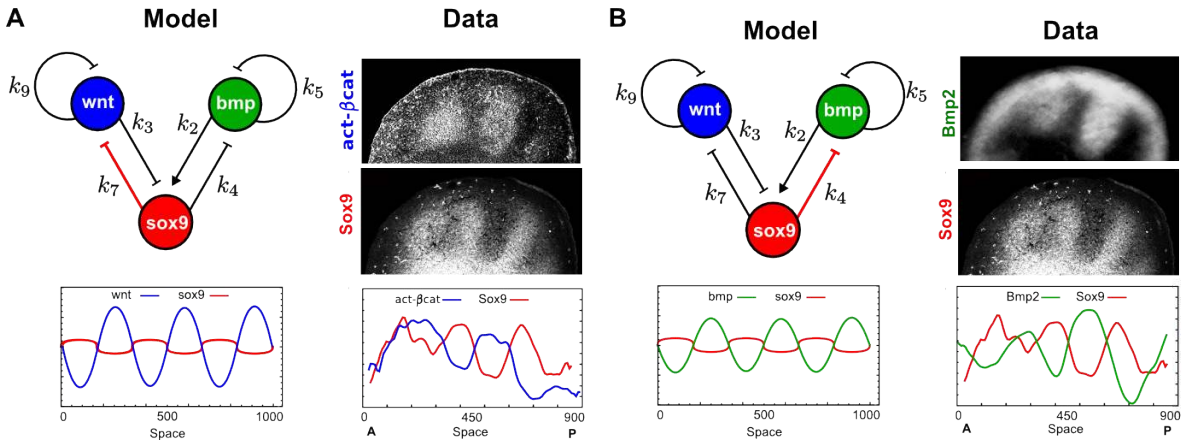

Figure 12: A) On the left, the feedback from Sox9 to Wnt (red line) is required to form a Sox9 pattern that is out of phase of Wnt. On the right, an immuno against active β-catenin (act-βcat) shows that Wnt signaling is opposite to Sox9. B) On the left, the feedback from Sox9 to Bmp (red line) is required to form a Sox9 pattern that is out of phase of Bmp. On the right, an in-situ of Bmp2 shows that Bmp2 expression is opposite to Sox9.

The difference between the interaction k_7 and k_4 becomes explicit if we consider an extended model which represents the Bmp-mRNA (*bmp*), the Bmp protein (BMP), the Wnt-mRNA (*wnt*), the Wnt protein (WNT), a Wnt signaling inhibitor (WI) and a node that represents both the mRNA and protein of Sox9 (*sox*9), see Figure 13A. The reactants in capital letters (BMP,WNT,WI) are diffusible and the other reactants (*bmp*,*sox*9,*wnt*) are not.

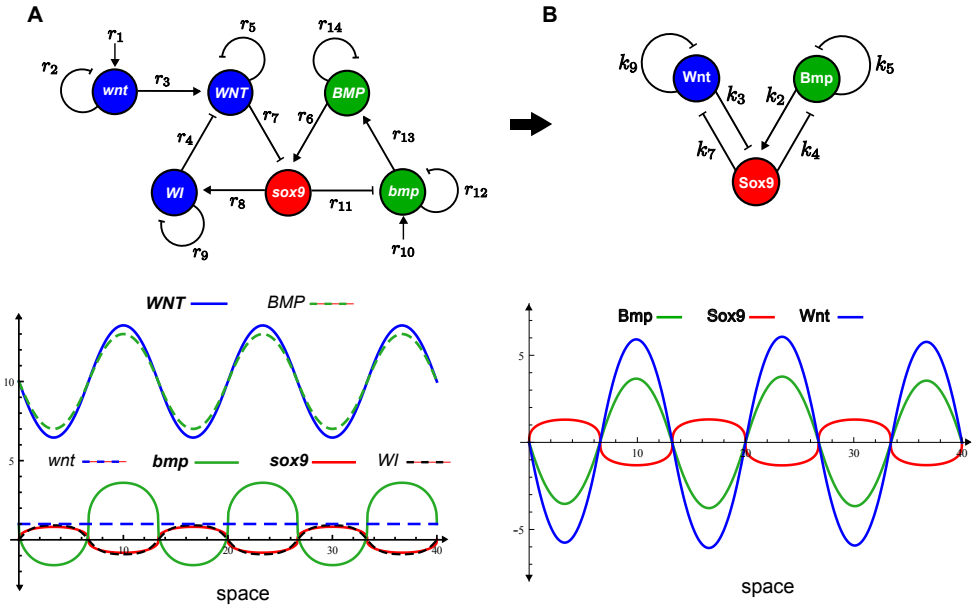

Figure 13: A) On top, the extended model which considers six reactants: Bmp-mRNA (*bmp*), the diffusible Bmp protein (BMP), the Wnt-mRNA (*wnt*), the diffusible Wnt protein (WNT), a diffusible Wnt signaling inhibitor (WI) and Sox9 (*sox*9). On the bottom, results of a one-dimensional simulation on a space of 40 square units at time $t = 3500$. Both WNT, BMP and *bmp* are out of phase of Sox9. The Wnt-mRNA (*wnt*) is uniform, in agreement with our microarray data, and the Wnt signaling inhibitor WI is in-phase with Sox9. B) On top, the network of the minimal BSW model identified in section 2.3.4 that recapitulates the patterns of Bmp expression, Sox9 and Wnt signaling (below).

A linear implementation of the topology in Figure 13A writes:

$$\begin{aligned}
\frac{\partial wnt}{\partial t} &= r_1 - r_2 wnt \\
\frac{\partial WNT}{\partial t} &= r_3 wnt - r_4 WI - r_5 WNT + D_{WNT}\nabla^2 WNT \\
\frac{\partial sox9}{\partial t} &= r_6 BMP - r_7 WNT \\
\frac{\partial WI}{\partial t} &= r_8 sox9 - r_9 WI + D_{WI}\nabla^2 WI \\
\frac{\partial bmp}{\partial t} &= r_{10} - r_{11} sox9 - r_{12} bmp \\
\frac{\partial BMP}{\partial t} &= r_{13} bmp - r_{14} BMP + D_{BMP}\nabla^2 BMP
\end{aligned} \tag{17}$$

If we set $D_{WI} = 0$ (discussed in the next section) and assume that the dynamics of the non diffusible species wnt, bmp, WI are fast, we can take quasi-steady state approximation (QSS) that assumes that

wnt, bmp and WI are in quasi-equilibrium:

$$\frac{\partial wnt}{\partial t} = 0 \quad \rightarrow \quad wnt = \frac{r_1}{r_2} \tag{18}$$

$$\frac{\partial WI}{\partial t} = 0 \quad \rightarrow \quad WI = \frac{r_8}{r_9} sox9 \tag{19}$$

$$\frac{\partial bmp}{\partial t} = 0 \quad \rightarrow \quad bmp = \frac{r_{10}}{r_{12}} - \frac{r_{11}}{r_{12}} sox9 \tag{20}$$

if we substitute (18),(19),(20) in (17) we can reduced the system to:

$$\begin{aligned} \frac{\partial sox9}{\partial t} &= r_6 BMP - r_7 WNT \\ \frac{\partial BMP}{\partial t} &= \frac{r_{10} r_{13}}{r_{12}} - \frac{r_{13} r_{11}}{r_{12}} sox9 - r_{14} BMP + D_{BMP} \nabla^2 BMP \\ \frac{\partial WNT}{\partial t} &= r_3 wnt - \frac{r_4 r_8}{r_9} sox9 - r_5 WNT + D_{WNT} \nabla^2 WNT \end{aligned} \tag{21}$$

The system (21) is equivalent to the system (13) when:

$$r_6 = k_2, \quad r_7 = k_3, \quad \frac{r_{13} r_{11}}{r_{12}} = k_4, \quad \frac{r_4 r_8}{r_9} = k_7, \quad r_{14} = k_5, \quad r_5 = k_9 \tag{22}$$

To confirm that the two models are equivalent we perform a numerical simulation of (17). Starting from the parameters in Table (ST4) we use the conditions (22) to derive parameters for the system (17) to produce a diffusion-driven instability:

r_1	r_2	r_3	r_4	r_5	r_6	r_7	r_8	r_9	r_{10}	r_{11}	r_{12}	r_{13}	r_{14}
1	1	1	1	0.1	1	1	1.27	1	1	1.59	1	1	0.1

Table ST5: Parameter set for the system (17)

where r_1, r_2, r_3, r_{10} are set to obtain the homogeneous steady state:

$$(wnt_0, WNT_0, sox9_0, WI_0, bmp_0, BMP_0) = (1, 10, 0, 0, 1, 10.) \tag{23}$$

Finally we simulate the system on a one-dimensional domain of 40 space units by using the parameters in Table ST5 setting $D_{WI} = D_{WNT} = 1, D_{BMP} = 4$. We begin the simulation from a slight random perturbation (1% of noise) of the homogeneous steady state (23). Similarly to the other numerical simulations, we add saturations terms in order to limit the unbounded growth of the system. This is done by adding two negative cubic terms to $sox9$ and WI by rewriting (17) as follows:

$$\frac{\partial sox9}{\partial t} = r_6 BMP - r_7 WNT - \mathbf{sox9^3} \tag{24}$$

$$\frac{\partial WI}{\partial t} = r_8 sox9 - r_9 WI - \mathbf{WI^3} + D_{WI} \nabla^2 WI \tag{25}$$

The result of the simulation at time $t = 3500$ is shown in Figure 13A. In agreement with our analysis, the simulation shows a pattern of $sox9$ that is out of phase of WNT, bmp and BMP. In contrast, the pattern of the Wnt inhibitor (WI) is in phase of Sox9, while the pattern of the Wnt mRNA (wnt) is ubiquitous. In the next two subsections we discuss and analyze the two main negative feedbacks of this model.

2.5.1 Inhibition of Wnt by Sox9

The immuno-staining against active β-catenin shown in Figure 2A (main text) shows that WNT signaling is out of phase of Sox9. In addition, the BSW model suggests that a negative feedback from Sox9 to Wnt is required to obtain a Sox9 pattern that is out of phase of Wnt. Taken together, these two pieces of evidence predict that Sox9 must have a negative influence on the ligands that are mediating canonical Wnt signaling in the limb. Since Sox9 is a transcription factor and can only act inside the cell, the simplest interpretation of our model is that Sox9 must promote a secreted molecule that inhibits canonical Wnt signaling in the extracellular environment.

In agreement with this prediction, the analysis presented in the previous section shows that a detailed model that considers a Wnt signaling inhibitor WI promoted by Sox9 can be easily reduced to the BSW topology. When this model is simulated in a one-dimensional domain, a Sox9 pattern that is out of phase of the Wnt proteins is formed, see the graph in Figure 13A. This simulation is performed by setting a diffusion constant $D_{WI} = 1$. According to this simulation good candidates for the Wnt signaling inhibitor WI could be any diffusible molecules that inhibit Wnts and have an expression pattern that is in phase with Sox9.

Interestingly, we found that even when the inhibitor WI does not diffuse ($D_{WI} = 0$) similar periodic patterns can still be obtained, see the simulation in Figure 14A. This simulation suggests that from a broader point of view any cell autonomous mechanism that interferes with a diffusible aspect of Wnt signaling could be a possible candidate for the inhibitor WI. This includes for example membrane bound molecules that may sequester Wnt ligands or cellular/molecular mechanism that may prevent Wnt diffusion. It is important to notice, that although the WI can be cell-autonomous its ultimate target must be a diffusible component of the Wnt pathway. For example, a model where Sox9 inhibits only a cell-autonomous Wnt signaling cascade component (E.g. β-catenin) is not able to produce Turing pattern, see the example in Figure 14B. In the network shown Figure 14A, such feedback was provided by the interactions r_4, r_8, that together have a negative influence on the diffusible node of Wnt (WNT).

The Wnt pathway is known to be regulated by a variety of extracellular antagonists that prevent ligand-receptor interactions [52]. Some of these antagonists bind directly to Wnt proteins, like sFRP-family and WIF, while others like the Dkk family alter the Wnt receptor activity. In our microarray analysis we identified various diffusible Wnt inhibitors, namely Dkk1, Wif1, Apcdd1, Dkk2, Dkk3, Igfbp5, Sfrp2, Sfrp1, Shisa2 and Sulf1 (Figure S1A). From these, the last seven are differentially expressed in Sox9+ cells. We have analyzed their expression patterns by WMISH and found that Sfrp2, Shisa2 and Sulf1 have digital expression (Figure S1B).

Shisa proteins regulate the post-translational modification and trafficking to the cell surface of WNT and FGF receptors [53]. This implements a cell autonomous inhibition of Wnt signaling that cannot be reconciled with the requirements of our model.

Sfrp1, Sfrp2 and Sfrp3 are expressed in early stages of limb development while Sfrp4 and Sfrp5 in later stages [54]. They are known diffusible inhibitors of WNT, with a cysteine-rich domain that binds to WNT molecules. Knockout mutants usually have mild brachy-syndactilities and polydactyly [55]. Double mutants have more severe phenotypes suggesting that there is functional redundancy [56]. A triple knockout of Sfrp1, Sfrp2 and Sfrp5 leads to fused somites formation in early-somite mouse embryos [57] but impaired embryo development impedes the study of limb phenotypes. Sfrps are good candidates as extracellular inhibitors in our model. Moreover, Sfrp3 is expressed in chondrogenic condensations in chick [58] and could act as an antagonist of Wnt-signaling to allow chondrogenesis to proceed [59].

Finally Heparin Sulphate proteoglycans (HS) have been shown to control the distribution and binding to receptors of several growth factors such as BMPs, WNTs and FGFs [60,61]. Secreted 6-O-endosulfatases Sulf1 and Sulf2 can alter HS [62] by changing their binding affinities to diffusible growth factors thus contributing to inhibition or activation of signaling depending on the biological context. Indeed, while in C2C12 cells, quail Sulf1 promoted Wnt signaling by releasing WNT ligands from HS [63], Sulf1 transcript variant B inhibited Wnt signaling in quail embryos [64]. We found that Sulf1 is expressed in the digits very early and hypothesize that it could also contribute to extracellular inhibition of Wnt in the digits. Indeed Sulf1 was shown to promote chondrogenesis and mesenchymal condensation in micromass cultures contrary to the effect of WNT proteins [65].

In summary, there appear to be many candidate molecules which could inhibit Wnt signaling, making it difficult to determine the exact mechanism. Since many single knock-outs have only mild phenotypes it is likely that multiple molecules could take this role, thus conferring robustness to the system.

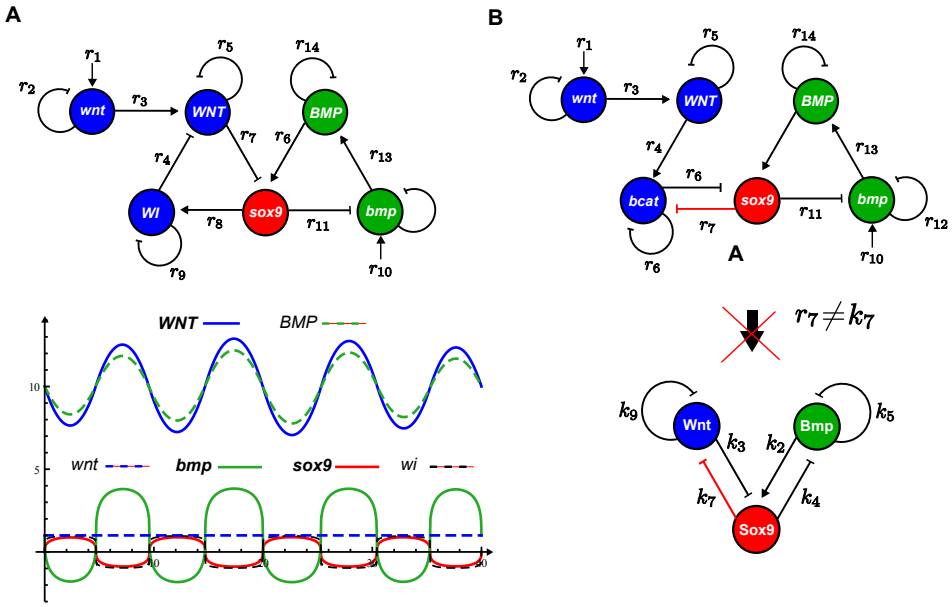

Figure 14: A) On top, the five reactants extended model with a non-diffusible Wnt signaling inhibitor (WI). On the bottom, results of a one-dimensional simulation on a space of 40 square units at time $t = 3500$. The network forms regular periodic patterns even with a non-diffusible WNT signaling inhibitor. B) A network where Sox9 inhibits a cell-autonomous component of Wnt signaling, in the example β-catenin (*bcat*). This model does not form a Turing instability and does not reduce to a BSW model because its inhibition from Sox9 to *bcat* (interaction r_7) is not equivalent to the inhibition from Sox9 to WNT (interaction k_7) in the BSW model.

2.5.2 Inhibition of Bmp by Sox9

The in situ hybridizations of Bmp2 shown in Figure 2A (main text) revealed that, as soon as the digit pattern forms, Bmp2 is expressed out of phase of Sox9. Nevertheless, previous studies [24-27] showed that Bmp-signaling promotes Sox9. How can Bmp-signaling promote Sox9 if the Bmps are expressed in Sox9 negative cells? This counter intuitive behavior is consistent with the patterning dynamics observed in the Substrate-Depletion model presented in Figure 1D (main text). In this mathematical model, despite the substrate (S) promoting the activator (A), the negative feedback from A to S leads over time to out-of-phase patterns of the two molecules, see Figure 15A. Similarly in the BSW model the negative feedback from Sox9 to Bmp leads over time to out-of-phase patterns of Bmp and Sox9 despite the fact that Bmp promotes Sox9, see Figure 15B. This explains how Bmp2 expression can be opposite to the Sox9 pattern although Sox9 is promoted by BMP signaling.

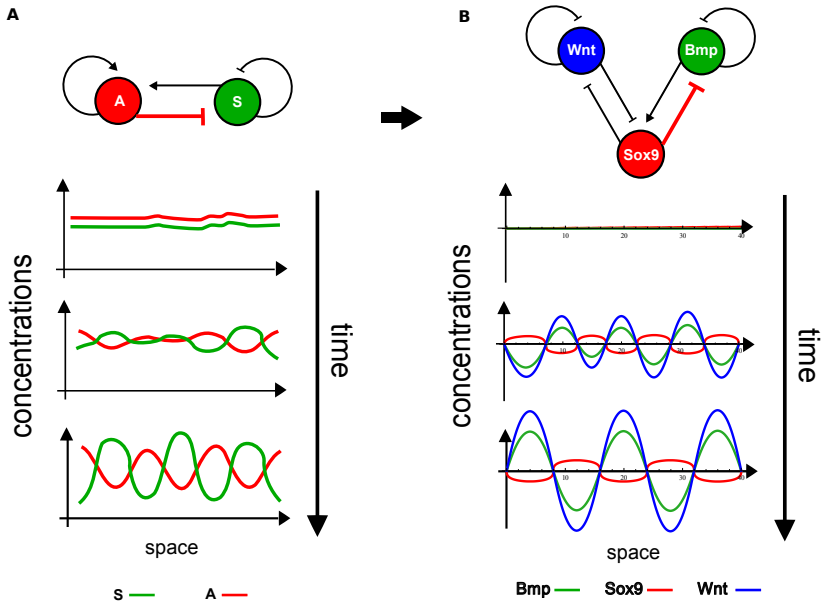

Figure 15: A) In the substrate-depletion model the negative feedback from the activator A to substrate S (interaction highlighted in red) implements an inhibition that over time leads to out-of-phase patterns of A and S, graphs at the bottom. B) In the BSW model, Bmp acts as a substrate promoting the activator Sox9. The inhibition from Sox9 to Bmp (interaction highlighted in red) over time leads to out-of-phase patterns of Bmp and Sox9, graphs at the bottom.

In Section 2.5 and Figure 16A we considered an extension of the basic BSW model to include more molecular players. This clarified that peaks of Bmp protein (BMP) are out-of-phase with Sox9 expression. Our experimental data however, shows that the pattern of phosphorylated Smad1/5/8 (and therefore Bmp-signaling) is in-phase with Sox9. How can pSmad display an opposite pattern with respect to the Bmp protein distribution? Again this reflects the non-intuitive nature of the Substrate-Depletion model, and extending the model to include another explicit molecular player helps to illustrate this. The pSmad-node directly regulates Sox9 expression (consistent both with our data, and the literature [24-27]), and just like Sox9 itself the negative feedback from Sox9 to Bmp-mRNA leads over time to out-of-phase patterns between pSMAD and BMP (see the simulation result in Figure 16B). Both the pSmad-node and the Sox9-node act like the activator (A) of the Substrate-Depletion model and develop an out-of-phase pattern from the substrate (S) (Bmp-node) (compare with Figure 15A). Thus the extended BSW substrate-depletion model can explain both the out-of-phase patterns between Sox9 and Bmp-mRNA (*bmp*), and between pSmad and the Bmp protein (BMP), see Figure 16C. This depends however on pSmad being part of the mutual inhibition between Sox9 and Wnt, which is implemented by Wnt signaling having a negative effect on pSmad, see interaction r_7 in Figure 16B. Consistent with this hypothesis, cross-talk between β-catenin and Bmp signaling has been observed in variety of systems [66]. Nevertheless, other interactions which auto-activate pSmad could explain the out-of-phase patterns between Bmp and its signaling. Similar as shown in section 2.5, this model can be easily reduced to the simple BSW model made of three reactants.

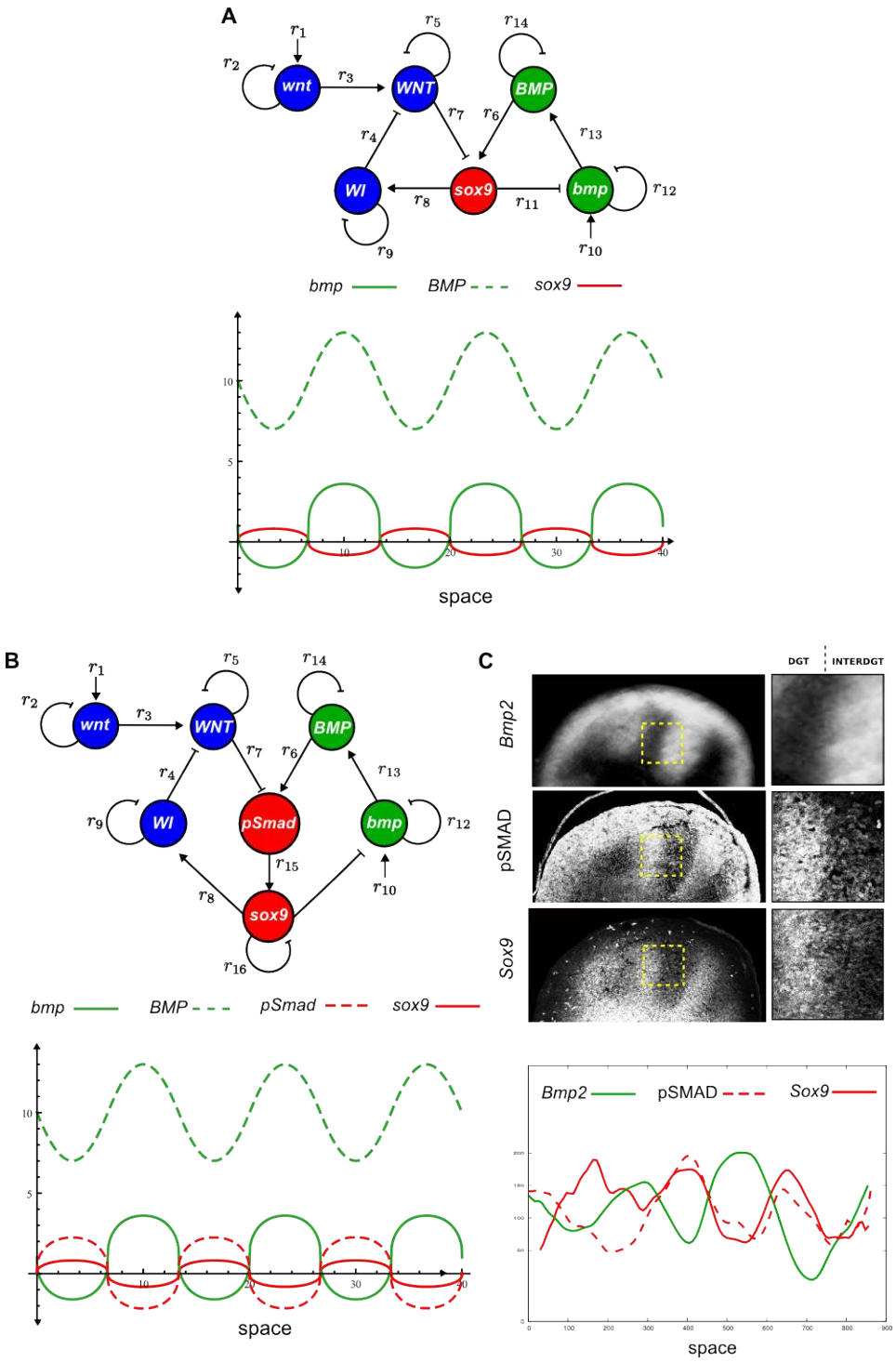

Figure 16: A) In the extended BSW model presented in in Section 2.5, despite the Bmp protein (BMP) activates sox9, the two genes have opposite patterns due to the negative feedback from Sox9 to Bmp-mRNA (bmp). B) Similarly, if we include a node that explicitly represents phosphorilated Smad1/5/8 (pSmad), despite the Bmp protein (BMP) activates pSmad, the two reactants have opposite patterns due to the negative feedback from Sox9 to Bmp-mRNA (bmp).

2.6 Introducing production rates to avoid negative values

The equations presented here will produce a Turing pattern, even if no background production rates are included. In this case the values of variables represents their deviation from the steady state which is zero. In other words, a negative value does not mean a negative concentration (which is impossible), but rather that the concentration is lower than the steady state. However, we here describe how the addition of production terms elevates the steady state such that all variables stay above zero. In this case the values could indeed be considered as real concentrations.

Let's consider the BSW model with explicit signs for the rates k_i and with the saturating cubic term $sox9^3$:

$$\begin{aligned}\frac{\partial sox9}{\partial t} &= k_2 bmp - k_3 wnt - sox9^3 \\ \frac{\partial bmp}{\partial t} &= -k_4 sox9 - k_5 bmp + \gamma d \nabla^2 bmp \\ \frac{\partial wnt}{\partial t} &= -k_7 sox9 - k_9 wnt + \gamma \nabla^2 wnt\end{aligned} \tag{26}$$

where γ is a scaling term for the diffusion constants and $d = \frac{D_{bmp}}{D_{wnt}}$.
This system has homogeneous steady state $(sox9_0, bmp_0, wnt_0) = (0, 0, 0)$. When the system is simulated in a one-dimensional space of 40 units with parameters in Table ST4, $\gamma = 1$ and $d = 2.5$, it forms periodic patterns whose values are centered around the homogeneous steady state and range in the intervals [-1.5,1.5],[-5,5],[-8,8] for $sox9, bmp$ and wnt respectively, see Figure 17A. In this case there are no production rates, the concentrations of $sox9, bmp$ and wnt should not be interpreted as absolute values but as relative shifts from the homogeneous steady state. Negative concentrations therefore represent a relative shifting towards concentrations that are lower than the homogeneous steady sate. The negative concentrations can be avoided by introducing production terms to shift the homogeneous steady state up to higher values. Let us rewrite the system (26) by including three production terms $\alpha_{sox9}, \alpha_{bmp}$ and α_{wnt} different from zero:

$$\begin{aligned}\frac{\partial sox9}{\partial t} &= \alpha_{sox9} + k_2 bmp - k_3 wnt - (sox9 - sox9'_0)^3 \\ \frac{\partial bmp}{\partial t} &= \alpha_{bmp} - k_4 sox9 - k_5 bmp + \gamma d \nabla^2 bmp \\ \frac{\partial wnt}{\partial t} &= \alpha_{wnt} - k_7 sox9 - k_9 wnt + \gamma \nabla^2 wnt\end{aligned} \tag{27}$$

where the saturation term $sox9^3$ is rewritten as $(sox9 - sox9'_0)^3$ to saturate symmetrically around the new homogeneous steady state that writes:

$$\begin{aligned}sox9'_0 &= -\frac{-k_5 k_9 \alpha_{sox9} - k_2 k_9 \alpha_{bmp} + k_3 k_5 \alpha_{wnt}}{k_2 k_4 k_9 - k_3 k_5 k_7} \\ bmp'_0 &= -\frac{k_4 k_9 \alpha_{sox9} + k_3 k_7 \alpha_{bmp} - k_3 k_4 \alpha_{wnt}}{k_2 k_4 k_9 - k_3 k_5 k_7} \\ wnt'_0 &= -\frac{k_5 k_7 \alpha_{sox9} + k_2 k_7 \alpha_{bmp} - k_2 k_4 \alpha_{wnt}}{k_2 k_4 k_9 - k_3 k_5 k_7}\end{aligned} \tag{28}$$

We solve this system to find the values of $\alpha_{sox9}, \alpha_{bmp}$ and α_{wnt} and obtain:

$$\begin{aligned}\alpha_{sox9} &= -k_2 bmp'_0 + k_3 wnt'_0 \\ \alpha_{bmp} &= k_4 sox9'_0 + k_5 bmp'_0 \\ \alpha_{wnt} &= k_7 sox9'_0 + k_9 wnt'_0\end{aligned} \tag{29}$$

This allows us to derive for any given steady state $(sox9'_0, bmp'_0, wnt'_0)$ and rates k_i the production terms $\alpha_{sox9}, \alpha_{bmp}$ and α_{wnt}. For example if we use the rates k_i in Table ST4 and set a homogeneous steady state to $(sox9'_0, bmp'_0, wnt'_0) = (5, 10, 10)$ we obtain:

$$\begin{aligned} \alpha_{sox9} &= 0 \\ \alpha_{bmp} &= 8.95 \\ \alpha_{wnt} &= 7.35 \end{aligned} \tag{30}$$

As expected, with these production rates a numerical simulation of the system (27) on a one-dimensional domain of 40 units shows only positive concentration of $sox9, bmp$ and wnt, see Figure 17B. The one-dimensional simulation in Figure 2B (main text) are performed with the parameters in Table ST4, $\gamma = 400$ and $d = 2.5$, and by setting the production rates to $\alpha_{sox9} = 0, \alpha_{bmp} = 16.9$ and $\alpha_{wnt} = 13.7$ in order to have the homogeneous steady state $(sox9'_0, bmp'_0, wnt'_0) = (10, 10, 10)$. In the numerical simulations that are presented in the following sections, we derive $\alpha_{sox9}, \alpha_{bmp}$ and α_{wnt} in the same way by solving the homogeneous steady state system.

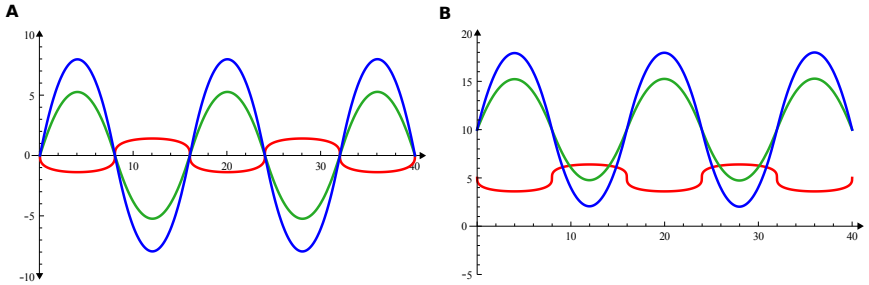

Figure 17: A) Results of a simulation of the system (26) on a one-dimensional domain of 40 units at $t = 3500$. The periodic patterns are centered around the homogeneous steady state $(sox9_0, bmp_0, wnt_0) = (0, 0, 0)$. B) Results of a simulation of the system (27) one-dimensional domain of 40 units at $t = 3500$. The production rates (30) shift the homogeneous steady state to $(sox9'_0, bmp'_0, wnt'_0) = (5, 10, 10)$ making all the concentrations positive.

2.7 The BSW model

In summary, our analysis identified a three-reactant reaction-diffusion model that:

1. Fits the patterns of Sox9, Wnt signaling and Bmp expression
2. Is in agreement with the known regulation between Sox9 and Bmp-signaling [24-27]
3. Is in agreement with the known regulation between Sox9 and Wnt signaling [21-23]
4. Is able to form a pattern with realistic diffusion coefficients of Bmps and Wnts.
5. Produces positive concentration values for Sox9, Wnt and Bmp.

We named this reaction-diffusion model the Bmp-Sox9-Wnt model (BSW) and use the following equations and parameters as a starting point for further analysis:

$$\begin{aligned}\frac{\partial sox9}{\partial t} &= \lambda(\alpha_{sox9} + k_2 bmp - k_3 wnt - (sox9 - sox9'_0)^3) \\ \frac{\partial bmp}{\partial t} &= \lambda(\alpha_{bmp} - k_4 sox9 - k_5 bmp) + \gamma d \nabla^2 bmp \\ \frac{\partial wnt}{\partial t} &= \lambda(\alpha_{wnt} - k_7 sox9 - k_9 wnt) + \gamma \nabla^2 wnt\end{aligned} \tag{31}$$

where λ is a coefficient that scales the reaction part and where the production terms are calculated according to (29).

k_2	k_3	k_4	k_5	k_7	k_9	γ	d	λ
1	1	1.59	0.1	1.27	0.1	250	2.5	0.6

Table ST6: Parameter set for the BSW model

2.8 The BSW model in 2D

In order to investigate the behavior of the BSW model in two dimensions, we simulated the system (31) on a triangular square grid with edge length of 32000 space units and made of 18976 triangles. With the parameters in Table ST6 which consider realistic diffusion coefficients (see Section 2.4) this system produces a Sox9 pattern of randomly oriented stripes that are out of phase of Bmp and Wnt, see Figure 18. This pattern is reminiscent of the patterns formed by mesenchymal cells in in vitro Micromass cultures, see Figure S3.

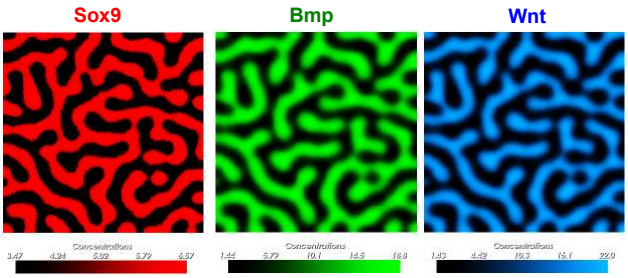

Figure 18: Simulation of the BSW system (31) on a triangular square grid with edge length of 32000. With the parameters in Table ST4, $\gamma = 250$, $d = 2.5$, and the production terms given in (30), the system forms a labyrinthine Sox9 pattern that is out of phase of Bmp and Wnt ($t = 300$). Also see Figure S3.

Thanks to the symmetric saturation given by the term $-(sox9 - sox9'_0)^3$, the system (31) always forms stripes. Spots can be formed by introducing a squared saturation term $\delta(sox9 - sox9'_0)^2$ that makes the Sox9 saturation stronger either above or below the homogeneous steady state depending on the sign of δ. In the first case the model forms spots while in the second case it forms reversed spots

(highly connected stripes of Bmp and Wnt). This can be easily seen by rewriting the system (31) as:

$$\begin{aligned}
\frac{\partial sox9}{\partial t} &= \lambda(\alpha_{sox9} + k_2 bmp - k_3 wnt - (sox9 - sox9'_0)^3 + \delta(sox9 - sox9'_0)^2) \\
\frac{\partial bmp}{\partial t} &= \lambda(\alpha_{bmp} - k_4 sox9 - k_5 bmp) + \gamma d \nabla^2 bmp \\
\frac{\partial wnt}{\partial t} &= \lambda(\alpha_{wnt} - k_7 sox9 - k_9 wnt) + \gamma \nabla^2 wnt
\end{aligned} \tag{32}$$

and by performing a numerical simulation on a square domain where the parameter δ is varied along the x axis. Figure 19A shows a simulation with the parameters in Table ST6 where δ is linearly varying in the range (2,-2) along the x axis. This stimulates a progressive transitions from spots to reverse spots.

Similar results can be also obtained with the simpler BSW model (31) by changing the ratio between the production terms of bmp (α_{bmp}) and wnt (α_{wnt}). This changes the homogeneous steady state of the system and if we keep the cubic saturation centered on a certain value of Sox9 $(sox9 - sox9_c)^3$ implements an effective asymmetric saturation. This can be easily seen by simulating the system (31) on a squared domain where α_{bmp} and α_{wnt} increase along the x and the y axis of the domain respectively, see Figure 19B.

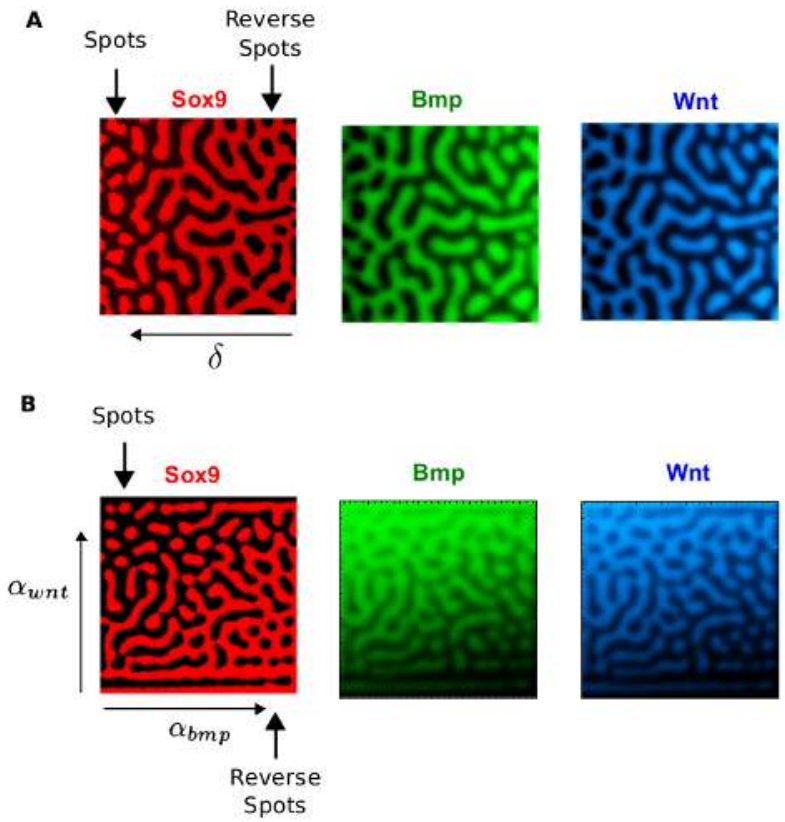

Figure 19: A) Simulation of the BSW system (32) on a triangular square grid with edge length of 32000. A progressive transition from spots to reverse spots is obtained with the parameters in Table ST6 by decreasing δ along the x axis in the range (2,-2). B) A simulation of the BSW system (31) on a triangular square grid with edge length of 32000. A progressive transition from spots to reverse spots is obtained with the parameters in Table ST6 and by progressively increasing the production terms α_{bmp},α_{wnt} along the x and the y axis respectively.

2.8.1 Stripe orientation and wavelength change

In a previous study [9], we characterized the behavior of a simple Activator-Inhibitor reaction-diffusion model, see Figure 20A, by plotting the maximum eigenvalue λ_{max} and the wavelength ω for each pair of reaction parameters across the Turing space, see Figure 20B. This analysis together with numerical simulations revealed that when the parameters f_u and g_u were increased and decreased (respectively) in a graded manner through space by Hox and Fgfs, the stripy pattern formed by the model could be oriented along the gradient, see Figure 20C.

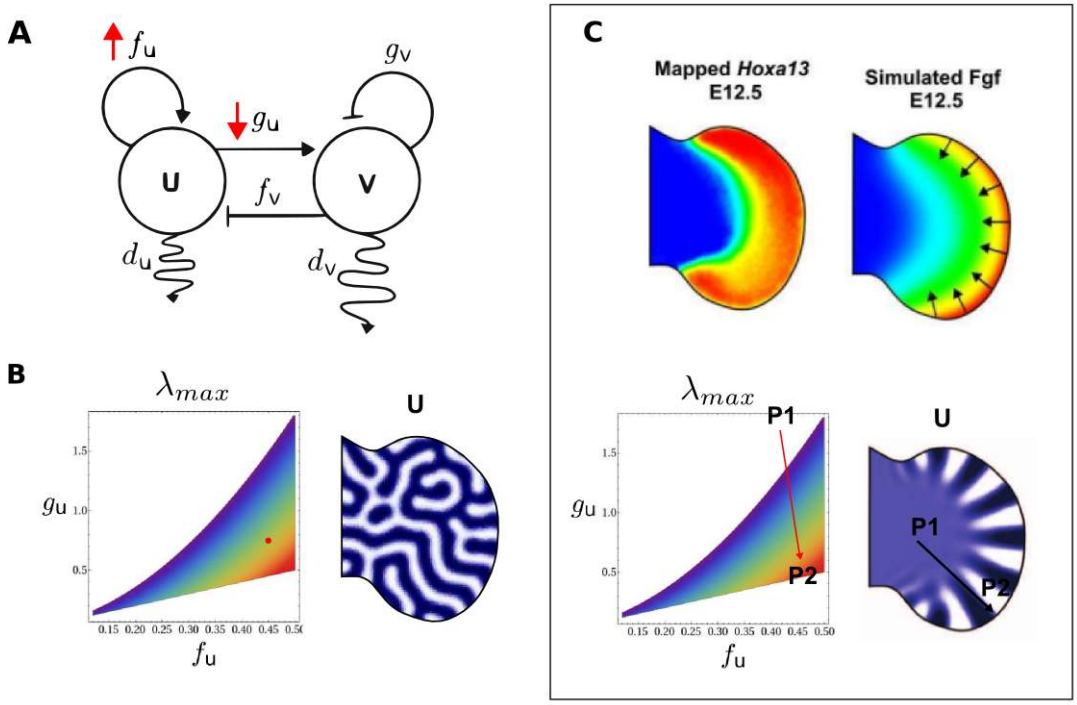

Figure 20: A) The network diagram of an Activator-Inhibitor model: f_u, f_v, g_u and g_v are the reaction rates which regulate the two diffusible reactants u and v. B) On the left, a graph shows the maximum eigenvalue λ_{max} across the Turing space as g_u and f_u are changed (blue and red corresponds to low and high values respectively. When the model is simulated with a parameter set inside the Turing space (red dot) it produces a labyrinthine pattern of randomly oriented stripes, simulation on the right. C) If Hox genes and an Fgf gradient are used to modulate the parameters g_u and f_u in a proximal-distal graded manner (from point P1 to point P2) the stripes align radially towards the distal tip assuming a digit-like conformation.

Here we perform a similar analysis to identify which parameters of the BSW model can be varied in a graded manner to orient the stripes and increase the wavelength. The results of this analysis are used to build the realistic growing simulation of limb digit patterning presented in the following sections and Figure 3 (main text). In the BSW model, the analytical derivation of λ_{max} and the wavelength ω is not possible. As an alternative, for each parameter couple, we perform a numerical simulation where the two parameters are changed along the x and the y axis of a squared domain. A similar approach was taken in

[67] to sample the behavior of the Gray-Scott reaction-diffusion model. On one hand, these simulations give an overview of the pattern changes across the parameter space (E.g the wavelength of the pattern). On the other hand, they give an idea of how spatially varying parameters can effect the pattern (E.g. if a graded parameter along x axis is able to align the stripes). The simulations are performed using the BSW model without production terms (26) and have as initial condition the homogeneous steady state $(sox9'_0, bmp'_0, wnt'_0) = (0, 0, 0)$. We consider the parameter set in Table ST6 except for the parameter d which is set to $d = 10$ to obtain a bigger Turing space (as shown in Section 2.4). Starting from this parameter set we allow only two parameters to vary linearly along the x and the y axis of a square grid with edge length of 32000 and 18976 triangles. The results can be represented with a single plot for each parameter pair that shows the final time point of the numerical simulation overlapped with the Turing instability region which is derived analytically, see the three examples in Figure 21B.

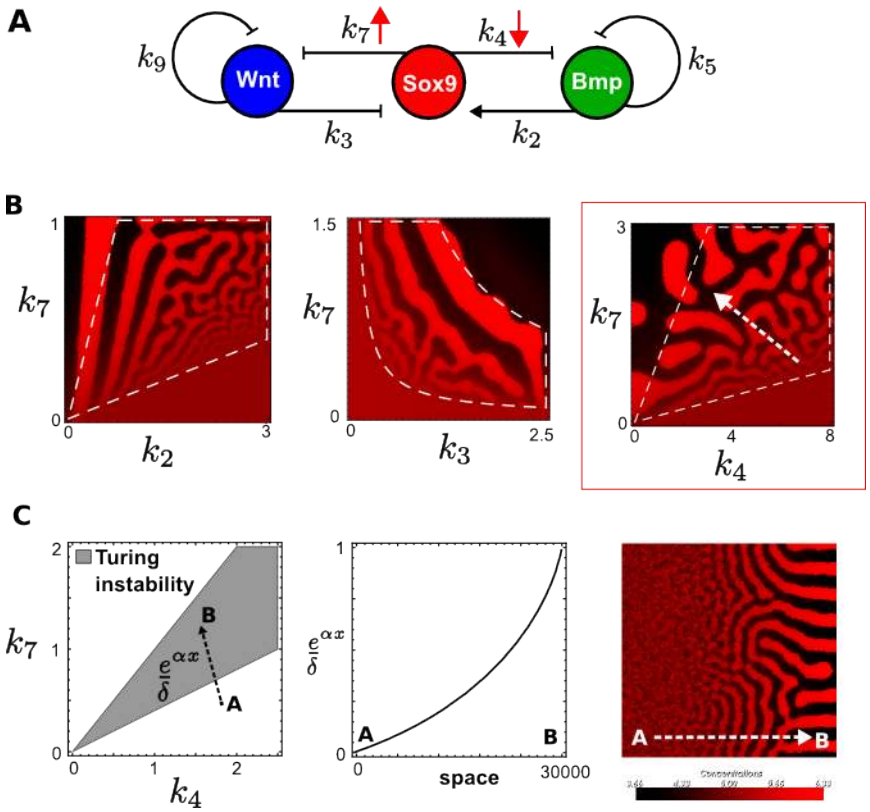

Figure 21: A) The network diagram of the BSW model. A decrease in the rate k_4 and an increase in the rate k_7 promote stripe orientation, see the red arrows. B) From left to right, graphs show the Turing space as $(k_2, k_7), (k_3, k_7)$ and (k_4, k_7) are varied, the white dashed lines outlines the Turing space. The graphs are overlapped with a simulation where the two rates are varies along the x and y axis. When k_4 is decreased and k_7 is increased (graph on the right) the wavelength increases and the patterns appears to align towards the direction of rate change (see the white dashed arrow). C) On the left, the Turing space of the BSW model with $d = 2.5$ as k_4 and k_7 are varied (gray region). The dashed arrow shows the change in k_4 and k_7 that is controlled by an exponential function (middle panel) to align the stripes along the x axis from point A to point B (simulation on the right).

Our computational screening predicted that when k_4 is decreased and k_7 is increased the wavelength of the patterns increases and more importantly that the stripes orient along the direction of change,

21B. Interestingly, similar to the results obtained in our previous work [9], these two rates represent the two interactions that depend on the concentration of the activator (u in the previous case and Sox9 in our new model) see Figure 20A and Figure 21A. This suggests that a decrease of the lateral inhibition strength (g_u and k_4) and an increase in the auto-activation strength (f_u and k_7) may represent a general strategy to align the stripes along a gradient. Other combinations of parameters (E.g. (k_2, k_7) and (k_3, k_7)) are able to successfully increase the wavelength but appear to orient the stripes in the opposite direction (parallel to the direction of change).

To evaluate our prediction we perform another simulation on the square grid using the BSW model (31) with the set in Table ST6 and $d = 2.5$. This time we decrease k_4 and increase k_7 only along the x axis by using an exponential function that represents a morphogen gradient profile, see the left and the middle graph in Figure 21C. The simulation confirms the prediction of our screening, showing that the stripes align along the x axis of the square and have an increasing wavelength.

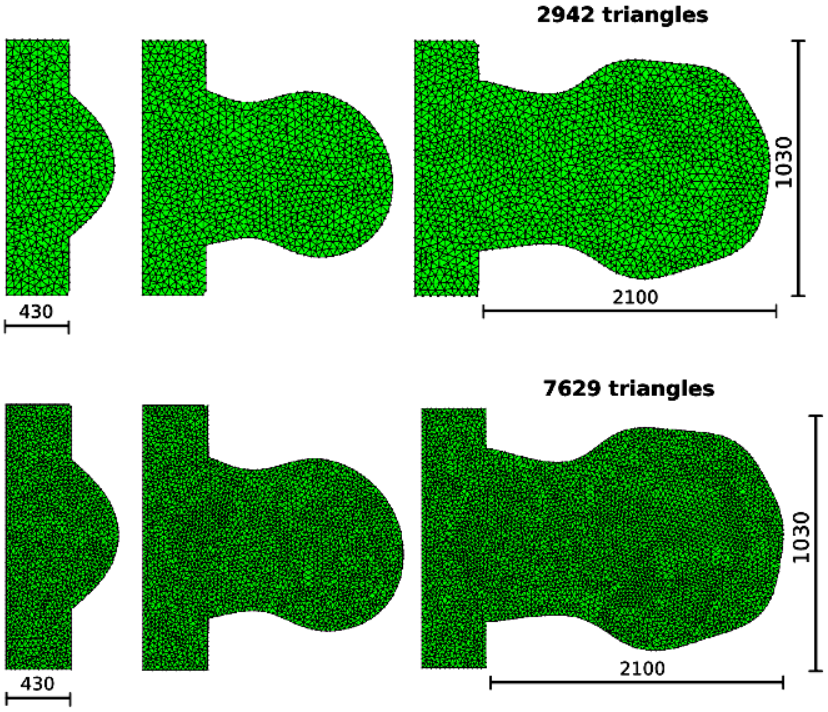

Figure 22: The two MorphoMovies used in the simulations. On top a MorphoMovie with coarse meshes and on the bottom the MorphoMovie with high resolution that is used in the simulations in Figure 3 and Figure 4 (main text. The PD length of the body and the AP/PD length of the limb bud shape at E12.5 are given. Just 3 time-points are shown in each case.

2.9 A realistic simulation of digit patterning

To test if the BSW model can recapitulate the dynamics of Sox9 (see Figure 1A main text) we developed a realistic numerical simulation of limb development. The starting point for our simulation is the finite element description of limb growth presented in [30]. In this model, triangular meshes are created from a series of experimental limb bud shapes with the Gmsh software [68]: a triangular mesh for each hour of development in the period from E10.5 to E12.5. Each mesh in the sequence is deformed into the next one with a velocity vector field derived from experimental clonal data, that recapitulates the tissue movements underlying the normal limb outgrowth. We call this continuous series of deforming meshes a MorphoMovie. We built two versions of the model: one with coarse meshes and one with high resolution meshes, shown in Figure 22. The value of the MorphoMovie is that each time we perform a limb development simulation, we do not have to re-simulate limb growth. Instead, we use the Morphomovies as a scaffold in which we solve the reaction-diffusion Partial Differential Equations (PDEs) of the BSW model.

The numerical simulations are performed with a PDE solver written in Java that is based on a second order Runge Kutta method (Heun method). The diffusion is simulated using a Finite Volume Solver that calculates the amount of diffusion between neighboring triangles according to the Fick's law of diffusion. The integration algorithm uses an adaptive time-step that is resized according to an error calculated as the difference between the numerical solutions obtained with the Heun method (2nd order) and the solution obtained with the Euler Method (1st order):

Let us define δt_n as the current time step and $\varepsilon_{ij} =\mid c_{ij}^2 - c_{ij}^1 \mid$ as the error in the triangle i for the reactant j, where c_{ij}^2 is the solution calculated with the Heun method and c_{ij}^1 the solution calculated with the Euler method. The next time-step δt_{n+1} is calculated as :

$$\delta t_{n+1} = \beta \delta t_n (\frac{\gamma}{\varepsilon_{max}})^{\frac{1}{\eta+1}}$$

where β is a correction term (set at 0.5), γ is a tolerance term (set at 0.02), ε_{max} is the maximum error $\forall i \forall j$ and η is the order of the method with highest precision, in our case 2 (Heun method). We begin each simulation with a very small initial time step $\delta t_0 = 0.000001$.

All the numerical simulations have zero-flux boundary conditions, have the homogeneous steady state as initial conditions and have a 1% of Gaussian multiplicative noise added to $sox9, bmp$ and wnt at each time step. One time unit in the simulation corresponds to one minute in real developmental time. On a 2.30GHz CPU of an Intel Core i7-3610QM with 4GB of ram, the wild-type simulation in Figure 3E (main text) takes approximately 30min on the the coarser meshes (average $\delta t \approx 0.026$) and 5h on the finer meshes (average $\delta t \approx 0.011$).

The simulations shown in Figure 3 and Figure 4 (main text) are performed with the high resolution MorphoMovie but equivalent results were obtained with the coarser model.

2.9.1 Figure 3A

As a first step, we wish to test the behavior of the BSW network inside the growing limb model. In particular, we want to explore how the tissue movements specified by the MorphoMovie can affect the stripy pattern formed by the BSW model. We simulate the BSW model (31) with the parameters shown in Table ST6 inside the MorphoMovie for 2880 time units (minutes) that represent $48h$ of development in the period from $E10.5$ to $E12.5$. The simulation, presented in Figure 3A (main text), shows a pattern with stripes that align along the PD axis of the limb. To test to which extent this alignment is due to the tissue movements specified in the MorphoMovie we introduce a new parameter β that scales the the speed of the reaction-diffusion system with respect to speed of the tissue movements. We rewrite the system (31) as:

$$\begin{aligned}
\frac{\partial sox9}{\partial t} &= \beta(\lambda(\alpha_{sox9} + k_2 bmp - k_3 wnt - (sox9 - sox9_0')^3)) \\
\frac{\partial bmp}{\partial t} &= \beta(\lambda(\alpha_{bmp} - k_4 sox9 - k_5 bmp) + \gamma d \nabla^2 bmp) \\
\frac{\partial wnt}{\partial t} &= \beta(\lambda(\alpha_{wnt} - k_7 sox9 - k_9 wnt) + \gamma \nabla^2 wnt)
\end{aligned}$$

By changing β we can test how the relative speed between the tissue movements and the reaction-diffusion patterning events affect the pattern. We perform three different simulations with the parameters in table ST6 and with $\beta = 0.25, \beta = 1$ and $\beta = 4$ respectively. The simulations reveal a general trend in which a faster reaction-diffusion mechanism leads to a pattern which is more independent of limb growth. Indeed, when $\beta = 0.25$ or $\beta = 1$ we observe that the direction of the stripes is biased to the distal tip of the limb, see Figure 23. This is due to the anisotropies that drive elongation in our growing model, see the top row in Figure 23. When $\beta = 4$, the fast reaction-diffusion rates allow the pattern to re-arrange quickly at every time-point and the distal bias given by the tissue movements is lost, see the patterns pointed by the white arrow in Figure 23.

The simulations presented in Figures 3 and 4 (main text) consider the intermediate case with $\beta = 1$ which leaves the parameters γ and d to the realistic values identified in Section 2.4.

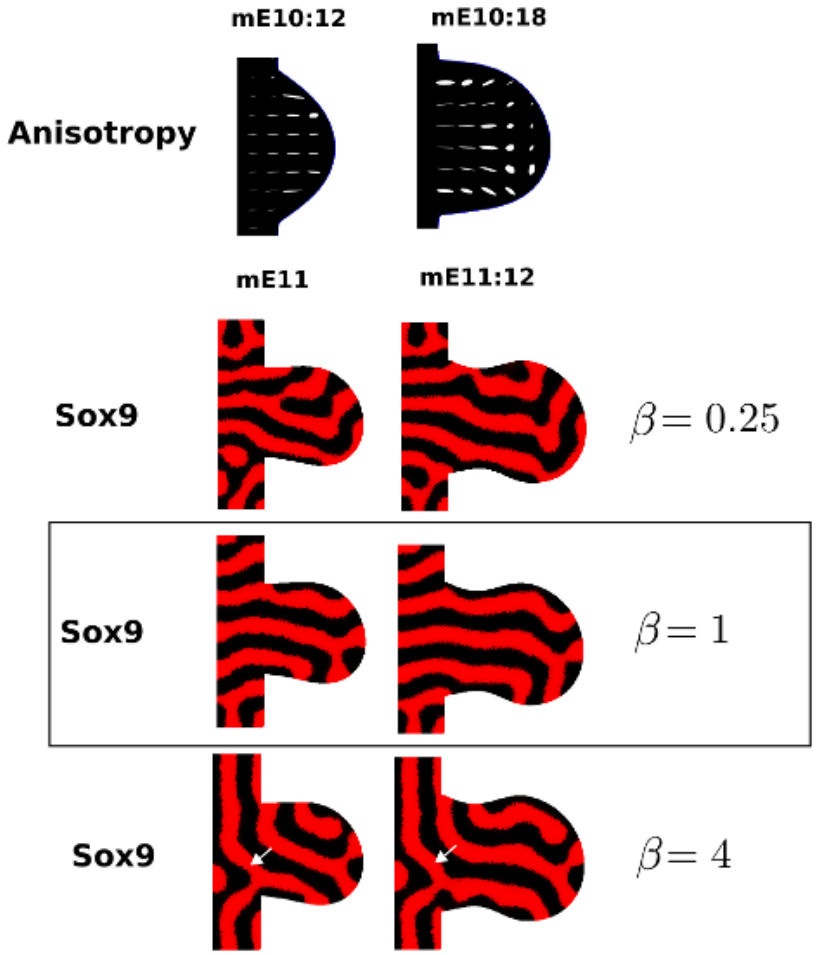

Figure 23: White ellipses show the anisotropies of the limb growth model (top row). The concentrations of Sox9 for the three simulations of the system (33) with $\beta = 0.25, \beta = 1$ and $\beta = 4$ are shown in red color. When β is high, the orientation of the stripes becomes more independent from the tissue movement, see the white arrow.

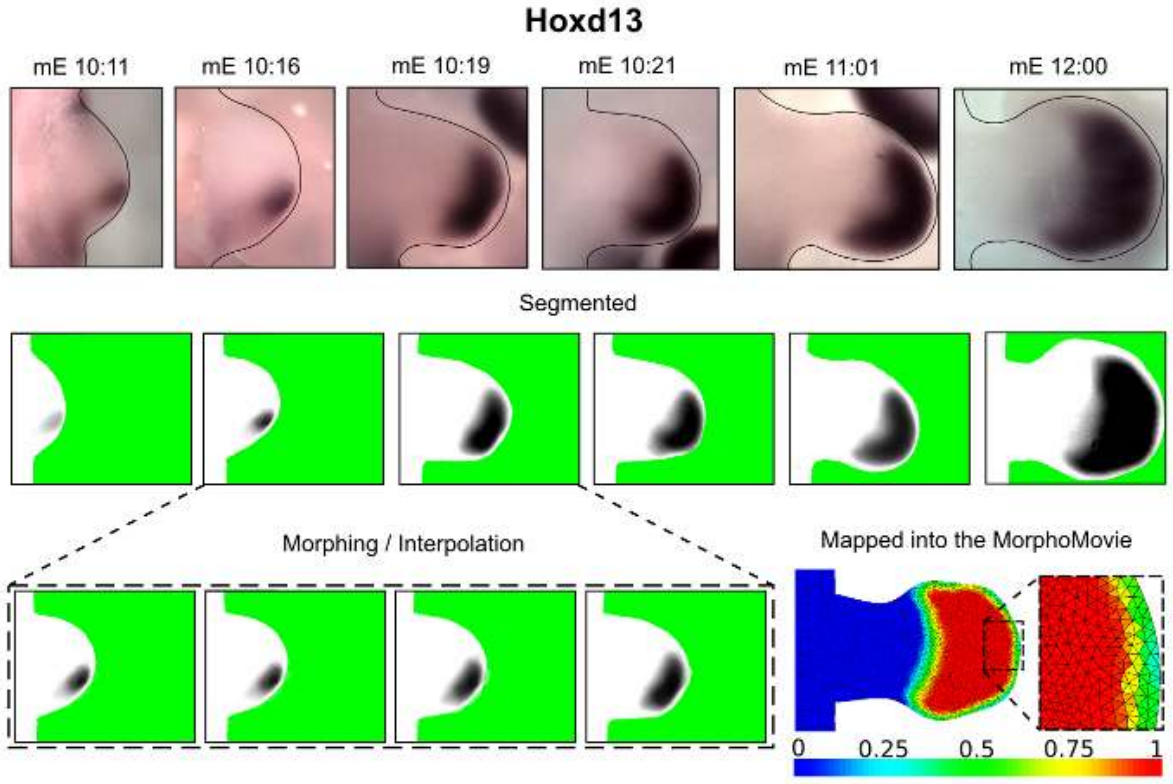

Figure 24: The first row shows a time course of Hoxd13 in-situ hybridization, the second row shows segmented expression patterns. In the third row, on the left an example of interpolated patterns obtained with JavaMorph and on the right an example of expression pattern mapped into the triangular mesh.

2.9.2 Figure 3B

Previous studies have revealed that Hoxa13 and Hoxd13 mark the perspective autopod and are required for normal digit patterning [69]. In addition, our previous work [9] has shown that distal Hox genes (including Hoxa13 and Hoxd13) regulate digit number by increasing the wavelength of the reaction-diffusion network that controls digit patterning. Taken together these results suggest that the patterning of the autopod is relatively independent from the patterning of the other proximal-distal segments. Our study focuses only on digit patterning, therefore we wish to investigate the behavior of the BSW model when it is restricted to the autopod by Hoxa13 and Hoxd13. We chose to map a detailed gene expression time-course of Hoxd13 into the MorphoMovie as a representative marker for both Hoxa13 and Hoxd13. This was done by manually segmenting in-situ hybridizations of Hoxd13 using the software Gimp [70] to remove the background and obtain a black and white images. We then interpolated the expression patterns with the JavaMorph software [71] to derive patterns for the missing time-points. We staged each time-point using the Morphometric staging system presented in [72]. Finally, we map the expression patterns into the corresponding triangular mesh of the MorphoMovie by using the Vtk library [73], each expression pattern is normalized between 0 and 1. An overview of the whole pipeline is shown in Figure 24. The final result is a smooth series of Hoxd13 experimental expression patterns mapped into the triangular mesh of the Morphomovies, see left part in Figure 3B (main text).

Scalar values associated with the expression of Hoxd13 can be used to vary the reaction-diffusion parameters of the BSW model to restrict the diffusion-driven instability to the autopod. This is done

by rewriting the the BSW model (31) as:

$$\frac{\partial sox9}{\partial t} = \lambda(\alpha_{sox9} + k_2 bmp - k_3 wnt - (sox9 - sox9'_0)^3)$$
$$\frac{\partial bmp}{\partial t} = \lambda(\alpha_{bmp} - (k_4 - k^1_{hox} hoxd13) sox9 - k_5 bmp) + \gamma d \nabla^2 bmp$$
$$\frac{\partial wnt}{\partial t} = \lambda(\alpha_{wnt} - (k_7 + k^2_{hox} hoxd13) sox9 - k_9 wnt) + \gamma \nabla^2 wnt$$

and by using the parameters shown in Table ST6 except for k_4 and k_7 which are set to $k_4 = 1.95$ and $k7 = 0.55$. These parameters are outside the Turing instability space (see the point A in Figure 25), therefore when $hoxd13 = 0$ the BSW model does not form any pattern. However, when $hoxd13 > 0$ the new parameters $k^1_{hox} = 0.36$ and $k^2_{hox} = 0.72$ promote a shifting of k_4 and k_7 to the values in Table ST6 which lie inside the Turing instability region (see the point B in Figure 25). This shifting allows the system to define an active autopod region according to the experimental expression patterns of Hoxd13.

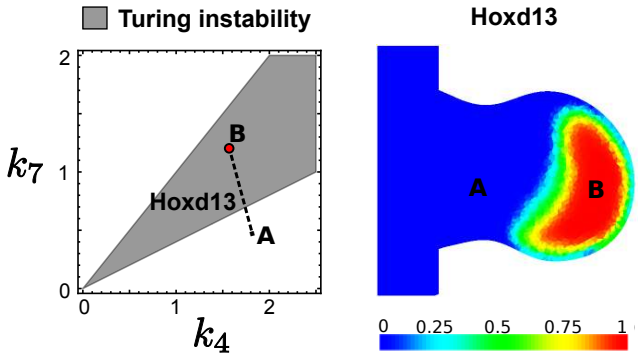

Figure 25: On the left, a graph shows the Turing instability region (gray color) as k_4 and k_7 are varied. The black dashed line represents the change in k_4 and k_7 promoted by Hoxd13 to go from a region with no Turing instability (A) to a region with Turing instability (B). On the right, an Hoxd13 expression mapped into the model shows where the system move from (A) to (B).

The simulation presented in Figure 3B (main text) show a series of distally oriented stripes that progressively appear as Hoxd13 expands. Remarkably, despite the intrinsic variability of reaction-diffusion patterning, when we run the same simulation multiple times we observe the same stereotypical sequence of stripes, see Figure 26.

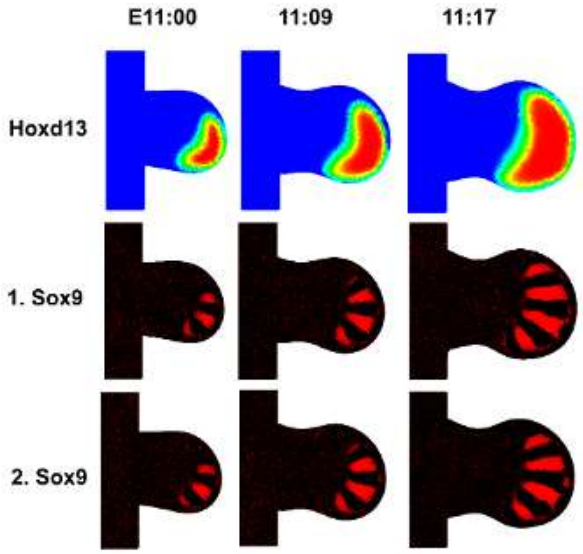

Figure 26: Top row, the experimental pattern of Hoxd13 mapped inside the MorphoMovie. The second and the third row show the Sox9 pattern in two independent simulation runs. The progressive expansion of the Hoxd13 domain reduces the intrinsic variability of the reaction-diffusion patterning and generates a stereotypical sequence of stripes.

This result confirms previous studies on one-dimensional domains [28] which showed that a progressive expansion of the spatial domain was able to reduce the intrinsic variability of the patterns formed by reaction-diffusion systems. However, the BSW model modulated by Hoxd13 produces stripes that have a different orientation with respect to the experimental Sox9 pattern. This can be observed by comparing the simulations on the right part of Figure 3B with Figure 3E (main text). In addition, in late time-points the simulation produces distal stripes bifurcation, see black arrows in Figure 3B (main text). This results confirms our previous work [9] which highlighted that when a reaction-diffusion system was simulated inside a curved static domain that represented the expression of Hoxd13 and Hoxa13, stripe bifurcation arose because of the bigger AP length at the distal tip of the limb. This work also suggested that such bifurcations could be avoided by coupling Hox genes with a graded Fgf signaling gradient to scale the wavelength in proximal-distal graded manner. In the next section we introduce an Fgf signaling gradient to explore a similar mechanism inside the growing simulation.

2.9.3 Figure 3C

We previously proposed [9] that a gradient coming from the AER in conjunction with distal Hox genes (E.g. Hoxd13) modulates the Turing model to align the digits and prevent distal bifurcations. However, in our previous study the simulations were performed on a static domain. To extend this idea to the growing simulation, we simulate a gradient that represents the region where Fgf signaling is active in the MorphoMovie. To do so, we define regions that correspond to Fgf8 and Fgf4-9-17 expression on the boundary of each mesh. In the case of Fgf4-9-17 we use Fgf4 in-situ hybridization as representative patterns, see the red line in Figure 27.

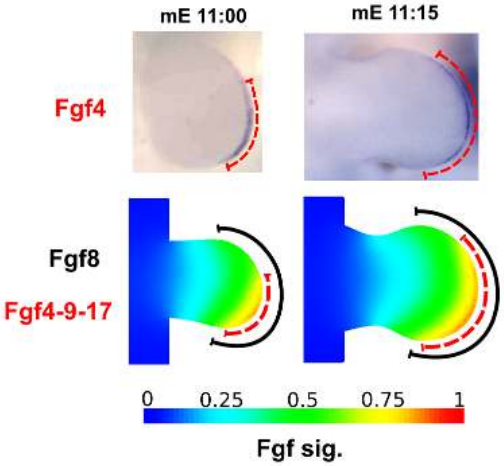

Figure 27: On the top row in-situ hybridizations for Fgf4. The dashed red line highlights the region along the AER where Fgf4 is expressed. On the bottom row, the black line shows the region under the AER where $\alpha_{fgf8} > 0$, while the dashed red line shows the region where $\alpha_{fgf4} > 0$. The colored pattern represent the simulated Fgf signaling gradient obtained by diffusion of a single fgf term that is influenced by both production terms.

These boundary regions are used to simulate a gradient of Fgf signaling, see Figure 27. The gradient is formed by local production, diffusion and decay according to the following equations:

$$\frac{\partial fgfsig}{\partial t} = \alpha_{fgf8} + \alpha_{fgf4} - \mu_{fgf} fgfsig + D_{fgf} \nabla^2 fgfsig$$

where $\mu_{fgf} = 0.1$, $D_{fgf} = 30000$, the two production terms $\alpha_{fgf8}, \alpha_{fgf4}$ are set to $\alpha_{fgf4} = 0.7$ and $\alpha_{fgf4} = 0.3$ in the triangles underneath the $Fgf8$ and $Fgf4$ expressing boundary and are equal to 0 elsewhere. Finally we normalize the gradient between 0 and 1 according to the last time point where $Fgf4$ has fully expanded promoting the maximum $fgfsig$ values. The results are showed in Figure 27.

Our goal is to verify whether by modulating the parameters k_4 and k_7 of the BSW model in a proximal-distal graded manner with $fgfsig$, we can promote the correct stripe alignment (radial) and also increase the wavelength to prevent distal stripe bifurcations. Similarly to the case of Hoxd13 we rewrite the BSW model (31) as:

$$\begin{aligned}
\frac{\partial sox9}{\partial t} &= \lambda(\alpha_{sox9} + k_2 bmp - k_3 wnt - (sox9 - sox9'_0)^3) \\
\frac{\partial bmp}{\partial t} &= \lambda(\alpha_{bmp} - (k_4 - k^1_{fgf} fgfsig) sox9 - k_5 bmp) + \gamma d \nabla^2 bmp \\
\frac{\partial wnt}{\partial t} &= \lambda(\alpha_{wnt} - (k_7 + k^2_{fgf} fgfsig) sox9 - k_9 wnt) + \gamma \nabla^2 wnt
\end{aligned}$$

and we use the parameters shown in Table ST6 except for k_4 and k_7 which are set to $k_4 = 1.95$ and $k7 = 0.55$ that are outside the Turing instability space (see the point A in Figure 28). In the distal part of the limb $fgfsig$ progressively increases towards the AER (where Fgf ligands are secreted) this together with the new parameters $k^1_{fgf} = 0.36$ and $k^2_{fgf} = 0.72$ promotes a proximal-distal graded shifting of k_4 and k_7 towards the values in Table ST6 that are inside the Turing instability region (see the point B in Figure 28).

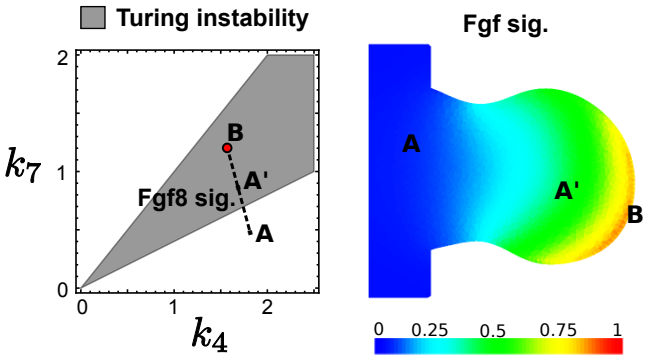

Figure 28: On the left, a graph shows the Turing instability region (gray color) as k_4 and k_7 are varied. The black dashed line represents the change in k_4 and k_7 promoted by $fgfsig$ to go from no-Turing instability (A) to a Turing instability (B), an intermediate point (A') is showed. On the right, an example of simulated $fgfsig$, the points (A) (A') (B) are highlighted along the gradient.

In agreement with the static simulations presented in Figure 20, the simulation on the growing model shows that when k_4 and k_7 are respectively decreased and increased in a graded manner, the stripes align towards the gradient. When simulated inside the limb geometry, this promotes radial conformation of the stripes, see the right part in Figure 3C (main text). However, we also observe a greater variability in the arrangement of the stripes in comparison with the case where Hoxd13 expression defined the active region, see Figure 29.

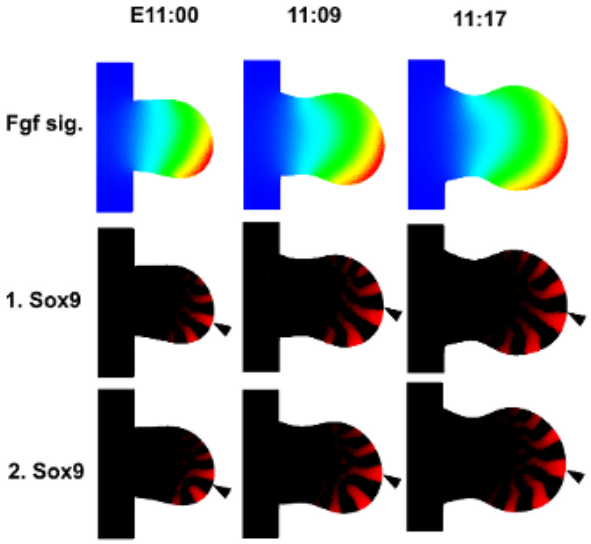

Figure 29: Top row, the simulated gradient of Fgf signaling. The second and third rows show the Sox9 pattern in two independent simulation runs. The position of the stripes formed by the BSW model is highly variable between runs, see the black arrow which is pointing at the same position in both simulations.

On the one hand, the progressive expansion of Hoxd13 into the anterior and the proximal part of the limb promotes a sequence of reaction-diffusion patterns that reduces the variability of possible final configurations. On the other hand, the model with modulation by Fgf signaling promotes a reliable radial orientation of the stripes and prevents distal stripe bifurcations by scaling the wavelength along the PD axis. This suggests that a model using both Hoxd13 and the Fgf signaling gradient to modulate the parameters of the BSW model may be able to fit the experimental Sox9 pattern. This is explored in detail in the next section.

2.9.4 Figure 3D-F

To investigate the combined effect of Hoxd13 and Fgf signaling we rewrite the the BSW model (31) as:

$$\begin{aligned}
\frac{\partial sox9}{\partial t} &= \lambda(\alpha_{sox9} + k_2 bmp - k_3 wnt - (sox9 - sox9'_0)^3) \\
\frac{\partial bmp}{\partial t} &= \lambda(\alpha_{bmp} - (k_4 - k^1_{hoxfgf} hoxd13 \cdot fgfsig) sox9 - k_5 bmp) + \gamma d \nabla^2 bmp \\
\frac{\partial wnt}{\partial t} &= \lambda(\alpha_{wnt} - (k_7 + k^2_{hoxfgf} hoxd13 \cdot fgfsig) sox9 - k_9 wnt) + \gamma \nabla^2 wnt
\end{aligned} \tag{33}$$

and we use the parameters shown in Table ST6 except for k_4 and k_7 which are set to $k_4 = 1.95$ and $k7 = 0.55$ which is outside the Turing space (no pattern). Similar to the previous cases, the new parameters $k^1_{hoxfgf} = 0.36$ and $k^2_{hoxfgf} = 0.72$ allow $hoxd13$ and $fgfsig$ to modulate k_4 and k_7 moving the system inside the Turing space, see the graph in Figure 3D (main text). The entire list of parameters used in the simulation is given in Table ST7.

k_2	k_3	k_4	k_5	k_7	k_9	k^1_{hoxfgf}	k^2_{hoxfgf}	γ	d	λ
1	1	1.95	0.1	0.55	0.1	0.36	0.72	250	2.5	0.6

Table ST7: Parameter set for the limb development simulation

The production terms $\alpha_{sox9}, \alpha_{bmp}$ and α_{wnt} were calculated as shown in section 2.6 to obtain the homogeneous steady state $(sox9'_0, bmp'_0, wnt'_0) = (10, 10, 10)$.

As hoped, the BSW model modulated by both Hoxd13 and the Fgf signaling forms a stereotypical sequence of stripes that align radially towards the AER and increase in wavelength along the proximal-distal axis reflecting the experimental Sox9 patterns. Nevertheless, in later time points the simulations show that the stripe start to bend and bifurcate (see Figure S8A). By analyzing the model in detail, we find that this is due to the dynamics of Fgf signaling levels relative to Hoxd13 expression, see Figure S8A.

Our analysis reveals that up to stage E12 the proximal boundary of Hoxd13 nicely correlates with a specific threshold of Fgf signaling, despite the dynamics of tissue growth, see the Figure S8A. This behavior is not imposed into the simulation but spontaneously results from the experimental expression patterns of Hoxd13 and the experimental expression of Fgf4 and Fgf8 (see Section 2.9.3) that we used to simulate the Fgf signaling gradient. The progressive extension of Fgf4 along the anterior-posterior axis of the limb increases the Fgf signaling over time and expands its range towards the proximal part of the limb in coordination with the proximal expansion of Hoxd13. In agreement with our model, it has been shown that Fgfs are involved in PD patterning [34] and that they promote the expression of distal markers like Hoxd13. The coordination between Hoxd13 and Fgf signaling that we observe from the experimental data, may therefore be simply due to the fact that Hoxd13 is promoted by the Fgf signaling, suggesting that the proximal expansion of Hoxd13 (which we also reported in a previous study [30]) should be accompanied by an increase in the Fgf signaling range. However, when the expression of Hoxd13 expands proximally, Fgf4 has already extended anteriorly and the Fgf signaling range remains unchanged, see the graph on the right in Figure S8A. In summary, our analysis suggests that to obtain the correct patterning throughout the entire MorphoMovie Fgf signaling should be gradually up-regulated

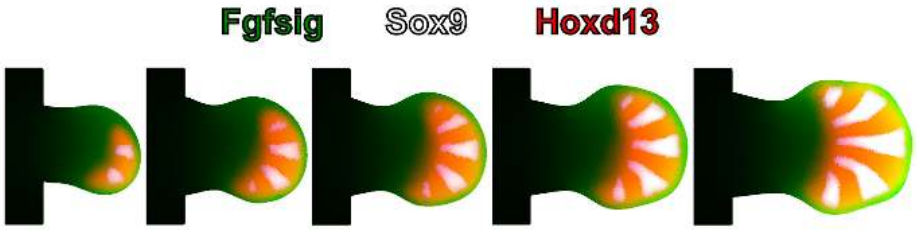

Figure 30: A time-course of the final simulation presented in Figure 3E (main text), the simulated Fgf signaling gradient is shown in green, the experimental expression patterns of Hoxd13 in red and the simulated Sox9 pattern in white.

during limb growth to match the anterior and proximal expansion of Hoxd13. This prediction agrees with previous studies that have proposed that the expression of Fgfs in the AER is progressively up-regulated by the the Shh-Grem-Fgf positive feedback loop [3].

To validate this prediction we re-simulate the Fgf.signaling gradient by progressively increasing the production of $fgf8$ and $fgf4$ over time. This is done by rewriting the terms α_{fgf8} and α_{fgf4} as follows:

$$\alpha_{fgf8} = 0.7 + \Delta_{fgf8}\frac{t - t_1}{t_2 - t_1}$$
$$\alpha_{fgf4} = 0.3 + \Delta_{fgf4}\frac{t - t_1}{t_2 - t_1}$$

where t is the the current time in the simulation, t_1, t_2 define the temporal interval when the productions are increased and $\Delta_{fgf8}, \Delta_{fgf4}$ define the strength in Fgf increase. In the final simulation showed in Figure 3E, we use the system (33) and we consider an Fgf signaling gradient simulated with $\Delta_{fgf8} = \Delta_{fgf4} = 0.15$, $t_1 = 17200$ (E12) and $t_2 = 18000$ (E12.5). In conclusion, the coordination between Fgf signaling and Hoxd13 prevents stripe bending and stripe bifurcation, see Figure S8B and produces a pattern that strongly resemble the expression pattern of Sox9, see Figure 3E-F (main text) and Figure 30.

2.9.5 Reduction of Hox dosage

In a previous study [9] we showed that a reduction of distal Hox dosage produces limbs with an increased number of thinner digits. The effect of distal Hox genes removal was more evident when the growth deficiencies that were caused by the lack of Hox dosage were rescued by using a Gli3-/- mutant background, where the growth of the hand-plate is increased. To check if the BSW model (33) can recapitulate the effect of Hox dosage reduction, we compare the Gli3+/- Hoxa13+/- Hoxd11-13-/- mutant, which has an hand-plate size comparable to the wild type, with a simulation of the system (33) where Hox dosage is reduced by rewriting $hoxd13$ as $\frac{hoxd13}{2}$. In agreement with the phenotype of the Gli3+/- Hoxa13+/- Hoxd11-13-/- mutant and with our previous simulations, this model forms an increased number of thinner digits that have an higher probability to bifurcate distally, see Figure 31. Finally, in agreement with our previous results [9], we also observed that digit patterning becomes slower.

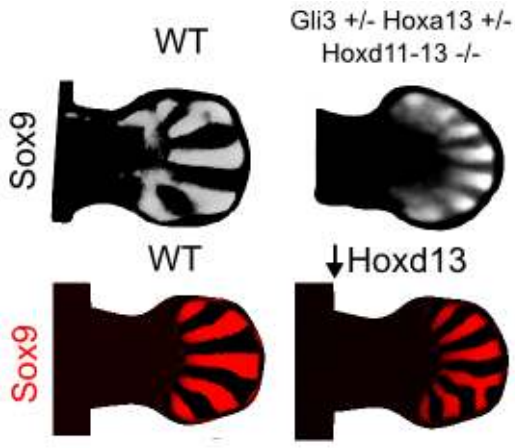

Figure 31: On the left, the WT Sox9 pattern (gray) and a simulated Sox9 pattern (red) at E12. On the right, when Hox dosage is reduced (E.g. the two alleles of Hoxd11-13 and one allele of Hoxa13) the Sox9 pattern at E12.5 (gray) shows an increased number of thinner digits (one allele of Gli3 is removed to compensate for growth reduction). Similarly, when the contribution of Hox is reduce to a half in the model, the simulated Sox9 pattern (red) shows an increased number of thinner digits.

2.9.6 Fgf signaling increases the wavelength

Since the BSW model relies on the idea that Fgf signaling has a positive effect on digit wavelength, we wished to test this experimentally by Fgf signaling gain of function. Unfortunately, Fgf signaling is also well known for promoting limb growth, therefore the application of ectopic Fgf to the limb bud would have pleiotropic effects making the comparison between experimental perturbations and the wild type patterning difficult. To avoid this problem, we decided to study the effect of ectopic Fgf signaling in micromass cultures where the effect of Fgf on growth can be neglected, see Figure 32.

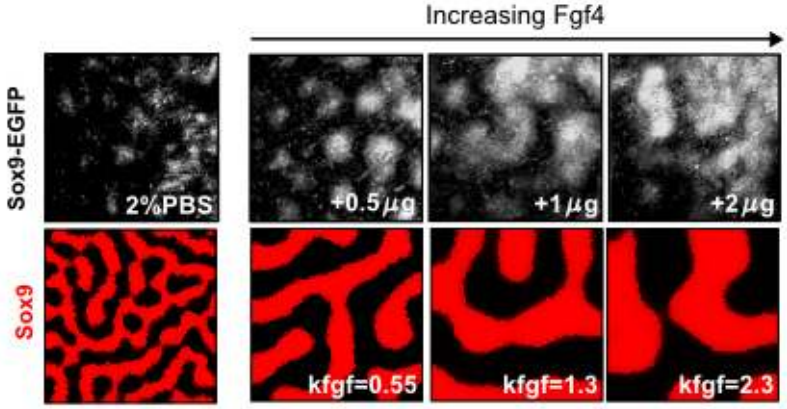

Figure 32: Top row, Sox-EGFP at 24h in micromass cultures with increasing concentration of Fgf4 added to the medium. As the concentration of Fgf4 increases, the wavelength of the periodic pattern becomes larger. Bottom, a similar behavior is observed in 2D simulations of the BSW model with increasing Fgf signaling.

We compared these experiments with simulations of a BSW system (33) which is rewritten to modulate in a homogeneous manner the parameters k_4 and k_7 with Fgf inside a squared domain:

$$\frac{\partial sox9}{\partial t} = \lambda(\alpha_{sox9} + k_2 bmp - k_3 wnt - (sox9 - sox9'_0)^3)$$
$$\frac{\partial bmp}{\partial t} = \lambda(\alpha_{bmp} - (k_4 - k_{fgf}0.11)sox9 - k_5 bmp) + \gamma d\nabla^2 bmp$$
$$\frac{\partial wnt}{\partial t} = \lambda(\alpha_{wnt} - (k_7 + k_{fgf}0.47)sox9 - k_9 wnt) + \gamma\nabla^2 wnt$$

We use the parameter set in Table ST6 except for k_4 and k_7 which are set to $k_4 = 1.7$ and $k_7 = 0.8$. By varying the rate k_{fgf} we can obtain parameters that lay along the trajectory promoted by the Fgf signaling gradient in the wild type simulation presented in Section 2.9.4, see Figure 33.

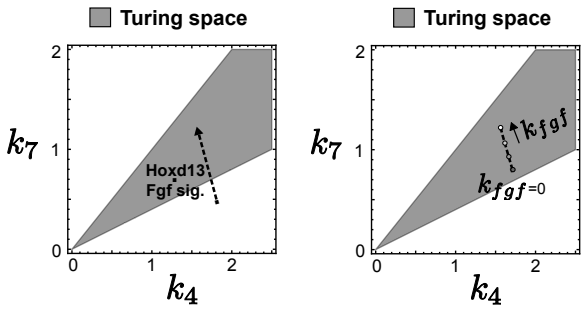

Figure 33: On the left, the change in k_4 and k_7 promoted by Fgf signaling and Hoxd13 in the system (33). On the right, the micromass simulations have default parameters ($k_{fgf} = 0$) inside the Turing instability region. When k_{fgf} is increased the parameter set is moved along the same direction as in the (33). The parameter set of the simulation with different k_{fgf} can be visualized as single points along the dashed line.

We simulate the addition of increasing concentration of ectopic Fgf4 with the following k_{fgf} values: 0, 0.33, 0.66 and 1, see the simulation in Figure S3B.

2.10 Genetic perturbations in mouse

mutant	phenotype	reference
$Bmp2^{c/c}; Bmp4^{c/c}; Prx1-Cre$	Absence of the two posterior digits; affected proximal elements, stylopod fused with zeugopod	Bandyopadhyay et al 2006 [24]
$Bmp2^{c/c}; Bmp7^{c/c}; Prx1-Cre$	Shortened phalanges in the middle digits	Bandyopadhyay et al 2006 [24]
$Bmpr1a^{flox/-}; Prx1-Cre$	Absence of digital elements in the autopod. Sox9 disorganized pattern	Ovchinnikov et al 2006 [74] Selever et al 2004 [75]
$Bmpr1b^{-/-}$	Null mutants present normal early patterning events / normal Sox9 expression	Yi et al 2001 [76]
$Smad4^{flox/flox}; Prx1-Cre$	Loss of Sox9 expression in the autopod - no digits formed	Benazet et al 2012 [27]

Table ST8: Bmp signaling mutants

mutant	phenotype	reference
$Sox9^{flox/flox}; Prx1-Cre$	Complete absence of cartilage and bone in limbs. Normal digital pattern markers show no periodic pattern (Bmp2, Chrd, Noggin).	Akiyama et al 2002 [19]
$Sox9Tg-Prx1\ promoter$	Polydactyly	Akiyama et al. 2007 [77]

Table ST9: Sox9 mutants

mutant	phenotype	reference
$Porcn^{lox/Y}; Prx1-Cre$	Shorter and wider digits and fusion of digits, loss of digits.	Barrott et al 2011 [78]
$Wnt5a^{-/-}$	Shorter and wider digits, and loss of digits	Yamaguchi et al 1999 [79]
$Wnt3a^{n/c}; Msx2-Cre$	Loss of autopod	Barrow et al 2003 [80]
$Wnt3a^{n/c}; RAR-Cre$	Loss of digits	Barrow et al 2003 [80]
$Wnt7a^{-/-}$	Ventralization of the whole limb and loss of posterior digits	Parr and McMahon et al 1995 [81]
$Wls^{c/c}; Msx2-Cre$	Shortened digits-truncated autopod	Zhu et al 2012 [82]
$Wls^{c/c}; Prx1-Cre$	Absence of autopod-arrest of distal differentiation	Zhu et al 2012 [82]
$\beta cat^{flox/-}; Prx1-Cre/+$	Up-regulation of Sox9 in the distal half of the limb	Hill et al 2005 [22]
$\beta cat^{ex3fl/+}; Prx1Cre/+$ "stabilized β-cat"	Down-regulation of Sox9 in the limb (opposite effect from reducing β-catenin)	Hill et al 2005 [22] Hill et al 2006 [23]

Table ST10: Wnt signaling mutants

2.11 Model predictions vs experimental perturbations

To validate the BSW model, we performed experimental perturbations in limb culture with E11.5 Sox9-EGFP limbs and compared the resulting Sox9 patterns with similar perturbations in the model presented in Section 2.9.4.

2.11.1 Control simulation

The control for the experimental perturbations is the limb culture shown in Figure 4B (main text) with the vehicle DMSO added to the medium. In this condition, cultured limbs are able to growth and elongate for approximately 48h, see Figure S5. The control for the simulations, is the wild type simulation shown in Figure 4A (main text) obtained with the BSW model (33) with the parameters presented in Table ST7 starting from the stage E11.5.

2.11.2 Inhibition of Bmp signaling

When the Bmp-signaling inhibitor LDN193189 is added to the medium of limb cultures, we observe down regulation of Sox9 in the autopod and loss of digits within 48h of culture, see Figure 4B (main text). In the BSW model, the strength of Bmp signaling is controlled by the parameter k_2. To simulate the addition of LDN, we rewrite the BSW system (33) as follows:

$$\begin{aligned}
\frac{\partial sox9}{\partial t} &= \lambda(\alpha_{sox9} + (k_2 - LDN)bmp - k_3 wnt - (sox9 - sox9'_0)^3) \\
\frac{\partial bmp}{\partial t} &= \lambda(\alpha_{bmp} - (k_4 - k^1_{hoxfgf} fgfsig)sox9 - k_5 bmp) + \gamma d\nabla^2 bmp \\
\frac{\partial wnt}{\partial t} &= \lambda(\alpha_{wnt} - (k_7 + k^2_{hoxfgf} fgfsig)sox9 - k_9 wnt) + \gamma\nabla^2 wnt
\end{aligned}$$

where LDN is a new parameter that controls the amount of LDN added to the model. We simulate this system using the parameters in Table ST7 and start the simulation from the timepoint which corresponds to the stage E11.5, shown in first column Figure 4A (main text). We performed different simulations progressively increasing the value of LDN. Our analysis reveals that when $LDN = 0.33$, Sox9 down-regulates and the digit pattern disappears, see the second row in Figure 4A (main text). Interestingly, the model predicts that Bmp is increased in the region where Sox9 is down-regulated, see the second row in Figure 4D (main text). In agreement with this prediction, Bmp2 in situ hybridizations in limb cultures treated with LDN show a distal up-regulation of Bmp2 expression. Furthermore, the predictions of the model are also confirmed by the analysis of the Smad4 mutant presented in [27], where impairment of Bmp signaling results in down-regulation of Sox9 and up-regulation Bmp2, see Figure 34.

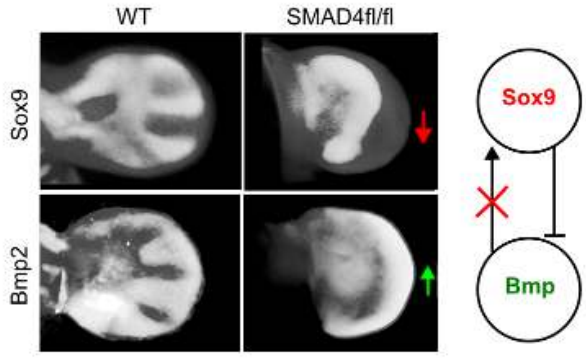

Figure 34: OPT scans of Sox9 and Bmp2 expression patterns in WT (left) and in the Prx1-CRE-Smad4fl/fl mutant (right). In the Smad4fl/fl mutant abrogation of canonical Bmp signaling causes loss of digit patterning with down-regulation of Sox9 (red arrow) and up-regulation of Bmp2 (green arrow). This behavior is consistent with deletion of Bmp signaling (red cross) in a Substrate-depletion network where Bmp activates Sox9 that in turns represses Bmp, network diagram on the right.

2.11.3 Inhibition of Wnt signaling

To investigate the dynamics of digit patterning when Wnt signaling is inhibited, we add the Wnt inhibitor IWP2 to the medium of limb cultures. This inhibitor blocks Wnt signaling by preventing the secretion of Wnt ligands and has been used with success to suppress the Wnt/beta-catenin pathway in cancer cells [83]. When IWP2 is added to limb cultures, we observe an up-regulation of Sox9 and a progressive increase in the width of the digit which eventually results in digit fusion, see the third row in Figure 4B (main text). To simulate the addition of IWP2 we rewrite the BSW system (33) as follows:

$$\begin{aligned}
\frac{\partial sox9}{\partial t} &= \lambda(\alpha_{sox9} + k_2 bmp - k_3 wnt - (sox9 - sox9_0')^3) \\
\frac{\partial bmp}{\partial t} &= \lambda(\alpha_{bmp} - (k_4 - k_{fgf}^1 fgfsig)sox9 - k_5 bmp) + \gamma d\nabla^2 bmp \\
\frac{\partial wnt}{\partial t} &= \lambda((\alpha_{wnt} - IWP2) - (k_7 + k_{fgf}^2 fgfsig)sox9 - k_9 wnt) + \gamma\nabla^2 wnt
\end{aligned}$$

where $IWP2$ is a new parameter that reduces the amount of secreted Wnts as done by IWP2. Similar to the case of LDN, we simulate this system using the parameters in Table ST7 and start the simulation from the stage E11.5 showed in the left-most column of Figure 4A (main text). We perform different simulations by progressively increasing $IWP2$. Strikingly, the simulations reveal that when $IWP2$ is increased the model predicts a change in the Sox9 pattern that is almost identical to patterning dynamics observed in limb cultures, see third row in Figure 4B (main text). When $IWP2 = 0.4$ each digit increases in width until digit fusion is obtained. Moreover, the model predicts that Bmp is down regulated in the distal part of the limb, see the last row in Figure 4D (main text). In agreement with this prediction, in situ hybridizations in limbs treated with IWP2 show a distal down-regulation of Bmp2 expression, see the third row in Figure 4D.

2.11.4 Simultaneous inhibition of Bmp and Wnt signaling

Since Bmp signaling inhibition causes digit loss while inhibition of Wnt signaling causes loss of interdigits, we decided to explore weather a simulation that adds both IWP2 and LDN would balance-out the

perturbations and give a more interesting pattern. We rewrite the system (33) combining the effect of both drugs as follows:

$$\frac{\partial sox9}{\partial t} = \lambda(\alpha_{sox9} + (k_2 - LDN)bmp - k_3 wnt - (sox9 - sox9'_0)^3)$$
$$\frac{\partial bmp}{\partial t} = \lambda(\alpha_{bmp} - (k_4 - k^1_{fgf} fgfsig)sox9 - k_5 bmp) + \gamma d\nabla^2 bmp$$
$$\frac{\partial wnt}{\partial t} = \lambda((\alpha_{wnt} - IWP2) - (k_7 + k^2_{fgf} fgfsig)sox9 - k_9 wnt) + \gamma\nabla^2 wnt$$

We simulate this system with the parameters in Table ST7 setting $LDN = 0.33$ and $IWP2 = 0.4$. Interestingly, our model predicts that starting from the timepoint corresponding to E11.5 the BSW model forms a pattern with two/three thick digits that occupy the entire autopod, see the Figure 35 and simulation in Figure 4E-High (main text).

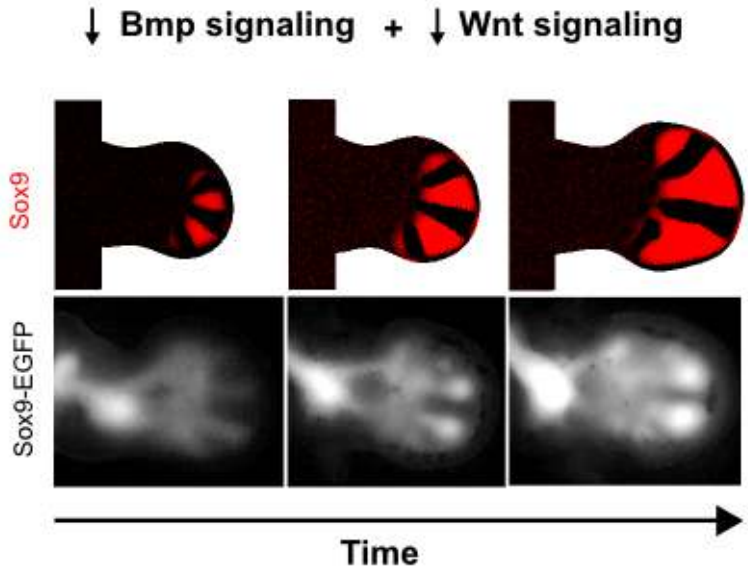

Figure 35: Top row, simulated Sox9 patterns (red) when Bmp and Wnt signaling are inhibited simultaneously ($LDN = 0.33$ and $IWP2 = 0.4$): the periodic digit pattern re-arrange to form few thicker digits. Bottom row, a similar change in the the Sox9-EGFP pattern is observed when LDN and IWP2 are added at E11.5 in limb culture.

To test weather this oligodactyly pattern is dependent on the concentration of LDN and $IWP2$, we perform a similar simulation in which both parameters were reduced: $LDN = 0.2$ and $IWP2 = 0.25$, Figure 4E-Medium (main text). The simulations show a less severe oligodactyly with three/four smaller digits that occupy the entire autodpod, suggesting that the thickness of the digits (digit period) and the severity of the oligodactyly are positively correlated with the amount of LDN and $IWP2$, Figure 4E (main text).

Intuitively, the olygodactyly can be seen as the results of the slower Sox9 reaction kinetics caused by Bmp and Wnt inhibition. If we approximate the effect of IWP2 as a general reduction in the amount of wnt, we can rewrite $\frac{\partial sox9}{\partial t}$ as:

$\frac{\partial sox9}{\partial t} = \lambda(\alpha_{sox9} + (k_2 - LDN)bmp - k_3(wnt - IWP2) - (sox9 - sox9'_0)^3)$

assuming that the amount of LDN and IWP2 are coupled, we can approximate the effect of LDN=IWP2 with a single parameter α and rewrite the systems as:

$\frac{\partial sox9}{\partial t} = \lambda(\alpha_{sox9} + \alpha(k_2 bmp - k_3 wnt) - (sox9 - sox9'_0)^3)$

where $0 < \alpha < 1$ is inversely proportional to the amount of LDN and IWP2 added to the medium and $\alpha = 1$ represents the case LDN=IWP2=0. Finally, we can calculate how the wavelength changes when α is decreased by calculating the wavenumber k_{max} (as explained in section 2.3) and by deriving the wavelength ω of the 1D case: $\omega = \frac{2\pi}{k_{max}}$. In agreement with the numerical simulations presented in Figure 4E (main text), as the concentrations of LDN and IWP2 increase (smaller α) the wavelength ω becomes larger, see Figure 36.

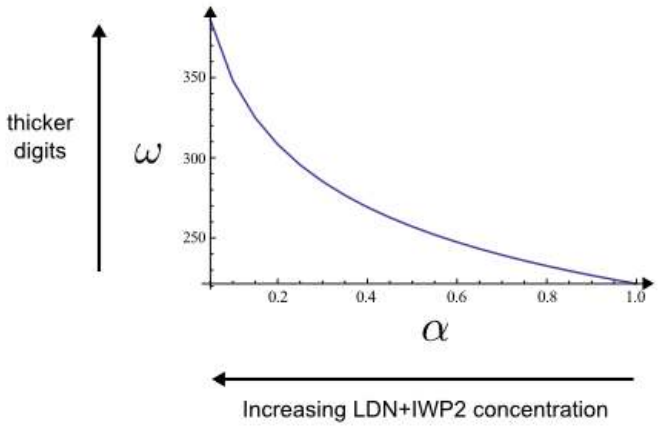

Figure 36: A graph showing how the wavelength (ω) changes when Bmp and Wnt signaling are simultaneously inhibited with LDN and IWP2. When LDN and IWP2 concentrations increase (smaller α) the wavelength increases.

To test these predictions, we perform experiments by adding IWP2 and LDN simultaneously at E11.5. We use LDN and IWP2 concentrations that would individually cause digit loss and interdigit loss, respectively. This allows us to test the prediction that the two drugs would balance out and promote a pattern with fewer, but thicker digits (a larger effective wavelength). In agreement, with the prediction of the model the experiments show an oligodactyly Sox9 pattern with two ticker digits, see Figure 4E in the main text. We perform different experiments by using low, medium and high drug concentrations to asses weather as predicted by model the drug concentrations positively correlates with the oligodactyly severity and with the digit period, see the graph and experiments in Figure S7 and in Figure 4E (main text).

2.11.5 Gain of function experiments: Wnt and Bmp ligands

Finally, we use the BSW model to predict the effect of Bmp and Wnt gain of functions. This was done by defining two virtual beads that were used to locally increase the concentrations of Bmp and Wnt respectively. The virtual beads are defined by taking advantage of limb Morphomovie which provides a map between the triangles of the different meshes from E10.5 to E12.5. This map can be used to mark triangles corresponding to a bead at E11.5 and to track their fate until E12.5.

First, we define a virtual bead by marking triangles at E11.5 in the interdigital region between digit 2 and digit 3, see the white triangles in Figure S6A. We track these triangles until E12.5 and model a Bmp bead by modifying the BSW system to constantly produce Bmp in the marked triangles. This is done by changing the BSW equations (33) inside marked triangles as:

$$\begin{aligned}\frac{\partial sox9}{\partial t} &= 0\\ \frac{\partial bmp}{\partial t} &= \alpha_{bmp}^2 + \gamma d \nabla^2 bmp\\ \frac{\partial wnt}{\partial t} &= 0\end{aligned}$$

These equations model the Bmp bead as a region that constantly produces bmp with the rate α_{bmp}^2. We ignore degradation terms within the marked triangles by assuming that α_{bmp}^2 represents flow of bmp at steady state and that the large amount of Bmp in the bead makes the decay negligible. A simulation with the parameters in Table ST7 and $\alpha_{bmp}^2 = 1$ predicts an up-regulation of Sox9 and a down regulation of Bmp in the region surrounding the bead, see the bottom row in Figure S6A. In agreement with this prediction implantation of beads soaked with Bmp2 in the interdigital region show a similar behavior, see the top row in Figure S6A.

Secondly, we define another virtual bead by marking triangles in the digit 2 region at E11.5, see the white triangles in Figure S6B. Similar to the case of Bmp, we model a Wnt bead by changing the BSW equations (33) in the marked triangles with the following equations:

$$\begin{aligned}\frac{\partial sox9}{\partial t} &= 0\\ \frac{\partial bmp}{\partial t} &= 0\\ \frac{\partial wnt}{\partial t} &= \alpha_{wnt}^2 + \gamma \nabla^2 wnt\end{aligned}$$

A simulation with the parameters in Table ST7 and $\alpha_{wnt}^2 = 1$ predicts a down-regulation of Sox9 and an up-regulation of Bmp in the region surrounding the bead, see the bottom row in Figure S6B. To test this prediction, we had to determine which Wnt ligand was the most likely candidate. We tested the effect of Wnt3a, Wnt5a and Wnt7a on Sox9-EGFP expression by adding recombinant proteins in micromass culture and implantation of protein-soaked beads in limb cultures, see Figure 37A-B. Although previous studies [85] have shown that Wnt7a inhibits chondrogenic differentiation in micromass cultures, we could not observed any effect on Sox9-EGFP. Similar results were obtained with Wnt5a. In constrast, Wnt3a promoted inhibition of Sox9-EGFP both in micromass and in bead implantation experiments, suggesting that Wnt3a could act as a the primary ligand in our model. Although this gene is expressed in the ectoderm, previous studies have proposed that ectodermal Wnts can indeed regulate gene expression in the mesenchyme, eg. Wnt3a restricts Sox9 and chondrogenesis to the core mesenchyme [21-23] and Wnt7a activates Lmx1b in the dorsal half of the mesenchyme (spanning from the sub-ectodermal tissue, to the core of the limb bud) [85]. However, we cannot rule-out that Wnts expressed in the mesenchyme, such as Wnt5a [79,86] and Wnt14 [87], might also contribute to digit patterning.

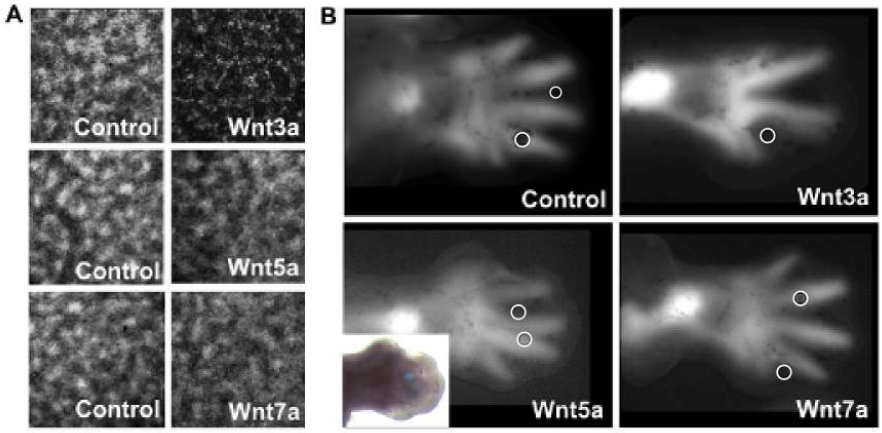

Figure 37: A-B) When Wnt3a is added to the micromass culture or Wnt3a-soaked beads are implanted in limb cultures, Sox9-EGFP is inhibited in comparison to similar experiments done with Wnt5a and Wnt7a recombinant proteins. This suggest that Sox9 is inhibited by Wnt/β-catenin canonical pathway. However, Wnt7a and Wnt5a genetic perturbations show that these ligand are also mediating Sox9 regulation, see Table ST10.

2.12 Robustness of the BSW model

The linear stability analysis presented in section 2.2 shows that when $f_{sox9} = 0$ and $D_{sox9} = 0$, as in the BSW network, the Turing instability condition (6) is relaxed to (8). This implies that the BSW network has particularly large Turing space and suggests that it should implement a robust patterning mechanism. To test this hypothesis, first we perturbed the concentration of $bmp, sox9$ and wnt with different amount of Gaussian noise, secondly we perturbed the reaction rates k_i and diffusion parameters γ, d with different relative strength.

2.12.1 Robustness to noise

The BSW model can be written as a system of stochastic partial differential equation (SPDEs) as follows:

$$\begin{aligned}
\frac{\partial sox9}{\partial t} &= f(sox9, bmp, wnt) + \eta(t, sox9) \\
\frac{\partial bmp}{\partial t} &= g(sox9, bmp, wnt) + D_{bmp}\nabla^2 bmp + \eta(t, bmp) \\
\frac{\partial wnt}{\partial t} &= h(sox9, bmp, wnt) + D_{wnt}\nabla^2 wnt + \eta(t, wnt)
\end{aligned}$$

where $f(sox9, bmp, wnt), g(sox9, bmp, wnt), h(sox9, bmp, wnt)$ the reaction terms presented in equation (33) and $\eta(t, sox9), \eta(t, bmp), \eta(t, wnt)$ are noise terms written as:

$$\begin{aligned}
\eta(t, sox9) &= \upsilon \quad sox9 \quad W_t^s \\
\eta(t, bmp) &= \upsilon \quad bmp \quad W_t^b \\
\eta(t, wnt) &= \upsilon \quad wnt \quad W_t^w
\end{aligned}$$

with W_t^s, W_t^b, W_t^w that are normally distributed random variables and υ that is a constant between 0 and 1 that defines the amount of multiplicative noise (intrinsic noise) in the system.

At every integration step, we solve this system of SPDEs in a manner similar to the Euler Maruyama method:

let define Δt_n as the time-step used by the Heun method at the iteration n, the noise terms $\eta(t, sox9), \eta(t, bmp), \eta(t, wnt)$ can be calculated by sampling the normally distributed random variables W_n^s, W_n^b, W_n^w with expected value 0 and variance Δt_n. The amount of noise can be modulated by varying the υ.

We simulate the BSW model (33) with the parameters in Table ST6 considering an increasing amount of multiplicative noise. Our analysis reveals that the model can form a digit pattern with at most 5% of multiplicative noise, see Figure 38.

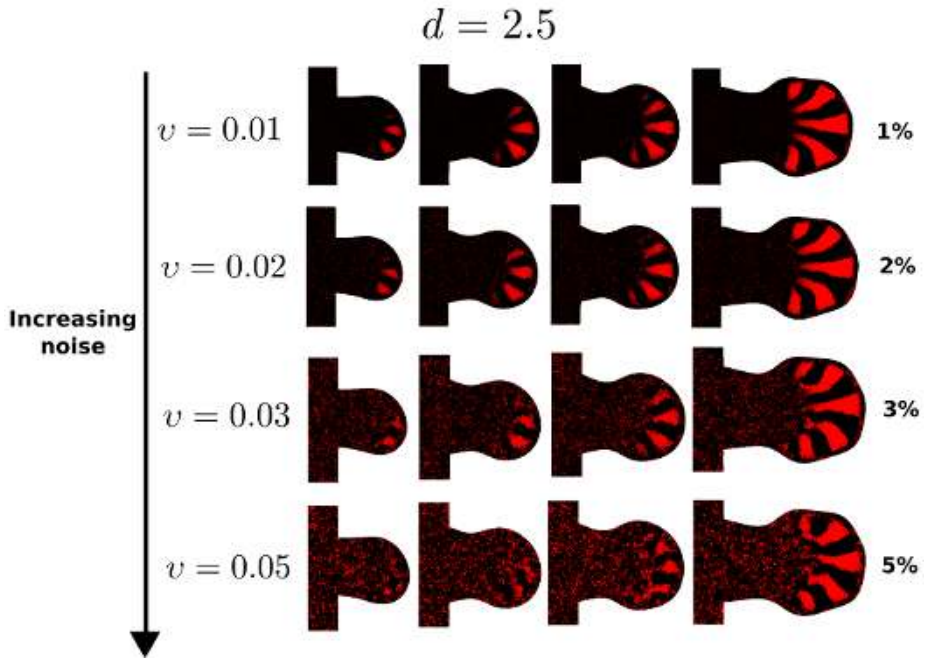

Figure 38: Simulation presented in Figure 3E (main text) with progressively increasing noise, Sox9 concentration in red. The model produces a pattern up to $\upsilon = 0.05$ that corresponds to 5% of multiplicative noise.

Interestingly, we find that the robustness to noise can be dramatically increased if we increased the parameter d that controls the ratio between the diffusion of Bmp and Wnt. If for example we set $d = 10$, the BSW model is able to form a digit pattern even when $\upsilon = 0.5$, which represents 50% of multiplicative noise, see Figure 39. This is in agreement with the analysis presented in Section 2.4, that shows that when d increases the parameter Turing space becomes larger making the reaction-diffusion mechanism more robust.

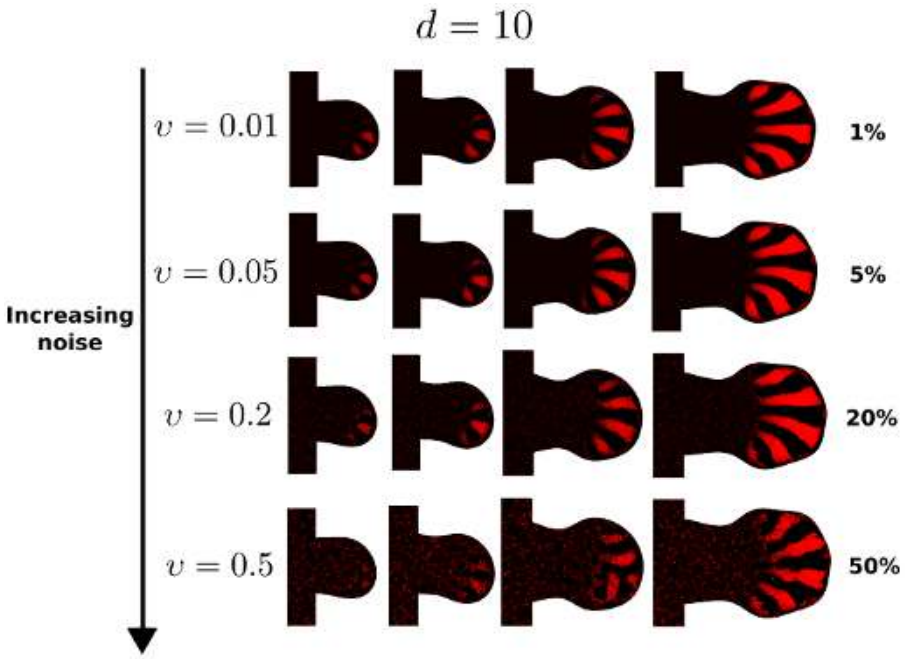

Figure 39: Simulations with progressively increasing noise of the BSW system (33) with the parameters in Table ST7 except for $d = 10$, Sox9 concentration in red. The model produces a pattern even with $v = 0.5$ that corresponds to 50% of multiplicative noise.

2.12.2 Robustness to parameter variation

To test how robustly the BSW model can reproduce the experimental Sox9 pattern when the parameters are changed, we perform simulation of the BSW model (33) starting from the parameter set in Table ST6 and systematically perturbing each parameter by $\pm 10\%$ and $\pm 20\%$. The final time point of each perturbed simulations is shown in Figure 40. The simulations show that when the parameters are perturbed by $\pm 10\%$ the BSW model forms patterns with five digits or weak polydactyly and oligodactyly patterns. When the parameter perturbation is increased to $\pm 20\%$, the variation of final Sox9 increases showing polydactyly patterns with up to seven digits and oligodactyly pattern with up to four, see Figure 40. Nevertheless, the BSW model is still able to form patterns which have the same qualitative radial orientation of the digits towards the distal tip.

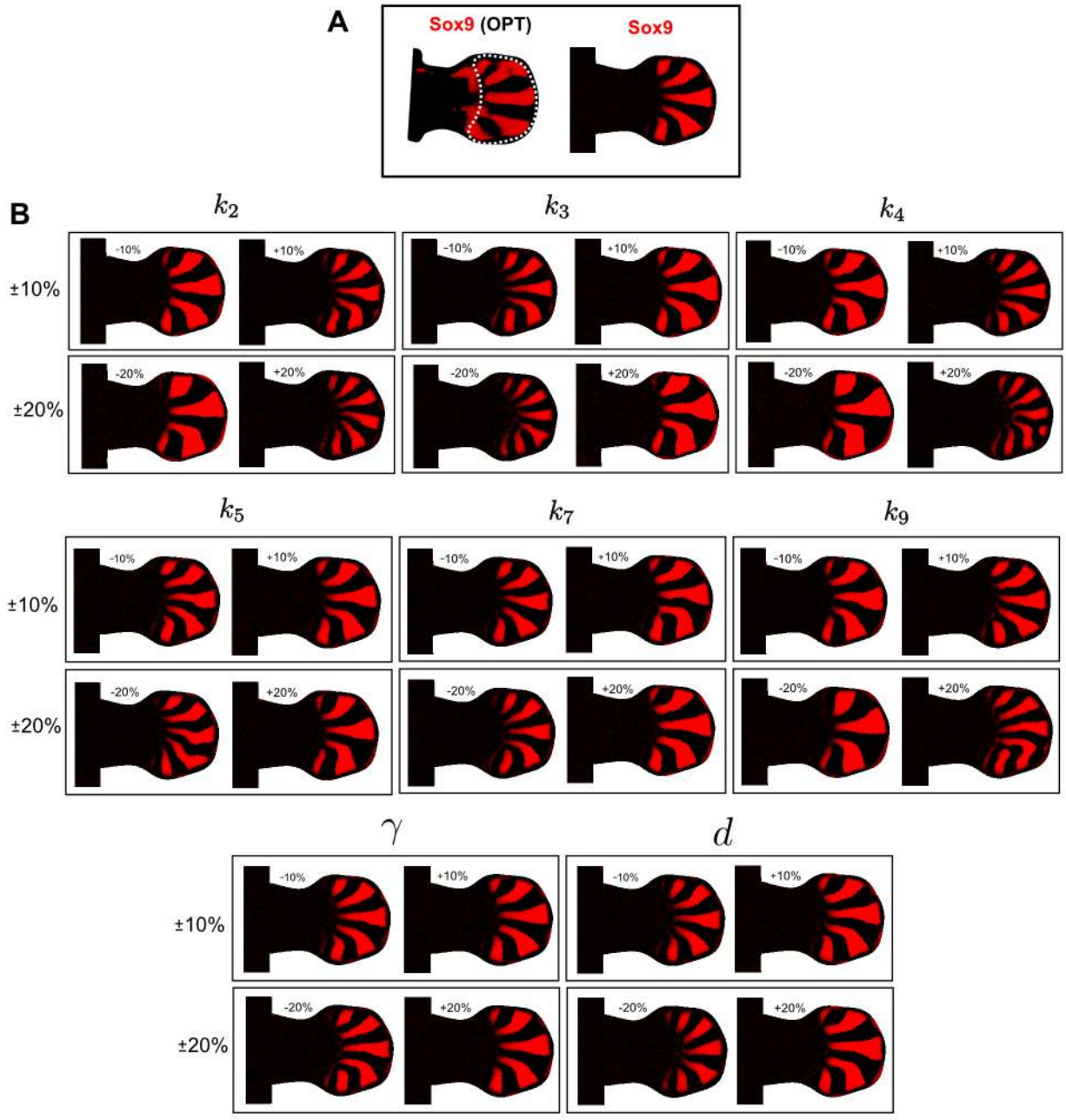

Figure 40: A) On the left, the experimental expression pattern of Sox9 at E12.5 obtained with OPT microscopy. On the right, the Sox9 pattern formed by the BSW model (33) at E12.5 with the parameter set in Table ST6. B) The Sox9 pattern at final time point (E12.5) of various simulations were the reaction rates k_i and the diffusion parameters γ and d have been varied of $\pm 10\%$ and $\pm 20\%$.

3 Other Supplementary Materials

3.1 Movie S1

The patterning dynamics of the micromass culture obtained with Sox9-EGFP autopod cells compared against the dynamics of the simulation of Turing mechanism (A simple linear model of a Substrate-depleted mechanism with two molecules).

3.2 Movie S2

Micromass culture initiated with Sox9-negative cells FACS-sorted from Sox9-EGFP autopods, the video shows 22h of culture. A periodic spatial pattern is formed by spatially-controlled Sox9 up-regulation.

3.3 Movie S3

Micromass culture initiated with Sox9-positive cells FACS-sorted from Sox9-EGFP autopods, the video shows 22h of culture. A periodic spatial pattern is formed by spatially-controlled Sox9 down-regulation.

3.4 Movie S4

Simulated concentration of Sox9 (high values in red) when the BSW model is simulated inside the limb growing model. The PD expansion that underlies limb elongation orients the stripes along the PD axis.

3.5 Movie S5

Simulated concentration of Sox9 (high values in red) when the activity of the BSW model is restricted to the autopod region by the experimental expression patterns of Hoxd13. A stereotypical pattern is formed thanks to the progressive expansion of Hoxd13 into the anterior and the proximal part of the limb which stimulate a reproducible spatial configuration of the Turing pattern. In later timepoints, distal stripe bifurcations are observed due to the geometry of the limb.

3.6 Movie S6

Simulated concentration of Sox9 (high values in red) when the activity of the BSW model is modulated by Fgf signaling to increase the wavelength and align the stripes. Stripe bifurcations are prevented and the pattern orients radially towards the AER.

3.7 Movie S7

Simulated concentration of Sox9 (high values in red) and Bmp (high values in green) when the activity of the BSW model is modulated by Fgf signaling and Hoxd13. A reproducible pattern that captures the main features of the experimental expression patterns of Sox9 is obtained.

3.8 Movie S8

Simulated concentration of Sox9 (high values in white), experimental expression pattern of Hoxd13 (high values in red) and Fgf signaling (high values in green). Spatio-temporal dynamics that robustly reflect the experimental expression patterns of Sox9 are obtained by modulating the the BSW Turing model with the positional information provided by Fgf signaling and Hoxd13.

3.9 Movie S9

Sox9 concentrations (high values in red) in a simulation where addition of LDN was simulated by inhibiting Bmp signaling. Similar to the experiment, Sox9 is down-regulated and the digit pattern is disrupted.

3.10 Movie S10

Sox9 concentrations (high values in red) in a simulation where addition of IWP2 (Wnt secretion inhibitor) was simulated by reducing the Wnt production term. Remarkably similar to the experimental situation, the Sox9 expression in the digits expands producing fusion of the digits.

3.11 Movie S11

22h of a Sox9-EGFP E11.5 limb culture with a Bmp2-soaked bead (dark circle) implanted in the autopod region.

3.12 Movie S12

Simulated concentration of Sox9 (high values in red) in a virtual Bmp-bead experiment. The virtual Bmp bead (white triangles) is implanted at E11.5.

3.13 Movie S13

22h of a Sox9-EGFP E11.5 limb culture with a Wnt3a-soaked bead (dark circle) implanted in the autopod region.

3.14 Movie S14

Simulated concentration of Sox9 (high values in red) in a virtual Wnt-bead experiment. The virtual Wnt bead (white triangles) is implanted at E11.5.

References and Notes

1. D. Summerbell, J. H. Lewis, L. Wolpert, Positional information in chick limb morphogenesis. *Nature* **244**, 492–496 (1973). Medline doi:10.1038/244492a0

2. R. D. Riddle, R. L. Johnson, E. Laufer, C. Tabin, Sonic hedgehog mediates the polarizing activity of the ZPA. *Cell* **75**, 1401–1416 (1993). Medline doi:10.1016/0092-8674(93)90626-2

3. R. Zeller, J. López-Ríos, A. Zuniga, Vertebrate limb bud development: Moving towards integrative analysis of organogenesis. *Nat. Rev. Genet.* **10**, 845–858 (2009). Medline doi:10.1038/nrg2681

4. E. Zwilling, Development of fragmented and of dissociated limb bud mesoderm. *Dev. Biol.* **9**, 20–37 (1964). Medline doi:10.1016/0012-1606(64)90012-0

5. Y. Litingtung, R. D. Dahn, Y. Li, J. F. Fallon, C. Chiang, Shh and Gli3 are dispensable for limb skeleton formation but regulate digit number and identity. *Nature* **418**, 979–983 (2002). Medline doi:10.1038/nature01033

6. A. M. Turing, The chemical basis of morphogenesis. *Bull. Math. Biol.* **52**, 153–197, 153–197 (1990). Medline doi:10.1007/BF02459572

7. S. A. Newman, H. L. Frisch, Dynamics of skeletal pattern formation in developing chick limb. *Science* **205**, 662–668 (1979). Medline doi:10.1126/science.462174

8. A. Gierer, H. Meinhardt, A theory of biological pattern formation. *Kybernetik* **12**, 30–39 (1972). Medline doi:10.1007/BF00289234

9. R. Sheth, L. Marcon, M. F. Bastida, M. Junco, L. Quintana, R. Dahn, M. Kmita, J. Sharpe, M. A. Ros, Hox genes regulate digit patterning by controlling the wavelength of a Turing-type mechanism. *Science* **338**, 1476–1480 (2012). Medline doi:10.1126/science.1226804

10. A. Badugu, C. Kraemer, P. Germann, D. Menshykau, D. Iber, Digit patterning during limb development as a result of the BMP-receptor interaction. *Sci. Rep.* **2**, 991 (2012). Medline doi:10.1038/srep00991

11. H. G. Hentschel, T. Glimm, J. A. Glazier, S. A. Newman, Dynamical mechanisms for skeletal pattern formation in the vertebrate limb. *Proc. Biol. Sci.* **271**, 1713–1722 (2004). Medline doi:10.1098/rspb.2004.2772

12. C. M. Leonard, H. M. Fuld, D. A. Frenz, S. A. Downie, J. Massagué, S. A. Newman, Role of transforming growth factor-beta in chondrogenic pattern formation in the embryonic limb: Stimulation of mesenchymal condensation and fibronectin gene expression by exogenenous TGF-beta and evidence for endogenous TGF-beta-like activity. *Dev. Biol.* **145**, 99–109 (1991). Medline doi:10.1016/0012-1606(91)90216-P

13. T. Miura, K. Shiota, TGFbeta2 acts as an “activator” molecule in reaction-diffusion model and is involved in cell sorting phenomenon in mouse limb micromass

culture. *Dev. Dyn.* **217**, 241–249 (2000). Medline doi:10.1002/(SICI)1097-0177(200003)217:3<241::AID-DVDY2>3.0.CO;2-K

14. R. Bhat, K. M. Lerea, H. Peng, H. Kaltner, H. J. Gabius, S. A. Newman, A regulatory network of two galectins mediates the earliest steps of avian limb skeletal morphogenesis. *BMC Dev. Biol.* **11**, 6 (2011). Medline doi:10.1186/1471-213X-11-6

15. V. Georgiadis, H. J. Stewart, H. J. Pollard, Y. Tavsanoglu, R. Prasad, J. Horwood, L. Deltour, K. Goldring, F. Poirier, D. J. Lawrence-Watt, Lack of galectin-1 results in defects in myoblast fusion and muscle regeneration. *Dev. Dyn.* **236**, 1014–1024 (2007). Medline doi:10.1002/dvdy.21123

16. E. Wright, M. R. Hargrave, J. Christiansen, L. Cooper, J. Kun, T. Evans, U. Gangadharan, A. Greenfield, P. Koopman, The Sry-related gene Sox9 is expressed during chondrogenesis in mouse embryos. *Nat. Genet.* **9**, 15–20 (1995). Medline doi:10.1038/ng0195-15

17. Y. Nakamura, K. Yamamoto, X. He, B. Otsuki, Y. Kim, H. Murao, T. Soeda, N. Tsumaki, J. M. Deng, Z. Zhang, R. R. Behringer, B. Crombrugghe, J. H. Postlethwait, M. L. Warman, T. Nakamura, H. Akiyama, Wwp2 is essential for palatogenesis mediated by the interaction between Sox9 and mediator subunit 25. *Nat. Commun.* **2**, 251 (2011). Medline doi:10.1038/ncomms1242

18. W. M. Kulyk, J. L. Franklin, L. M. Hoffman, Sox9 expression during chondrogenesis in micromass cultures of embryonic limb mesenchyme. *Exp. Cell Res.* **255**, 327–332 (2000). Medline doi:10.1006/excr.1999.4784

19. H. Akiyama, M. C. Chaboissier, J. F. Martin, A. Schedl, B. de Crombrugghe, The transcription factor Sox9 has essential roles in successive steps of the chondrocyte differentiation pathway and is required for expression of Sox5 and Sox6. *Genes Dev.* **16**, 2813–2828 (2002). Medline doi:10.1101/gad.1017802

20. K. Summerhurst, M. Stark, J. Sharpe, D. Davidson, P. Murphy, 3D representation of Wnt and Frizzled gene expression patterns in the mouse embryo at embryonic day 11.5 (Ts19). *GEP* **8**, 331–348 (2008). Medline doi:10.1016/j.gep.2008.01.007

21. D. ten Berge, S. A. Brugmann, J. A. Helms, R. Nusse, Wnt and FGF signals interact to coordinate growth with cell fate specification during limb development. *Development* **135**, 3247–3257 (2008). Medline doi:10.1242/dev.023176

22. T. P. Hill, D. Später, M. M. Taketo, W. Birchmeier, C. Hartmann, Canonical Wnt/beta-catenin signaling prevents osteoblasts from differentiating into chondrocytes. *Dev. Cell* **8**, 727–738 (2005). Medline doi:10.1016/j.devcel.2005.02.013

23. T. P. Hill, M. M. Taketo, W. Birchmeier, C. Hartmann, Multiple roles of mesenchymal beta-catenin during murine limb patterning. *Development* **133**, 1219–1229 (2006). Medline doi:10.1242/dev.02298

24. A. Bandyopadhyay, K. Tsuji, K. Cox, B. D. Harfe, V. Rosen, C. J. Tabin, Genetic analysis of the roles of BMP2, BMP4, and BMP7 in limb patterning and

skeletogenesis. *PLOS Genet.* **2**, e216 (2006). Medline doi:10.1371/journal.pgen.0020216

25. Q. Pan, Y. Yu, Q. Chen, C. Li, H. Wu, Y. Wan, J. Ma, F. Sun, Sox9, a key transcription factor of bone morphogenetic protein-2-induced chondrogenesis, is activated through BMP pathway and a CCAAT box in the proximal promoter. *J. Cell. Physiol.* **217**, 228–241 (2008). Medline doi:10.1002/jcp.21496

26. B. K. Zehentner, C. Dony, H. Burtscher, The transcription factor Sox9 is involved in BMP-2 signaling. *J. Bone Miner. Res.* **14**, 1734–1741 (1999). Medline doi:10.1359/jbmr.1999.14.10.1734

27. J. D. Bénazet, E. Pignatti, A. Nugent, E. Unal, F. Laurent, R. Zeller, Smad4 is required to induce digit ray primordia and to initiate the aggregation and differentiation of chondrogenic progenitors in mouse limb buds. *Development* **139**, 4250–4260 (2012). Medline doi:10.1242/dev.084822

28. E. J. Crampin, E. A. Gaffney, P. K. Maini, Reaction and diffusion on growing domains: Scenarios for robust pattern formation. *Bull. Math. Biol.* **61**, 1093–1120 (1999). Medline doi:10.1006/bulm.1999.0131

29. T. Miura, K. Shiota, G. Morriss-Kay, P. K. Maini, Mixed-mode pattern in Doublefoot mutant mouse limb—Turing reaction-diffusion model on a growing domain during limb development. *J. Theor. Biol.* **240**, 562–573 (2006). Medline doi:10.1016/j.jtbi.2005.10.016

30. L. Marcon, C. G. Arqués, M. S. Torres, J. Sharpe, A computational clonal analysis of the developing mouse limb bud. *PLOS Comput. Biol.* **7**, e1001071 (2011). Medline doi:10.1371/journal.pcbi.1001071

31. C. Tickle, B. Alberts, L. Wolpert, J. Lee, Local application of retinoic acid to the limb bond mimics the action of the polarizing region. *Nature* **296**, 564–566 (1982). Medline doi:10.1038/296564a0

32. M. Bienz, beta-Catenin: A pivot between cell adhesion and Wnt signalling. *Curr. Biol.* **15**, R64–R67 (2005). Medline doi:10.1016/j.cub.2004.12.058

33. G. R. Martin, The roles of FGFs in the early development of vertebrate limbs. *Genes Dev.* **12**, 1571–1586 (1998). Medline doi:10.1101/gad.12.11.1571

34. N. Mercader, E. Leonardo, M. E. Piedra, C. Martínez-A, M. A. Ros, M. Torres, Opposing RA and FGF signals control proximodistal vertebrate limb development through regulation of Meis genes. *Development* **127**, 3961–3970 (2000). Medline

35. T. Suzuki, S. M. Hasso, J. F. Fallon, Unique SMAD1/5/8 activity at the phalanx-forming region determines digit identity. *Proc. Natl. Acad. Sci. U.S.A.* **105**, 4185–4190 (2008). Medline doi:10.1073/pnas.0707899105

36. P. Mani, A. Jarrell, J. Myers, R. Atit, Visualizing canonical Wnt signaling during mouse craniofacial development. *Dev. Dyn.* **239**, 354–363 (2010). Medline

37. M. E. Ritchie, J. Silver, A. Oshlack, M. Holmes, D. Diyagama, A. Holloway, G. K. Smyth, A comparison of background correction methods for two-colour microarrays. *Bioinformatics* **23**, 2700–2707 (2007). Medline doi:10.1093/bioinformatics/btm412

38. B. M. Bolstad, R. A. Irizarry, M. Astrand, T. P. Speed, A comparison of normalization methods for high density oligonucleotide array data based on variance and bias. *Bioinformatics* **19**, 185–193 (2003). Medline doi:10.1093/bioinformatics/19.2.185

39. G. K. Smyth, Linear models and empirical bayes methods for assessing differential expression in microarray experiments. *Stat. Appl. Genet. Mol. Biol.* **3**, e3 (2004). Medline doi:10.2202/1544-6115.1027

40. Y. Benjamini, Y. Hochberg, Controlling the false discovery rate: A practical and powerful approach to multiple testing. *J. R. Stat. Soc. B* **57**, 289–300 (1995).

41. Bioconductor project (http://www.bioconductor.org/)

42. R statistical environment (http://cran.r-project.org/.

43. J. L. de la Pompa, A. Wakeham, K. M. Correia, E. Samper, S. Brown, R. J. Aguilera, T. Nakano, T. Honjo, T. W. Mak, J. Rossant, R. A. Conlon, Conservation of the Notch signalling pathway in mammalian neurogenesis. *Development* **124**, 1139–1148 (1997). Medline

44. J. Sharpe, U. Ahlgren, P. Perry, B. Hill, A. Ross, J. Hecksher-Sørensen, R. Baldock, D. Davidson, Optical projection tomography as a tool for 3D microscopy and gene expression studies. *Science* **296**, 541–545 (2002). Medline doi:10.1126/science.1068206

45. K. White, C. Gilligan, Spatial heterogeneity in three species, plant–parasite–hyperparasite, systems. *Philos. Trans. R. Soc. Lond. B Biol. Sci.* **353**, 543–557 (1998). doi:10.1098/rstb.1998.0226

46. J. D. Murray, *Mathematical Biology: I. An Introduction* (Springer, 2002).

47. I. Wolfram Research (Champaign, IL, 2010), version 8.0.

48. A. Kicheva, P. Pantazis, T. Bollenbach, Y. Kalaidzidis, T. Bittig, F. Jülicher, M. González-Gaitán, Kinetics of morphogen gradient formation. *Science* **315**, 521–525 (2007). Medline doi:10.1126/science.1135774

49. S. Zhou, W. C. Lo, J. L. Suhalim, M. A. Digman, E. Gratton, Q. Nie, A. D. Lander, Free extracellular diffusion creates the Dpp morphogen gradient of the Drosophila wing disc. *Curr. Biol.* **22**, 668–675 (2012). Medline doi:10.1016/j.cub.2012.02.065

50. H. Inomata, T. Shibata, T. Haraguchi, Y. Sasai, Scaling of dorsal-ventral patterning by embryo size-dependent degradation of Spemann's organizer signals. *Cell* **153**, 1296–1311 (2013). Medline doi:10.1016/j.cell.2013.05.004

51. P. Müller, K. W. Rogers, B. M. Jordan, J. S. Lee, D. Robson, S. Ramanathan, A. F. Schier, Differential diffusivity of Nodal and Lefty underlies a reaction-diffusion

patterning system. *Science* **336**, 721–724 (2012). Medline doi:10.1126/science.1221920

52. C. M. Cruciat, C. Niehrs, Secreted and transmembrane wnt inhibitors and activators. *Cold Spring Harb. Perspect. Biol.* **5**, a015081 (2013). Medline doi:10.1101/cshperspect.a015081

53. A. Yamamoto, T. Nagano, S. Takehara, M. Hibi, S. Aizawa, Shisa promotes head formation through the inhibition of receptor protein maturation for the caudalizing factors, Wnt and FGF. *Cell* **120**, 223–235 (2005). Medline doi:10.1016/j.cell.2004.11.051

54. F. Witte, J. Dokas, F. Neuendorf, S. Mundlos, S. Stricker, Comprehensive expression analysis of all Wnt genes and their major secreted antagonists during mouse limb development and cartilage differentiation. *GEP* **9**, 215–223 (2009). Medline doi:10.1016/j.gep.2008.12.009

55. R. Morello, T. K. Bertin, S. Schlaubitz, C. A. Shaw, S. Kakuru, E. Munivez, P. Hermanns, Y. Chen, B. Zabel, B. Lee, Brachy-syndactyly caused by loss of Sfrp2 function. *J. Cell. Physiol.* **217**, 127–137 (2008). Medline doi:10.1002/jcp.21483

56. W. Satoh, T. Gotoh, Y. Tsunematsu, S. Aizawa, A. Shimono, Sfrp1 and Sfrp2 regulate anteroposterior axis elongation and somite segmentation during mouse embryogenesis. *Development* **133**, 989–999 (2006). Medline doi:10.1242/dev.02274

57. W. Satoh, M. Matsuyama, H. Takemura, S. Aizawa, A. Shimono, Sfrp1, Sfrp2, and Sfrp5 regulate the Wnt/beta-catenin and the planar cell polarity pathways during early trunk formation in mouse. *Genesis* **46**, 92–103 (2008). Medline doi:10.1002/dvg.20369

58. N. Wada, Y. Kawakami, R. Ladher, P. H. Francis-West, T. Nohno, Involvement of Frzb-1 in mesenchymal condensation and cartilage differentiation in the chick limb bud. *Int. J. Dev. Biol.* **43**, 495–500 (1999). Medline

59. V. L. Church, P. Francis-West, Wnt signalling during limb development. *Int. J. Dev. Biol.* **46**, 927–936 (2002). Medline

60. M. C. Farach-Carson, J. T. Hecht, D. D. Carson, Heparan sulfate proteoglycans: Key players in cartilage biology. *Crit. Rev. Eukaryot. Gene Expr.* **15**, 29–48 (2005). Medline doi:10.1615/CritRevEukaryotGeneExpr.v15.i1.30

61. B. Gorsi, S. E. Stringer, Tinkering with heparan sulfate sulfation to steer development. *Trends Cell Biol.* **17**, 173–177 (2007). Medline doi:10.1016/j.tcb.2007.02.006

62. W. C. Lamanna, I. Kalus, M. Padva, R. J. Baldwin, C. L. Merry, T. Dierks, The heparanome—the enigma of encoding and decoding heparan sulfate sulfation. *J. Biotechnol.* **129**, 290–307 (2007). Medline doi:10.1016/j.jbiotec.2007.01.022

63. G. K. Dhoot, M. K. Gustafsson, X. Ai, W. Sun, D. M. Standiford, C. P. Emerson Jr., Regulation of Wnt signaling and embryo patterning by an extracellular sulfatase. *Science* **293**, 1663–1666 (2001). Medline doi:10.1126/science.293.5535.1663

64. A. P. Sahota, G. K. Dhoot, A novel SULF1 splice variant inhibits Wnt signalling but enhances angiogenesis by opposing SULF1 activity. *Exp. Cell Res.* **315**, 2752–2764 (2009). Medline doi:10.1016/j.yexcr.2009.06.029

65. W. Zhao, G. B. Sala-Newby, G. K. Dhoot, Sulf1 expression pattern and its role in cartilage and joint development. *Dev. Dyn.* **235**, 3327–3335 (2006). Medline doi:10.1002/dvdy.20987

66. X. Guo, X. F. Wang, Signaling cross-talk between TGF-beta/BMP and other pathways. *Cell Res.* **19**, 71–88 (2009). Medline doi:10.1038/cr.2008.302

67. A. Munteanu, R. V. Solé, Pattern formation in noisy self-replicating spots. *Int. J. Bifurcat. Chaos* **16**, 3679–3685 (2006). doi:10.1142/S0218127406017063

68. C. Geuzaine, J. F. Remacle, Gmsh: A 3-D finite element mesh generator with built-in pre-and post-processing facilities. *Int. J. Numer. Methods Eng.* **79**, 1309–1331 (2009). doi:10.1002/nme.2579

69. C. Fromental-Ramain, X. Warot, N. Messadecq, M. LeMeur, P. Dollé, P. Chambon, Hoxa-13 and Hoxd-13 play a crucial role in the patterning of the limb autopod. *Development* **122**, 2997–3011 (1996). Medline

70. Gimp: The GNU Image Manipulation Program (http://www.gimp.org/).

71. JavaMorph—picture merging by interpolated deformation (http://code.google.com/p/javamorph/).

72. B. Boehm, M. Rautschka, L. Quintana, J. Raspopovic, Z. Jan, J. Sharpe, A landmark-free morphometric staging system for the mouse limb bud. *Development* **138**, 1227–1234 (2011). Medline doi:10.1242/dev.057547

73. W. Schroeder, K. Martin, B. Lorensen, *An Object-Oriented Approach To 3D Graphics* (Prentice-Hall, Englewood Cliffs, NJ, 1997).

74. D. A. Ovchinnikov, J. Selever, Y. Wang, Y. T. Chen, Y. Mishina, J. F. Martin, R. R. Behringer, BMP receptor type IA in limb bud mesenchyme regulates distal outgrowth and patterning. *Dev. Biol.* **295**, 103–115 (2006). Medline doi:10.1016/j.ydbio.2006.03.013

75. J. Selever, W. Liu, M. F. Lu, R. R. Behringer, J. F. Martin, Bmp4 in limb bud mesoderm regulates digit pattern by controlling AER development. *Dev. Biol.* **276**, 268–279 (2004). Medline doi:10.1016/j.ydbio.2004.08.024

76. S. E. Yi, P. S. LaPolt, B. S. Yoon, J. Y. Chen, J. K. Lu, K. M. Lyons, The type I BMP receptor BmprIB is essential for female reproductive function. *Proc. Natl. Acad. Sci. U.S.A.* **98**, 7994–7999 (2001). Medline doi:10.1073/pnas.141002798

77. H. Akiyama, H. S. Stadler, J. F. Martin, T. M. Ishii, P. A. Beachy, T. Nakamura, B. de Crombrugghe, Misexpression of Sox9 in mouse limb bud mesenchyme induces polydactyly and rescues hypodactyly mice. *Matrix Biol.* **26**, 224–233 (2007). Medline doi:10.1016/j.matbio.2006.12.002

78. J. J. Barrott, G. M. Cash, A. P. Smith, J. R. Barrow, L. C. Murtaugh, Deletion of mouse Porcn blocks Wnt ligand secretion and reveals an ectodermal etiology of human focal dermal hypoplasia/Goltz syndrome. *Proc. Natl. Acad. Sci. U.S.A.* **108**, 12752–12757 (2011). Medline doi:10.1073/pnas.1006437108

79. T. P. Yamaguchi, A. Bradley, A. P. McMahon, S. Jones, A Wnt5a pathway underlies outgrowth of multiple structures in the vertebrate embryo. *Development* **126**, 1211–1223 (1999). Medline

80. J. R. Barrow, K. R. Thomas, O. Boussadia-Zahui, R. Moore, R. Kemler, M. R. Capecchi, A. P. McMahon, Ectodermal Wnt3/beta-catenin signaling is required for the establishment and maintenance of the apical ectodermal ridge. *Genes Dev.* **17**, 394–409 (2003). Medline doi:10.1101/gad.1044903

81. B. A. Parr, A. P. McMahon, Dorsalizing signal Wnt-7a required for normal polarity of D-V and A-P axes of mouse limb. *Nature* **374**, 350–353 (1995). Medline doi:10.1038/374350a0

82. X. Zhu, H. Zhu, L. Zhang, S. Huang, J. Cao, G. Ma, G. Feng, L. He, Y. Yang, X. Guo, Wls-mediated Wnts differentially regulate distal limb patterning and tissue morphogenesis. *Dev. Biol.* **365**, 328–338 (2012). Medline doi:10.1016/j.ydbio.2012.02.019

83. B. Chen, M. E. Dodge, W. Tang, J. Lu, Z. Ma, C. W. Fan, S. Wei, W. Hao, J. Kilgore, N. S. Williams, M. G. Roth, J. F. Amatruda, C. Chen, L. Lum, Small molecule-mediated disruption of Wnt-dependent signaling in tissue regeneration and cancer. *Nat. Chem. Biol.* **5**, 100–107 (2009). Medline doi:10.1038/nchembio.137

84. A. C. Tufan, R. S. Tuan, Wnt regulation of limb mesenchymal chondrogenesis is accompanied by altered N-cadherin-related functions. *FASEB J.* **15**, 1436–1438 (2001). Medline

85. R. D. Riddle, M. Ensini, C. Nelson, T. Tsuchida, T. M. Jessell, C. Tabin, Induction of the LIM homeobox gene Lmx1 by WNT7a establishes dorsoventral pattern in the vertebrate limb. *Cell* **83**, 631–640 (1995). Medline doi:10.1016/0092-8674(95)90103-5

86. L. Topol, X. Jiang, H. Choi, L. Garrett-Beal, P. J. Carolan, Y. Yang, Wnt-5a inhibits the canonical Wnt pathway by promoting GSK-3-independent beta-catenin degradation. *J. Cell Biol.* **162**, 899–908 (2003). Medline doi:10.1083/jcb.200303158

87. C. Hartmann, C. J. Tabin, Wnt-14 plays a pivotal role in inducing synovial joint formation in the developing appendicular skeleton. *Cell* **104**, 341–351 (2001). Medline doi:10.1016/S0092-8674(01)00222-7